

Near-Infrared Diode Laser Absorption Spectroscopy for Measuring Film Thickness, Temperature, and Concentration in Liquid Films

Von der Fakultät für Ingenieurwissenschaften,
Abteilung Maschinenbau und Verfahrenstechnik der

Universität Duisburg-Essen

zur Erlangung des akademischen Grades

eines

Doktors der Ingenieurwissenschaften

Dr.-Ing.

genehmigte Dissertation

von

Rongchao Pan

aus

Jiangsu, China

1. Gutachter: Prof. Dr. Christof Schulz
2. Gutachter: Prof. Dr.-Ing. Johannes Kiefer

Tag der mündlichen Prüfung: 01. August 2017

Summary

Near-infrared (NIR) laser-absorption diagnostics in combination with diode lasers as light sources and fiber-optic beam delivery have been used extensively for *in situ* measurements of concentration and temperature of gas-phase combustion products (e.g., H₂O, CO, CO₂, NO₂, NO) due to the intrinsic advantages of this fast, sensitive, quantitative, and non-intrusive optical sensing technique. These measurements help designers, operators, and researchers of combustion devices to study combustion chemistry and thus reduce pollution and increase efficiency. This work focuses on liquid-phase absorption spectroscopy for analysis of liquid water films. In previous work, a multi-wavelength NIR diode laser absorption sensor had been developed in our laboratory to monitor liquid water thin films with $\sim 1.4 \mu\text{m}$ radiation. This thesis presents new applications of this sensor concept for real-time monitoring of the thickness, solute concentration, and temperature of thin films of aqueous solutions of NaCl and urea. The sensor monitors the transmittance of four near-infrared diode lasers through the aqueous liquid film deposited on a quartz plate. The variation of the absorption spectrum of the solution with temperature and solute concentration was used to select wavelengths for determining film thickness, solute concentration, and liquid temperature from ratios of the transmission measurements, where at least one of the two desired parameter (temperature or concentration) is known. The spectral database was measured by Fourier transform infrared (FTIR) spectrometry in the $5500\text{--}8000 \text{ cm}^{-1}$ range for the respective solutions at various concentrations and temperatures. A prototype sensor was constructed, and the sensor concept was validated with measurements using a temperature-controlled calibration cell with known plate separations. Temporal variations of film thickness and solute concentration were captured during the constant-temperature evaporation of liquid films deposited on optically polished temperature-stabilized quartz flats.

The development of a four-wavelength NIR laser-based absorption diagnostic for simultaneous measurement of thickness, temperature and urea concentration coupled with Bayesian methodology is described. The Bayesian analysis is based on a spectral database generated with a FTIR spectrometer in the $5500\text{--}8000 \text{ cm}^{-1}$ range with variable temperature and urea concentration. The concept was first validated with measurements using the calibration cell. Probability densities in the measured parameters were quantified using a Markov-chain Monte-Carlo (MCMC) algorithm, which were used to derive credibility intervals. As a practical demonstration, the temporal variation of film thickness, urea concentration, and liquid temperature were recorded during evaporation of a liquid film deposited on a transparent heated quartz plate.

Finally, a dual-wavelength diode laser-based absorption sensor for stand-off point measurements of water film thickness on an opaque surface is presented. The sensor consists of

a diode laser source, a foil as backscattering target, and off-axis paraboloids for collecting the fraction of the laser radiation transmitted through the liquid layer via retro-reflection. The water film thickness at a given temperature was determined from measured transmittance ratios at the two laser wavelengths. The sensor concept was first validated with measurement using the temperature-controlled calibration cell providing liquid layers of variable and known thickness between 100 and 1000 μm . Subsequently, the sensor was demonstrated successfully during recording the time varying thickness of evaporating water films at fixed temperatures. The film thickness was recorded as a function of time at three temperatures down to 50 μm .

Zusammenfassung

Nahinfrarot (NIR) Laser-Absorptionsdiagnostik in Kombination mit Diodenlasern als Lichtquellen und faseroptischer Strahlübertragung sind in großem Umfang in der Gasphase als schnelle, empfindliche, quantitative und berührungslose optische Messtechnik für die In-situ-Messung von Konzentrationen (z.B. H₂O, CO, CO₂, NO₂ und NO) und der Temperatur eingesetzt worden. Diese Messungen können Entwicklern, Betreibern und Forschern von Verbrennungsvorrichtungen helfen, Verbrennungsprozesse zu verstehen und dadurch Abgase zu verringern und die Effizienz zu erhöhen. Die vorliegende Arbeit konzentriert sich auf die Absorptionsspektroskopie in der flüssigen Phase für die Analytik von wässrigen Filmen. In einer früheren Arbeit wurde ein auf Diodenlasern basierender Absorptionssensor mit einer Kombination von mehreren Wellenlängen (~1.4 µm) in unserem Labor entwickelt, um Schichtdicken von wässrigen Flüssigkeitsfilmen zu bestimmen. Im Rahmen der vorliegenden Arbeit werden neue Anwendungen des Sensorkonzepts vorgestellt, wobei lokale Eigenschaften wässriger Filme, nämlich Filmdicke, Temperatur und die Konzentration von gelösten Substanzen (Salze, Harnstoff) detektiert werden. Dieser Sensor bestimmt die optischen Transmissionen durch wässrige Filme auf einer transparenten Quarzglasplatte. Die Temperatur- und Konzentrationsabhängigkeit der Absorptionsspektren wässriger Lösungen wurde genutzt, um für eine Auswahl von Laserwellenlängen die Schichtdicke, Konzentration gelöster Stoffe und die Temperatur aus der Variation zu bestimmen, wobei mindestens einer von zwei erwünschten Parametern (Temperatur oder Konzentration) bekannt sein musste. Diese Spektrendatenbank wurde durch Fourier-Transform-Infrarot-Spektroskopie (FTIR-Spektroskopie) im Spektralbereich zwischen 5500 und 8000 cm⁻¹ für entsprechende Lösungen mit unterschiedlichen Konzentrationen und Temperaturen erstellt. Ein Prototyp-Sensor wurde durch Messungen mit einer Kalibrierküvette bei bekannter Temperatur und bekannter Schichtdicke validiert. Anschließend wurden die zeitlichen Variationen von Schichtdicke und Konzentration während der Verdunstung eines freien Wasserfilms bei konstanter Temperatur auf einer transparenten Quarzglasplatte gemessen.

Um mehr als zwei Parameter (Filmschichtdicke, Temperatur und Harnstoffkonzentration) simultan messen zu können, wird anschließend eine Weiterentwicklung der Diagnostik zusammen mit der Bayes'schen Methode beschrieben. Die Bayes'sche Analyse basiert auf einer Spektrendatenbank, die mit einem FTIR-Spektrometer im NIR-Bereich (5500–8000 cm⁻¹) mit unterschiedlichen Temperaturen und Harnstoffkonzentrationen erstellt wurde. Dieses Konzept wurde zuerst an bekannten Schichtdicken in einer Kalibrierküvette validiert. Die Wahrscheinlichkeitsdichten der Messgrößen wurden durch einen Markov-Chain-Monte-Carlo-Algorithmus (MCMC-Algorithmus) ermittelt, aus dem sich die glaubhaften Intervalle bestimmen lassen. Für eine praktische Demonstration wurden die zeitlichen Variationen von Filmdicke, Harnstoffkonzentration und Flüssigkeitstemperatur wäh-

rend eines Verdampfungsvorgangs auf einer transparenten und beheizten Oberfläche bestimmt.

Schließlich wird ein auf zwei Diodenlasern verschiedener Wellenlänge basierender Absorptionssensor für die Messung von Filmparametern von auf nicht-transparenten Oberflächen deponierten Filmen vorgestellt. Der Sensor besteht aus einer Diodenlaser-Quelle, einer Folie als Rückstreutarget und Off-Axis-Parabolspiegeln zum Sammeln der durch den Wasserfilm transmittierten und an der Folie retroreflektierten Laserstrahlung. Die Wasserfilmdicke bei einer gegebenen Temperatur wurde aus der Variation der gemessenen Transmissionen bei den beiden Laserwellenlängen bestimmt. Das Sensorkonzept wurde zuerst in einer Kalibrierküvette mit Temperaturregelung und bekannter Filmdicke von 100 bis 1000 μm validiert. Dann wurde der Sensor für die Aufnahme zeitlicher Änderungen der Schichtdicke eines verdampfenden Wasserfilms bei einer festgelegten Temperatur erfolgreich demonstriert. Die Schichtdicke wurde als Funktion der Zeit bei drei Temperaturen bis zu 50 μm aufgezeichnet.

Contents

1	Introduction	1
1.1	Motivation	1
1.2	Organization of the thesis	4
1.3	Literature review of liquid-film measurement techniques	5
2	Theoretical background	9
2.1	Laser absorption spectroscopy.....	9
2.1.1	Spectroscopy.....	9
2.1.2	Infrared spectroscopy.....	11
2.1.3	NIR absorption spectroscopy in liquids.....	16
2.1.4	Beer-Lambert law	17
2.2	Measurement of absorption spectra	19
2.2.1	Spectrometer with broadband illumination	19
2.2.2	FTIR spectroscopy.....	20
2.2.3	Interference challenges	22
3	Measurement of absorption spectra of aqueous solutions with FTIR.....	25
3.1	Absorption of pure water	26
3.2	Absorption of aqueous NaCl solutions.....	27
3.2.1	NIR spectra of aqueous NaCl solution at fixed temperature	29
3.2.2	Temperature dependence of NIR spectra of aqueous NaCl solution at fixed concentration.....	30
3.3	Absorption of aqueous urea solutions	31
3.3.1	NIR spectra of aqueous urea solution at fixed temperature.....	32
3.3.2	Temperature dependence of NIR spectra of aqueous urea solution at fixed concentration.....	34
3.4	Uncertainty analysis in measured absorption coefficient	35
4	Measurement of liquid films in transmission.....	37
4.1	Measurement strategy.....	37
4.2	Design of sensor to characterize aqueous solutions of NaCl.....	38
4.2.1	Measurement of solute concentration and film thickness at constant liquid temperature	39
4.2.2	Measurement of liquid film temperature and film thickness at constant solute concentration.....	41
4.3	Design of sensor to characterize aqueous solutions of urea	42
4.3.1	Measurement of urea concentration and film thickness at constant liquid temperature	42
4.3.2	Measurement of liquid temperature and film thickness at constant urea concentration.....	44

4.4	Experimental setup of multiplexed diode laser absorption sensor.....	45
4.5	Demonstration of liquid-film measurements.....	48
4.5.1	Measurement of liquid-film parameters of aqueous of NaCl solutions	48
4.5.2	Measurement in the liquid film of urea solution	51
4.6	Time-resolved measurements of film properties.....	54
4.7	Summary	58
5	Uncertainty quantification and design-of-experiment using Bayesian inference	61
5.1	Introduction	61
5.2	Sensor strategy and Bayes' model	62
5.2.1	Theoretical framework and algorithm	62
5.2.2	Bayes' model.....	64
5.3	Error modeling	66
5.4	Results and discussion.....	68
5.4.1	Validation experiments.....	68
5.4.2	Temporal variation of film evaporation	70
5.5	Summary	72
6	Measurement of liquid films in retro-reflection	73
6.1	Motivation and overview	73
6.2	Characterization of retro-reflecting foils.....	74
6.3	Measurement strategy and sensor design	77
6.4	Results and discussion.....	80
6.4.1	Demonstration of liquid-film measurements.....	80
6.4.2	Time-resolved measurements of an evaporating thin film at constant temperature	81
6.5	Summary	85
7	Conclusions and future work	87
7.1	Conclusions	87
7.2	Future work	88
8	Own publications originating from this thesis.....	91
8.1	Articles in peer-reviewed journals	91
8.2	Non peer-reviewed articles and conference presentations	91
9	References	93
10	List of abbreviations.....	103
11	Acknowledgments.....	109

1 Introduction

1.1 Motivation

The quantitative knowledge of liquid film properties in the sub-millimeter range is relevant in many practical applications. For instance, fuel injection systems and intake geometries of internal combustion (IC) engines can be designed to improve fuel efficiency and minimize soot emissions by studying wall wetting during fuel injection associated with incomplete combustion [1-7]. Liquid water films are of interest in many practical applications, e.g., in fire suppression [8], steam power generation [9], water desalination [10], and the selective catalytic reduction (SCR) process using aqueous urea solution for NO_x reduction in exhaust gases from IC engines [11-13].

In many applications, in addition to film thickness, the temperature and the solute concentration of the liquid are also of interest, since this parameter on one hand influences various heat and mass transfer processes [14]. On the other hand, temperature is needed for film thickness evaluation because absorption or emission based techniques depend on absorption cross-section and fluorescence quantum yield. Another example is the SCR process based on urea-water solution that is sprayed into the hot exhaust stream in the tail pipe to produce ammonia by urea thermolysis and hydrolysis of HNCO [15]. During spray pyrolysis, wall wetting and liquid film formation with rapid subsequent temperature reduction and solid urea coating of the wall are unwanted processes and need to be controlled. Diagnostic methods for the measurement of film thickness, liquid temperature and solute concentration might be one approach for setting up a monitoring and control loop.

To optimize the performance of such systems, it is of great interest in obtaining a quantitative understanding of physical processes involved in liquid film formation and its development over time. One family of methods for liquid film thickness measurements is based on electrical techniques [16-20]. They are mostly based on the relationship between conductance and thickness of the liquid film between a pair of electrodes. Another family of techniques for liquid film thickness measurements are optical methods including, e.g., optical interference [9, 21-26], laser absorption spectroscopy [27-32], shadowgraphy [33], and laser-induced fluorescence (LIF) [5, 34-37]. Absorption based methods for liquid film thickness measurements so far have used light sources in the visible [27] or near infrared spectral region [30-32]. Compared to electrical methods, optical diagnostics are nonintrusive.

sive, require optical but not physical access, and are little affected by physical effects and chemical reactions that may occur within a sampling manifold.

Diode-laser absorption spectroscopy (DLAS) has long been the basis of the measurement of concentration and temperature of vapor-phase water as a combustion product [38-40], and the use of multi-wavelength diode laser absorption sensor strategy has been used for nearly 20 years for gas-phase measurements [41]. Many of the distributed feedback (DFB) lasers on the market are manufactured as fiber-coupled modules for the convenience of the telecom industry. This makes fiber-coupled sensor strategies especially attractive and simple. Most importantly, by combining laser beams in a common single-mode fiber, one makes sure that a common free-space path is shared by each laser through the sample. In this thesis this concept will be applied to monitor liquid thin aqueous films. Exploiting the strong native light absorption in the near infrared (NIR) caused by liquid water, enables tracer-free thickness measurements of aqueous films. Yang et al. [32] demonstrated diode-laser-based absorption sensing of liquid film thickness of pure water using two NIR diode lasers at wavelengths of 1392 and 1469 nm, which are non-resonant with any water vapor transition. This work is extended to solutions and studies of the liquid temperature, solute concentration, and film thickness measurement of aqueous salt and urea solutions in transmission.

There are three different types of multiplexing schemes are commonly used: Time-Division Multiplexing (TDM), Frequency-Division Multiplexing (FDM), and Wavelength-Division Multiplexing (WDM). FDM is typically used in modulation spectroscopy where the different wavelengths are modulated at different frequencies which is not used in the present thesis [42]. To monitor each individual laser wavelength transmitted through the liquid, two other multiplexing techniques (TDM and WDM) in the diode-laser based absorption sensors will be used. In both strategies, multiple laser beams with different emission wavelengths are combined and transmitted along the same optical path. The principles, strengths and weaknesses of the two methods will be introduced as below.

The schematic of a *wavelength-division multiplexing* (WDM) scheme is shown in Fig. 1 (left). The outputs from multiple DFB diode lasers are multiplexed together (usually by a single-mode fiber combiner) collimated and sent through the liquid sample. In order to monitor each individual laser wavelength, the transmitted laser beam is sent to a diffraction grating where it is dispersed into the constituent wavelengths and directed to multiple photodetectors. A diffraction grating consist of a series of closely spaced grooves that have been engraved or etched into a substrate (e.g., glass, metal). As light reflects off a grating, the grooves cause the light to diffract, dispersing the light into its component wavelengths.

Therefore, this technique cannot be used for a large number of wavelengths due to the overlap between different order reflections or the wavelength separation is geometrically insufficient. The WDM scheme has been used for the multi-wavelength absorption sensor to investigate the liquid film of pure water [29, 32]. In this thesis we extend this to aqueous solutions (see Chapter 4).

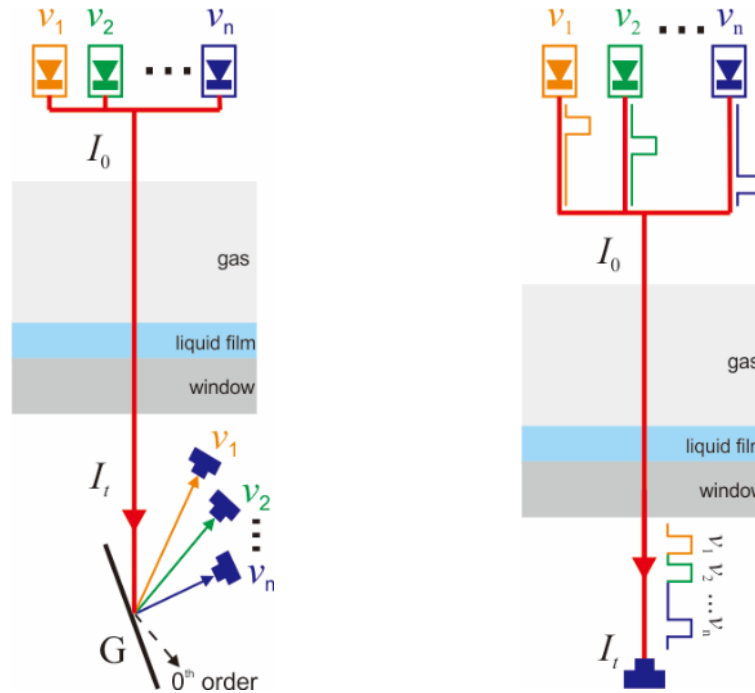


Fig. 1: Left: Schematic of wavelength-division multiplexing where the transmitted light is dispersed onto separate detectors for each laser wavelength. (I_0 , I_t : incident and transmitted laser intensity; G : diffraction grating). Right: Illustration of time-division multiplexing.

In a *time-division multiplexing* (TDM) scheme, alternately operated fixed-frequency lasers are multiplexed and transmitted through the sample. The transmitted laser beam is detected and attributed to the respective laser wavelength for each time interval. The advantage of the TDM scheme is that it allows for a simple optical setup, since only one detector is needed to measure the transmitted laser intensities from two or more lasers (Fig. 1, right). One shortcoming is that the transmitted laser intensities are not measured simultaneously, which will add extra measurement uncertainties for applications in rapidly fluctuating objects. As will be discussed in Chapter 6, the TDM technique was used for water film thickness measurements in retro-reflection. The primary advantages of TDM compared to WDM are the simplification of the optical setup that avoids the additional large signal loss when the emerging beams are diffracted off the grating for angular wavelength separation

and the robustness against mechanical vibrations during the experiment; TDM therefore improves the signal-to-noise ratio (SNR) in the measurements.

1.2 Organization of the thesis

The thesis is divided into four main parts:

1. Measurement of absorption spectra of aqueous solutions with FTIR
2. Development of a multi-parameter diagnostic in liquid film in transmission
3. Uncertainty quantification in absorption-based measurements via Bayesian inference
4. Development of a diagnostics for film thickness of pure water in retro-reflection

The order of the above topics is important; before developing laser-absorption diagnostics for multi-parameter measurements, the variation of absorption with temperature and solute concentration needs to be known. As will be shown in chapter 3, this database is measured here using a heated cuvette and a Fourier transform infrared (FTIR) spectrometer in the range between 5500 and 8000 cm^{-1} where the liquid water exhibits broadband absorption [43]. The spectral database is used to select laser wavelengths for a sensor based on absorption measurements at four distinct fixed wavelengths.

In chapter 4, the performance of this wavelength-multiplexed NIR diode laser sensor will be presented in validation experiments of liquid layers of variable thickness, solute concentration and temperature formed in a calibration cell consisting of two parallel quartz plates, where one of the parameters (temperature or solute concentration) needs to be known. Finally, a demonstration is presented for monitoring in real-time a constant-temperature evaporation of a liquid film deposited on a heated quartz plate.

In general, liquid temperature and solute concentration can change independently over time. For a simultaneous NIR absorption-based multi-parameter measurement of thickness, temperature, and solute concentration, the Bayesian methodology is used to infer probability densities for the obtained data (chapter 5). The Bayesian analysis is based on a temperature- and concentration-dependent spectral database. To demonstrate this concept validation measurements using a calibration cell will be presented. Probability densities in the measured parameters were quantified using a Markov chain Monte Carlo (MCMC) algorithm, which are used to derive credibility intervals. As a practical demonstration, the temporal variation of film thickness, urea concentration, and liquid temperature are recorded during evaporation of a liquid film deposited on a transparent and heated quartz plate.

In chapter 6, a dual-wavelength diode-laser-based absorption sensor for stand-off point measurements of water film thickness on an opaque surface will be presented. This development is motivated by practical applications where the liquid film is deposited onto opaque surfaces where optical access is only possible from one side and double-ended measurements are not feasible. The sensor consists of a diode laser source, a foil as back-scattering target, and off-axis paraboloids for collecting the fraction of the laser radiation transmitted through the liquid layer via retro-reflection. Two laser wavelengths in the near infrared are used where the temperature-dependence of the liquid water absorption cross-section is known. The lasers are fiber-coupled and the detection of the retro-reflected light is accomplished through a multimode fiber and a single photodiode using time-division multiplexing. The water film thickness at a given temperature is determined from measured transmittance ratios at the two laser wavelengths.

1.3 Literature review of liquid-film measurement techniques

The industrial importance of liquid thin films has led to significant research to develop characterization diagnostics. Many optical techniques have been successfully applied to measure or image liquid film thickness, a literature overview is given here.

One family of techniques for liquid film thickness measurements is based on interferometry. In this technique the light is reflected each time it passes from one material to another. The amount of light reflected depends on the wavelength of the light, the angle of incidence to the interface between the two materials and the refractive indices of both materials [44]. Unterberg reported an early application of an optical interference method for measuring the thickness of liquid film flow [45]. The method consisted of photographing and measuring the fringes appearing when a wide beam of monochromatic light illuminates a film. Interference occurs at the superposition of light beams reflected from mirror wall and film surface. Borgetto et al. developed a technique based on low-coherence interferometry (LCI) to measure liquid film thickness of linear alkanes [23]. A superluminescent light-emitting diode (SLED) was used as a light source to illuminate the film and generate interference patterns. The film thickness was obtained by subtracting the values of the positions of the detected interference maxima. Gao et al. introduced a wavelength-scanning interferometer for measuring the surface and thickness of a transparent film [25]. Combining a white light interferometer with a near-infrared (NIR) superluminescent light-emitting diode interferometer, it was possible to measure the liquid film thickness. Debnath et al. applied spectrally-resolved phase-shifting interferometry to determine thin transparent

films illuminated by a white light source [24]. In this case, the thickness of a thin transparent film on a reflecting substrate was measured through the analysis of the phase shift in spectrally resolved interferogram. Özdemir and Whitelaw derived an analytical correlation between the interferometric fringe pattern and the thickness of an unsteady liquid film [21]. This measurement technique has an accuracy that is independent of the film thickness and depends on the optical transformation function and the temporal resolution of the frequency measurements.

Another frequently applied technique to investigate liquid deposits on solid surface is based on laser-induced fluorescence (LIF) [46]. In this case, a fluorescent component in the liquid is excited by laser light and the subsequent fluorescence intensity is analyzed as a measure of the film thickness. The fluorescence can either arise from one of the components of the liquid itself or from a fluorescent tracer added, such as an aromatic component or a dye. This technique was applied in internal combustion engines for the determination of the amount of liquid deposited on surfaces and its layer thickness. Felton, using pulsed ultraviolet (UV) illumination of commercial gasoline at 355 nm from a frequency-tripled Nd:YAG laser and detection of LIF via an intensified charge-coupled device (CCD) camera, acquired two-dimensional maps of liquid fuel film thickness in the intake port of an internal combustion (IC) engine [2]. Signal intensities were converted to absolute thickness values by calibrating the setup with measurements in samples of known film thickness. Kull et al. reported a two-dimensional visualization technique based on LIF for investigation of liquid fuel film on transparent walls and its application in a spark ignition (SI) engine [34]. For fluorescence excitation, the beam from a XeCl-excimer laser at 308 nm was coupled into the quartz ring of the optical engine by a prism and guided to the liquid film by total internal reflection. Alonso et al. exploited total internal reflection (TIR) at the flat liquid/air interface of a UV laser beam (266 nm), which was coupled through a transparent quartz plate into a liquid film doped with 3-pentanone as a fluorescent tracer. This technique avoids the interference of signal contributions from airborne droplets present above the film, which is due to the fact that the laser continues its path upwards and the light thereby excites the airborne liquid fuel, increasing the fluorescence signal detected by the camera [35]. More recently, Wigger et al. developed a method for quantitative imaging of the oil film thickness that overcomes the main challenge, the accurate calibration of the detected fluorescence signal for film thickness in the low micrometer range [5]. Greszik et al. applied LIF with the organic tracer ethyl acetoacetate for imaging measurements of the thickness of liquid water-based films on a transparent quartz plate [5]. A UV laser beam at 266 nm was used to transverse and optically excite a tracer species dissolved in the water film deposited on a transparent window. Absolute LIF signal intensities were calibrated

with liquid layers of known thickness formed between two parallel quartz plates with adjustable distance.

An additional laser-based technique to measure liquid film thickness is based on light absorption. Mouza et al. used the absorption of visible light from a diode laser at 635 nm and detection of the transmitted beam by a photodiode through a flowing liquid film [27]. Using the law of Beer and Lambert, it is possible to determine the film thickness by measuring the absorption ratio in a calibrated system [47]. Wittig et al. used NIR laser radiation at 1523 nm to measure the film thickness of pure water in a rectangular duct [31]. Discrimination against light attenuation caused by other effects (e.g., windows) was accomplished by simultaneously recording the transmission of a second laser beam at 633 nm with negligible absorption in the water spectrum. Porter et al. quantified the strong absorption bands around 3.4 μm of liquid hydrocarbon fuels [48] and used a mid-infrared laser-absorption sensor in this wavelength range to determine the thickness of liquid films of n-dodecane on transparent windows in the presence of n-decane vapor [28]. More recently, Yang et al. demonstrated four-color sensing of liquid-film thickness, as well as liquid- and gas-phase temperature of a heated, evaporating water layer placed on a transparent wall in the thickness range between 300 and 1400 μm [29]. These tunable laser sources provide two key advantages: first, the laser can be tuned to wavelengths for which the absorption by the water vapor has the desired temperature dependence, and, second, multiple wavelengths are possible, allowing for a multi-parameter measurement in the liquid. In the present work, this diode-laser-based absorption method is extended to the measurement of film thickness, liquid temperature, and solute concentration in aqueous solutions.

2 Theoretical background

In this chapter, the basic theory of laser absorption spectroscopy and important related parameters are briefly introduced in the first section. Methods for the measurement of absorption spectra are presented in the second section.

2.1 Laser absorption spectroscopy

2.1.1 Spectroscopy

Light can be considered to have both wave properties and particle properties. Some properties of electromagnetic radiation, such as its refraction when it passes from air to water, are explained best by describing light as a wave. In this case, electromagnetic radiation consists of oscillating electric and magnetic fields that propagate through space along a linear path and with a constant velocity. An example of plane-polarized electromagnetic radiation, consisting of a single oscillating electric field and a single oscillating magnetic field is shown in Fig. 2.

The amplitude of the oscillating electric or magnetic field at any point along the propagating wave is

$$A_t = A_m \sin(2\pi\nu t + \Phi), \quad (1)$$

where A_t is the amplitude of the electric or magnetic field at time t , A_m is the maximum amplitude in the electric or magnetic field, ν is the wave's frequency, and Φ is a phase angle [49]. The wavelength λ is defined as the distance between successive maxima. The relationship in the vacuum between wavelength λ (in nm), frequency ν (in Hz) and wave-number $\tilde{\nu}$ (in cm^{-1}) is

$$c = \lambda \nu, \quad (2)$$

$$\tilde{\nu} = 1/\lambda, \quad (3)$$

where c is the speed of light (in m/s), which depends on the refractive index of the medium within which the light is traveling. As a result, the relationship involving the frequency and wavelength (cf., Eq. (3)) varies as the refractive index of the medium changes.

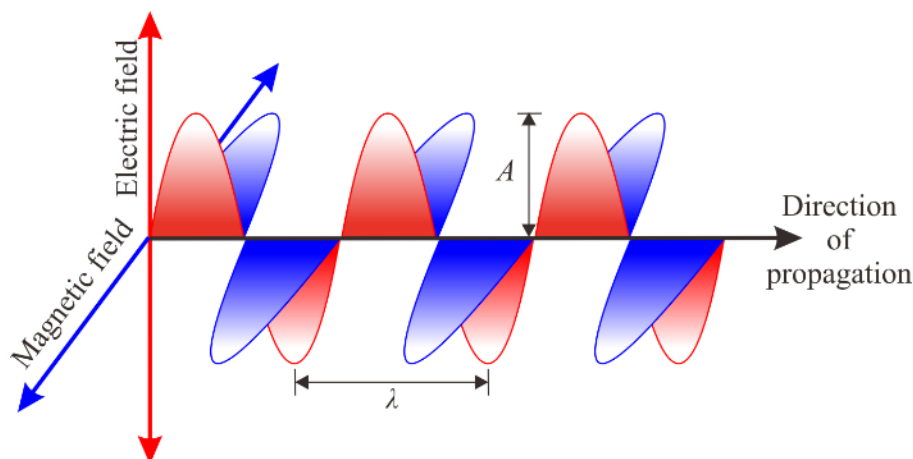


Fig. 2: Planar-polarized electromagnetic radiation showing the oscillating electric field in red and the oscillating magnetic field in blue. The radiation's amplitude A and its wavelength λ are shown [50].

As the frequency and wavelength of electromagnetic radiation vary over many orders of magnitude, the electromagnetic radiation is divided into different regions – the electromagnetic spectrum – based on the type of atomic or molecular transition that gives rise to the absorption or emission of photons [51]. The wavelength range of the electromagnetic spectrum comprises a wide scale ranging from radio waves to γ -rays (see Fig. 3). Note that the boundaries between the regions of the electromagnetic spectrum are, however, not rigid, and overlap between spectral regions is possible [50].

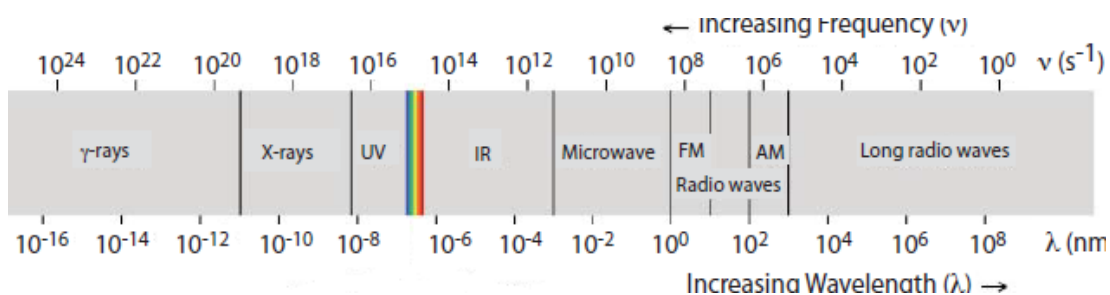


Fig. 3: The electromagnetic spectrum showing the boundaries between different regions and the type of atomic or molecular transition responsible for the change in energy [51].

Other properties, such as absorption and emission, are better described by treating light as a particle. In this case, the physical light-matter interaction phenomena that occur at the atomic and molecular levels will be discussed. A spectroscopic measurement is possible only if the photon's interaction with the sample leads to a change in one or more of the characteristic properties (energy, velocity, amplitude, frequency, phase angle, polarization, and direction of propagation). As there is only a transfer of energy between the photon and

the sample, several representative spectroscopic techniques can be divided according the type of energy transfer (see Table 1). This thesis will focus on the IR absorption spectroscopy.

Table 1: Examples of spectroscopic technique involving an exchange of energy between a photon and the sample [52]

Type of energy transfer	Region of electromagnetic spectrum	Spectroscopic technique	
Absorption	γ -ray	Mößbauer spectroscopy	
	X-ray	X-ray absorption spectroscopy	
	UV/Vis		UV/Vis spectroscopy
			Atomic absorption spectroscopy
	IR	Infrared spectroscopy	
	Microwave	Microwave spectroscopy	
	Radio wave		Electron spin resonance spectroscopy
		Nuclear magnetic resonance spectroscopy	
Thermal emission	UV/Vis	Atomic emission spectroscopy	
Photoluminescence	X-ray	X-ray fluorescence	
	UV/Vis	Fluorescence spectroscopy	
			Phosphorescence spectroscopy
			Atomic fluorescence spectroscopy
Chemiluminescence	UV/Vis	Chemiluminescence spectroscopy	

2.1.2 Infrared spectroscopy

Infrared spectroscopy is a physical method for qualitative as well as quantitative analysis. The spectral region extends from the upper part of the microwave range to the beginning of the visible region (cf., Fig. 3). It can be roughly subdivided into the near-IR, the mid-IR, and far-IR regions. The limits of the individual spectrum regions are not precisely defined, and therefore a certain wavelength range can also belong to several spectral regions.

As a photon is absorbed by an atom or molecule, it undergoes a transition from a low-energy state to an excited state (Fig. 4). The type of transition depends on the photon's

energy. From the law of conservation of energy, when a photon of energy $h\nu$ strikes the atom or molecule, absorption may occur if the difference in energy, ΔE , between the ground state and the excited state is equal to the photon's energy. An atom or molecule in an excited state may emit a quantum $h\nu$ and return to the ground state [53, 54].

The total excitation energy E of a molecule can be expressed as the sum of the partial excitations of the rotational, the vibrational, and the electronic degrees of freedom [50]. IR radiation does not have enough energy to induce electronic transitions. The absorption of IR radiation is restricted to compounds with small energy differences in the possible vibrational and rotational states. For a molecule to absorb IR radiation, the vibration or rotations within a molecule must cause a net change in the dipole moment of the molecule as a result of its oscillation and rotation. To understand the fundamental processes of IR spectroscopy, the Schrödinger equation, rotational transition, and vibrational transition will be introduced in detail below.

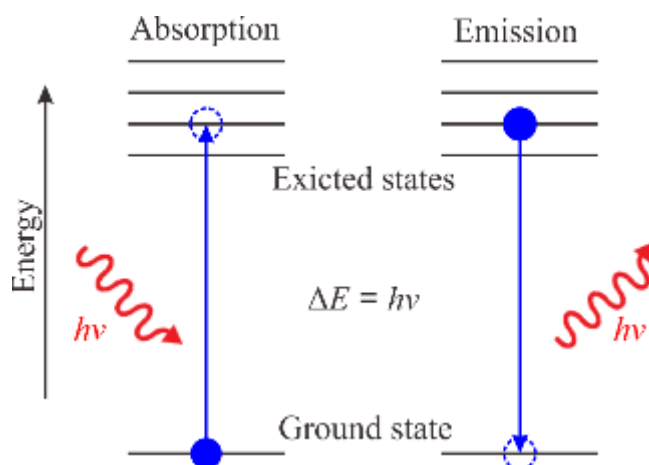


Fig. 4: Simplified energy diagram showing the absorption and emission of a photon by an atom or a molecule [50].

The Schrödinger equation

In quantum mechanical system, the energy levels for any molecule may be determined by solving the time-independent Schrödinger equation [44, 50]:

$$\mathbf{H}\Psi = E\Psi, \tag{4}$$

where \mathbf{H} is the Hamiltonian operator, Ψ is the wave function of the quantum system, and E is the total system energy. The Hamiltonian operator (total energy operator) is a sum of kinetic energy \mathbf{T} operator and the potential energy operator \mathbf{V} [55]:

$$\mathbf{H} = -\frac{\hbar}{2} \left(\frac{1}{m_e} \sum_i^n \Delta_i + \sum_j^k \frac{1}{M_j} \Delta_j + \mathbf{V} \right), \quad (5)$$

where $\hbar = h/2\pi$ is the Planck constant. The Schrödinger equation can be solved mathematically by making the Born-Oppenheimer approximation under the assumption that the electronic motion and the nuclear motion in molecules can be separated. In essence, the electronic wave function depends upon the nuclear positions but not upon their velocities, i.e., the nuclear motion is so much slower than electron motion that they can be considered to be fixed. The nuclear motion (e.g., rotation, vibration) sees a smeared out potential from the speedy electrons. The Hamiltonian may then be separated into an electronic (\mathbf{H}_{el}), a vibrational (\mathbf{H}_{vib}) and a rotational (\mathbf{H}_{rot}) part and be written as:

$$\mathbf{H} = \mathbf{H}_{\text{el}} + \mathbf{H}_{\text{vib}} + \mathbf{H}_{\text{rot}}, \quad (6)$$

yielding solutions of the Schrödinger equation with the total energy:

$$E = E_{\text{el}} + E_{\text{vib}} + E_{\text{rot}}, \quad (7)$$

where E_{el} is the electronic energy, E_{vib} is the vibrational energy, and E_{rot} is the rotational energy, each depending on one or more quantum numbers. Then the interaction between vibration and rotation can be taken into account by further factors.

Rotational spectra

If one assumes the diatomic molecule is a rigid rotor, in which the atoms are assumed as point masses with an equilibrium separation distance that is constant, the rotational energy can be obtained as

$$E_{\text{rot}} = \frac{h^2}{8\pi^2 I} J(J+1) \quad (8)$$

where $J = 0, 1, 2, 3, \dots$ is the rotational quantum number and h is Planck's constant. By convention, rotational energy is usually denoted by $F(J)$, in units of cm^{-1} . Referring to Eq. (8), the conversion is,

$$F(J) = \frac{E_{\text{rot}}}{hc} = \frac{h}{8\pi^2 Ic} J(J+1). \quad (9)$$

The rotational constant, B (in cm^{-1}), is

$$B = \frac{h}{8\pi^2 I_c}. \quad (10)$$

Thus, the rotational energy is given by

$$F(J) = BJ(J+1). \quad (11)$$

For pure rotational lines (absorption or emission), the change in rotational quantum number is $\Delta J = \pm 1$, and the rotational frequencies for these transitions are given by

$$\nu_{J' \leftarrow J''} = 2B(J''+1). \quad (12)$$

where J' and J'' are the quantum numbers for the upper and lower state, respectively.

Vibrational spectra

If one assumes that the diatomic molecule is a simple harmonic oscillator (SHO), the vibrational energy is given by

$$E_{\text{vib}} = \hbar\omega \left(\nu + \frac{1}{2} \right) \quad (13)$$

where $\nu = 0, 1, 2, 3, \dots$ is the vibrational quantum number, and ω is the classical oscillator frequency. Again, vibrational energy is usually denoted by $G(\nu)$, in units of cm^{-1} . Referring to Eq. (13), the conversion is

$$G(\nu) = \frac{E_{\text{vib}}}{hc} = \omega_e \left(\nu + \frac{1}{2} \right). \quad (14)$$

The quantum mechanics solution for absorption and emission assumed by the SHO model leads to a simple selection rule that says that the change in vibrational quantum number is $\Delta\nu = \pm 1$. The description of the vibrational motion for a diatomic system is rather simple, however polyatomic molecules present a large number of possible vibrations. Any vibrational motion can be decomposed into a set of so-called normal vibrations with suitable amplitude and phase. For a polyatomic molecule containing many (N) atoms there are $3N$ degrees of freedom from which $3N-6$ for nonlinear molecules, respectively $3N-5$ for linear systems are left to describe the vibrational motions of a molecular systems. Accordingly, there are $3N-6$ ($3N-5$) normal coordinates to describe the vibrational motion. The other 6 (5) coordinates describe the rotational and translational motions of the molecule. Carbon dioxide is cited as a typical example for a symmetric linear triatomic molecule (Fig. 5).

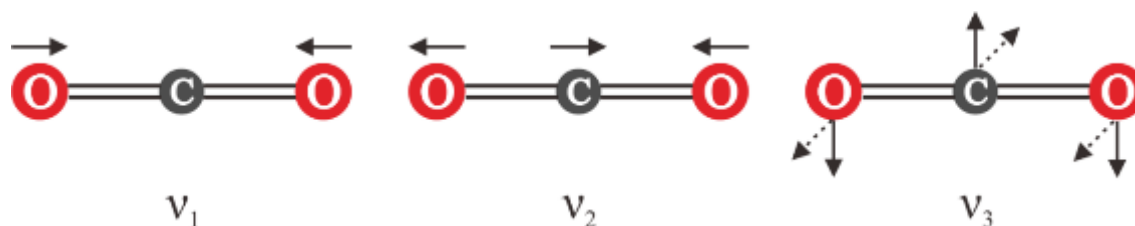


Fig. 5: The vibrational modes of carbon dioxide [56].

According to the following Table 2, both vibrational frequencies expected in the IR, namely the antisymmetric stretching vibration and the two-fold degenerate deformation vibrations, can be observed. The symmetric stretching vibration is only Raman-active [56, 57].

Table 2: Fundamental vibrations, frequencies, and description for CO₂ [56, 57].

Vibration	Wavenumber / cm ⁻¹	Vibrational mode
ν_1	1388	Symmetric stretching vibration
ν_2	2349	Antisymmetric stretching vibration
ν_3	667	Deformation vibration

A non-linear triatomic molecule is water. The complex molecular vibrational pattern of the water molecule can be resolved into three simple harmonic components or normal modes ($3N-6 = 3$) that correspond directly to three absorption bands in the infrared spectrum (see Fig. 6 and Table 3) [56]. Because of the angular structure, the symmetric stretching vibration ν_1 is connected with a change of the center of charges, so that the already existing dipole moment is altered and the vibration is IR-active. In the antisymmetric stretching vibration ν_3 not only do the hydrogen atoms move but also the oxygen atom moves, to a necessarily lesser degree, for maintaining the center of mass. The low-frequency mode ν_2 corresponds to a bending of the molecule about the bond angle. It occurs at lower frequencies than do the two stretching modes, as it takes less energy to bend a bond than it does to stretch one [58]. The atomic displacements of these normal modes can be used to characterize the type of fundamental vibration giving rise to the infrared absorption.

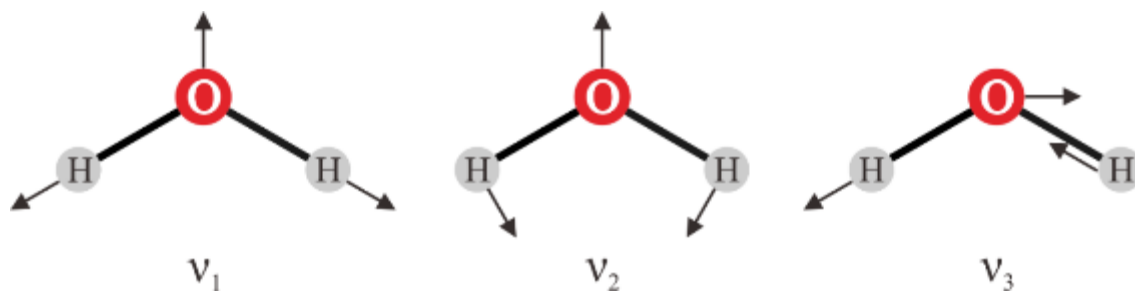


Fig. 6: Vibrational modes of water [56].

Table 3: Normal modes of vibration of water (gaseous) [56].

Vibration	Wavenumber / cm^{-1}	Vibrational mode
ν_1	3657	Symmetric stretching vibration
ν_2	1595	Deformation vibration
ν_3	3756	Antisymmetric stretching vibration

2.1.3 NIR absorption spectroscopy in liquids

The NIR region of the electromagnetic spectrum extends from the end of the visible spectral region (780 nm or 12820 cm^{-1}) to the beginning of the fundamental infrared spectral region (2500 nm or 4000 cm^{-1}). The most prominent absorption bands occurring in the NIR region are related to the overtone and combination bands of the fundamental molecular vibrations of C–H, N–H, O–H, and S–H functional groups. Therefore, most chemical species exhibit absorption band in NIR spectra region that can be used for both qualitative and quantitative purposes. NIR absorption bands are typically 10–100 times weaker than the corresponding fundamental mid-IR absorption bands. The weak nature of NIR absorptions in certain situations is an analytical advantage, e.g., in liquids such that sizable absorptions can be measured for layer thicknesses between 0.5 mm and 1 cm.

In the gaseous phase, rotation of the molecule is free and this leads to many rotational-vibrational combinations and millions of absorption lines. In the liquid phase, these rotations are limited by hydrogen bonding in the water molecule cluster and are reduced to three so-called libration modes that have weaker influences than the vibrations. Furthermore, it leads to a strong broadening of the absorption lines (Fig. 7b). The vibrational manifolds are broadened significantly due to the high density and the large number of collisions. Compared to the gas phase (Table 3) the main stretching band in liquid water is shifted to a lower frequency (ν_3 , 3490 cm^{-1} and ν_1 , 3280 cm^{-1}) [59] and the bending fre-

frequency increased (ν_2 , 1644 cm^{-1}) [60]. In Fig. 7a, the water vapor absorption lines are plotted at room temperature from 1.3 to $1.7 \text{ }\mu\text{m}$ based on the HITRAN database [61]. The spectral overlap of water absorption in the overtone ($2\nu_1$ and $2\nu_3$) and combination ($\nu_1+\nu_3$) bands in the near-infrared ($1.3\text{--}1.5 \text{ }\mu\text{m}$) with the emission characteristics of telecommunication diode lasers and optical fiber technology suggests a potential for relatively low-cost multi-wavelength absorption sensors. Yang et al. have successfully demonstrated four-color sensing of liquid film thickness, as well as liquid and gas phase temperature for pure water thin films in the NIR range [29, 32]. This thesis will focus on the application of this concept to monitor liquid thin film of aqueous salt and urea solutions. As ions dissolved in water and temperature change the internal structure of the water molecule cluster, the frequencies of the fundamental vibration and libration modes change and the light absorption spectrum of “pure” water changes with temperature and solute concentration [62]. Details of these will be discussed in chapter 3.

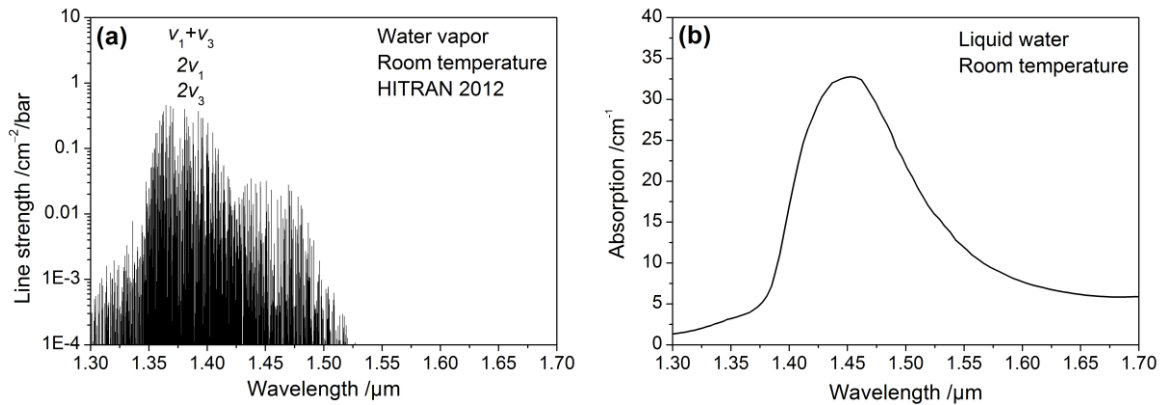


Fig. 7: Room temperature absorption spectra of (a) water vapor based on HITRAN 2012 database and (b) liquid water (path length: 1 mm) from 1.3 to $1.7 \text{ }\mu\text{m}$ [61, 63].

2.1.4 Beer-Lambert law

Laser absorption can be used to determine sample parameters of interest using the Beer-Lambert law. As depicted in Fig. 8, a beam of wavenumber $\tilde{\nu}$ with intensity $I_{\tilde{\nu}}$ is incident on an infinitesimal slab of absorbing liquid with thickness dz .

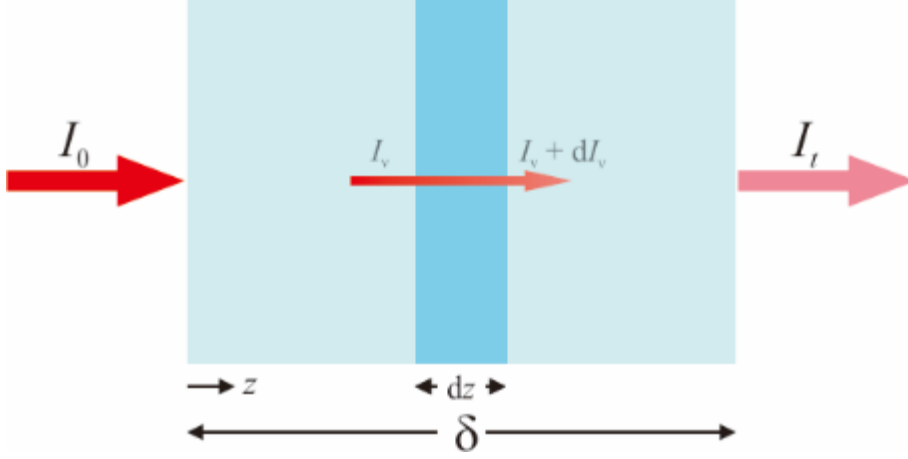


Fig. 8: Schematic of monochromatic light pass through an absorbing liquid [64].

In this thesis, wavenumber $\tilde{\nu}$ (in cm^{-1}) and wavelength λ (in nm) are both used to identify the emission wavelength of the laser. Then, the fractional attenuation of light, $dI_{\tilde{\nu}}$, is proportional to the local intensity, $I_{\tilde{\nu}}$, and the path length, dz , according to the relation:

$$dI_{\tilde{\nu}} = -n_L \sigma_L I_{\tilde{\nu}} dz \quad (15)$$

where n_L (in mol/cm^3) is the molar density of the absorbing species, σ_L the absorption cross section of the liquid at wavenumber $\tilde{\nu}$. Integrating Eq. (15) from $z = 0$ to δ , where δ is the thickness of the liquid layer (assumed here to be uniform) yields the Beer-Lambert law:

$$\tau(\tilde{\nu}) = \left(\frac{I_t}{I_0} \right)_{\tilde{\nu}} = \exp(-n_L \sigma_L \delta), \quad (16)$$

where $\tau(\tilde{\nu})$ is the transmittance at wavenumber $\tilde{\nu}$. If the light attenuation is only due to absorption, where I_t and I_0 are the light intensities with and without absorption. The absorbance, $A(\tilde{\nu}) = -\ln(I_t/I_0)_{\tilde{\nu}}$, is given as the product $n_L \sigma_L \delta$, with $k_{\tilde{\nu}}(w, T_L) = n_L \sigma_L$ the wavenumber-, solute concentration-, and liquid temperature-dependent absorption coefficient of the liquid has unit of inverse length (in cm^{-1}). For quantitative measurements, if the absorption cross-section is desired, the absorption spectra of the species must be known or measured directly (see following section).

2.2 Measurement of absorption spectra

In NIR absorption spectroscopy a beam of electromagnetic radiation passes through a liquid sample, one of its chemical bonds experiences only a change in vibrational energy, the number of photons passing through the sample decreases. A plot of absorbance caused by the decrease in number of photons as a function of the photon's energy is called an absorption spectrum. In this section, the FTIR spectrometer transmission measurement technique is described.

2.2.1 Spectrometer with broadband illumination

An absorption spectrum is usually recorded through transmission measurements or diffuse-reflectance measurements with an IR spectrometer. Absorption spectrometers are generally categorized into two configurations shown in Fig. 9. The difference between these two is the position of the sample relative to the device dispersing the incoming radiation. If the sample is placed in front of the spectral dispersion unit, as shown in Fig. 9a light with a broadband spectrum that is emitted from a thermal source is absorbed by the sample and is then introduced into a spectral dispersion unit to obtain the spectrum. In this case, both the light component of the wavelength of interest and the component of the unmeasured wavelength region irradiate the sample simultaneously; this may heat up the sample and change its physical characteristics. Therefore, this configuration is not recommended for measurement of thermally or photolytically sensitive samples. In the infrared the temperature of IR sources is, however, low enough to make this negative effect negligible [51]. However, these limitations may be overcome using the second design (see Fig. 9b). If the sample is placed after the spectral dispersion unit, the light first interferes with the pre-divided beam in an interferometer, and then illuminates the sample to obtain the intensity of absorbed light.

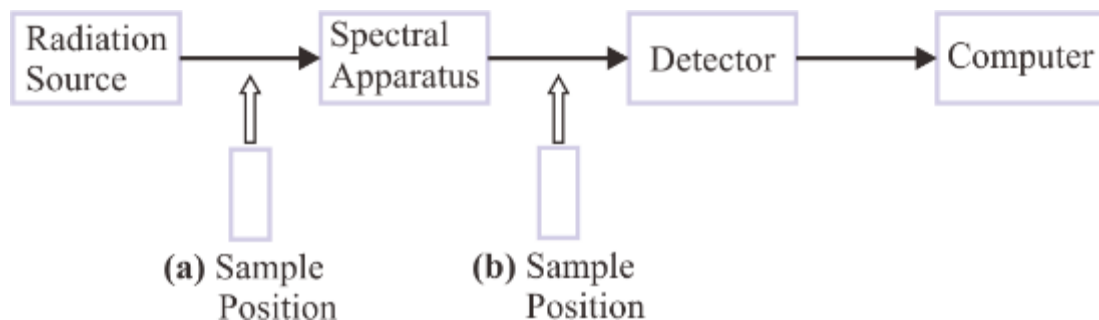


Fig. 9: Schematic design of an IR spectrometer: Sample is placed (a) in front of and (b) after the spectral dispersion.

2.2.2 FTIR spectroscopy

FTIR spectroscopy is a valuable tool for the nondestructive analysis of water-based solutions [65, 66]. The key concepts of this technique will be introduced in the following section.

In FTIR spectrometers, the spectrally coded transmitted radiation from a broadband source is modulated in a Michelson interferometer (two-beam interference), and the intensity vs. pathlength difference is converted by a Fourier transformation into spectral information (Fig. 10).

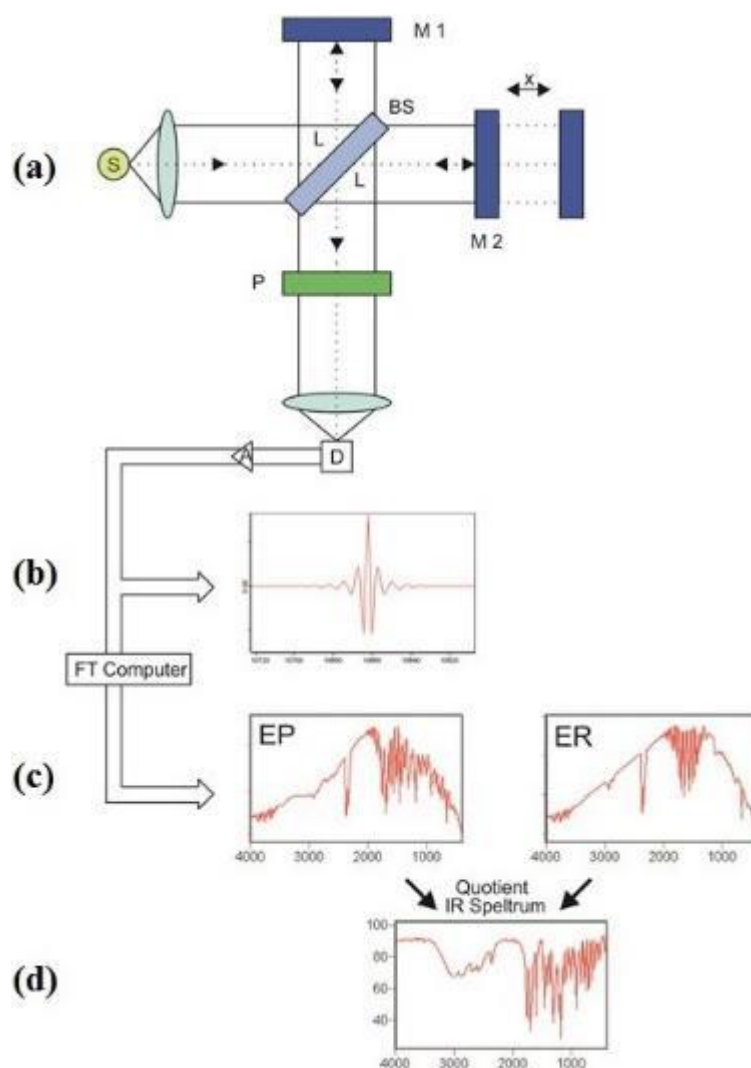


Fig. 10: (a) Schematics of a Michelson interferometer. S: source, D: detector, BS: beam splitter, M1: fixed mirror, M2: movable mirror, x: mirror displacement, P: Sample. (b) Measured interferogram by detector D. (c) ER: single channel reference spectrum measured through an empty sample compartment, EP: single channel spectrum of absorbing sample. (d) Transmittance spectrum equal to EP divided by ER [51].

Infrared light emitted by a source is directed to a beam splitter, where half of the light passes through while it reflects the other half. The reflected part of the beam travels to the fixed mirror M1 through a distance L , is reflected there and hits the beam splitter again after a total path length $2L$. The same happens to the transmitted part of the beam. However, as the reflecting mirror M2 of this interferometer arm is not fixed at the same position L but can be moved very precisely back and forth around L by a distance x , the total path length of this beam is accordingly $2(L + x)$. Thus when the two halves of the beam recombine again on the beam splitter they exhibit a path length difference or optical retardation of $2x$, i.e., the partial beams are spatially coherent and will interfere when they recombine. The beam leaving the interferometer is passed through the sample compartment and is finally focused on the detector D. The quantity actually measured by the detector is thus the intensity $I(x)$ of the combined IR beams as a function of the moving mirror displacement x , the so-called interferogram (see Fig. 10b).

To obtain a transmittance spectrum, three steps are necessary: (1) An interferogram measured without sample in the optical path is Fourier transformed and yields the so-called single channel reference spectrum $ER(\tilde{\nu})$ of Fig. 10c; (2) An interferogram with a sample in the optical path is measured and Fourier transformed. This yields the so-called signal channel sample spectrum EP of Fig. 10c. $EP(\tilde{\nu})$ looks similar to $ER(\tilde{\nu})$ but has less intensity at those wavenumbers where the sample absorbs; (3) The final transmittance spectrum $\tau(\tilde{\nu})$ is defined as the ratio $\tau(\tilde{\nu}) = EP(\tilde{\nu})/ER(\tilde{\nu})$, which is shown in Fig. 10d. Once the transmittance spectrum has been obtained, further quantitative analysis in the liquid, solid or gaseous samples can be performed based on the Beer-Lambert law (Eq. (16)).

The FTIR spectrometer has three advantages over other dispersive infrared spectrometers [67]:

1. Multiplex advantage: All of the spectral elements in FTIR spectrometer are measured simultaneously and many scans can be thereby completed and averaged in a shorter time than one scan on most dispersive instruments.
2. Jacquinot or throughput advantage: The FTIR spectrometer has no slit and does not limit the amount of light reaching the detector.
3. Connes advantage: The velocity of the moving mirror M2 is controlled using a laser, which is also used as a reference signal within the spectrometer. Furthermore, the interferogram of the laser is a constant sine-wave that provides the reference for both precision and accuracy of the spectrometer.

In this thesis, the absorption spectra of pure water and water solutions are measured using a FTIR spectrometer (Bruker, Vertex 80). The variation of the absorption spectrum of the

solutions with temperature and solute concentration provides the quantitative database for the multi-wavelength diode laser absorption sensor. This will be discussed in chapter 3 in detail.

2.2.3 Interference challenges

The measurement of an absorbance spectrum with an FTIR spectrometer is a two-stage process. First a reference spectrum is measured and then a sample spectrum. Measurements of absorption in liquid are mostly conducted using a quartz sample cell. According to Eq. (16), an accurate value of I_0 in the FTIR measurements is needed using the empty sample cell; when measuring liquid samples, the change of refractive index from air to liquid must be considered to convert the baseline measured with the empty cell to the true baseline of the filled cell. Previously, Porter et al. investigated this baseline offset to measure film thickness of liquid hydrocarbon fuels [28]. This situation is presented schematically in Fig. 11, where a light beam is shown passing through an empty cell (Fig. 11a) and through a cell containing the liquid (Fig. 11b).

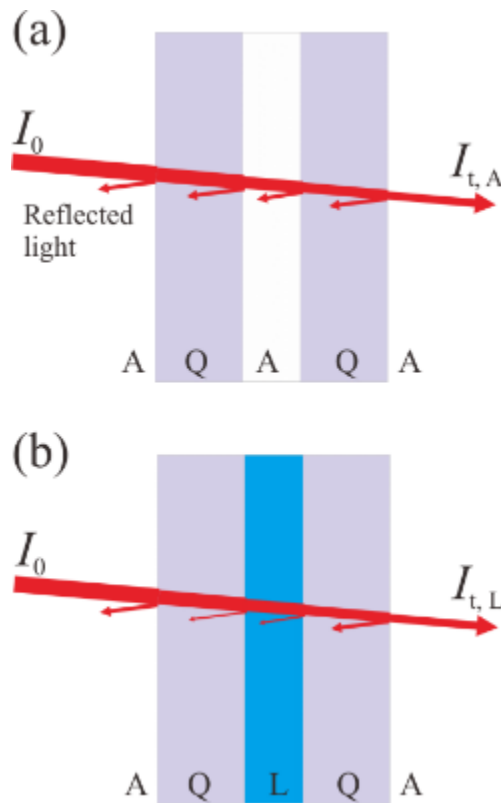


Fig. 11: Schematics of light transmission through (a) an empty sample cell and (b) a cell with liquid, A: air, Q: quartz, L: liquid

The transmittance, τ_{ij} , at the interface of two media (i and j representing A, Q, and L for air, quartz and liquid, respectively), can be determined using Fresnel's equation [68],

$$\tau_{ij} = \frac{4n_i n_j}{(n_i + n_j)^2} \quad (17)$$

where n_i and n_j are the real refractive indices of medium i and j, respectively. Neglecting multiple reflections within the window and the film, the light transmission through the windows and the empty cell $I_{t,A}$ can be approximated using Eq. (18), and the transmission through the cell with liquid, $I_{t,L}$, using Eq. (19):

$$I_{t,A} = I_0 \tau_{AQ} \tau_{QA} \tau_{AQ} \tau_{QA}, \quad (18)$$

$$I_{t,L} = I_0 \tau_{AQ} \tau_{QL} \tau_{LQ} \tau_{QA}, \quad (19)$$

where I_0 is the incident light intensity, and the transmittance subscripts are shown in Fig. 11. The measured transmittance is then given by:

$$\tau_{\text{FTIR}} = \left(\frac{I_{t,A}}{I_{t,L}} \right)_{\tilde{\nu}} = \frac{I_0 \tau_{AQ} \tau_{QL} \exp(-k(\tilde{\nu})\delta) \tau_{LQ} \tau_{QA}}{I_0 \tau_{AQ} \tau_{QA} \tau_{AQ} \tau_{QA}}. \quad (20)$$

Thus, the absorption coefficient can be expressed by

$$k(\tilde{\nu}) = \frac{1}{\delta} \left(-\ln \frac{\tau_{\text{FTIR}}}{\tau_{\text{QL}}^2 / \tau_{\text{QA}}^2} \right) = \frac{1}{\delta} \left(-\ln \frac{\tau_{\text{FTIR}}}{\alpha_{\text{Cal}}} \right), \quad (21)$$

where α_{Cal} is the transmission correction factor in FTIR measurement. In this work, the refractive index data of liquid water and water solutions are taken from Refs. [63, 69-72] to calculate the baseline offset for an accurate measure of absorption coefficient. This will be discussed in chapter 3.

3 Measurement of absorption spectra of aqueous solutions with FTIR

To develop quantitative diagnostics of liquid water solutions based on diode lasers, the broadband absorption spectra in the NIR spectral region of interest are required. FTIR spectrometers are appropriate instruments for this purpose providing absorption spectra with sufficient resolution. This accessory provides for the non-destructive measurement of samples. In the present work higher resolution spectra (2 cm^{-1}) at different temperatures were measured in our FTIR spectrometer (Bruker, Vertex 80) using a high-precision liquid sample cell (Hellma, 1 ± 0.005 mm optical path length). The probe temperature in the cuvette was measured using a mineral insulated thermocouple (Sheath diameter: 0.25 mm, TC Direct). The OPUS software provides the option to set the advanced and optics parameters. A list of the important measurement parameters that apply to the spectrometer configuration is shown in Table 4.

Table 4: Measurement parameters in the spectrometer configuration

Advanced / Optics Parameters	Settings
Resolution	2 cm^{-1}
Sample scan time	32 scans
Save data	$4000\text{--}8000\text{ cm}^{-1}$
Source setting	NIR source
Beam splitter	KBr
Aperture setting	3 mm
Detector setting	RT-DLaTGS
Scanner velocity	10 kHz

The following steps in the flow chart outline the procedure in the transmission measurement (Fig. 12). In this chapter the FTIR measurements of the temperature and concentration dependence of the NIR absorption in pure water, aqueous NaCl and urea solutions are presented.

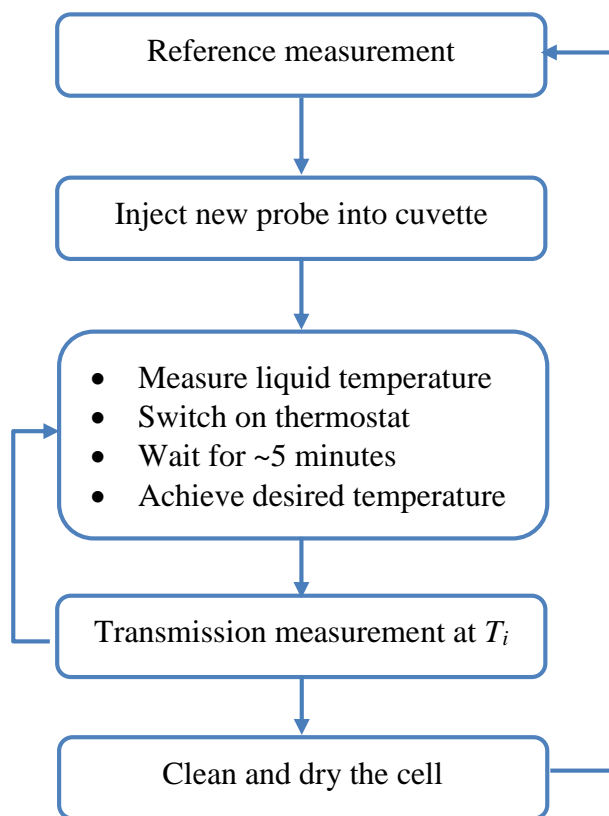


Fig. 12: Step-by-step flow chart for transmission measurement

3.1 Absorption of pure water

As discussed in section 2.2, liquid water exhibits broadband absorption from the OH-stretch vibrational bands in the NIR region due to the hydrogen bridge bonding and hindered rotations (Table 3). Compared to the gas phase the frequency of the fundamental vibration modes for liquid water are shown in Table 5.

Table 5: Fundamental vibrations and frequencies for liquid water at 298 K [73].

Vibration	Wavenumber / cm^{-1}	Vibrational mode
ν_1	3280	Symmetric stretching vibration
ν_2	1644	Deformation vibration
ν_3	3490	Antisymmetric stretching vibration

Hale et al. reported a review of the absorption spectrum of liquid water in the wavelength region between 0.2 and 200 μm [73] and Kou et al. presented a more detailed compilation in the NIR range [63]. More recently, Yang et al. reported the NIR absorption spectrum of liquid water for temperature between 298 and 348 K [32, 74]. In the measurements distilled water was filled into the 1-mm-pathlength cuvette with two optical windows and a double-jacket wall with flowing thermostating water kept the temperatures between 298 and 338 K. As seen in Eq. (21) (chapter 2), an accurate value of absorption coefficient can be calculated if the refractive indices of the different media (air, quartz, and liquid) are known in transmission measurements. The refractive indices of air and quartz are 1.0002 and 1.4458 near 1.4 μm , respectively. The refractive index data of liquid water was taken from [69] to calculate the baseline offset for an accurate measure of absorption coefficient. Based on the measured transmittance, the absorption coefficient of liquid water can be found and the spectrum at different temperatures is presented in Fig. 13. The spectra show a spectral blue shift of the peak absorbance of $\sim 5 \text{ cm}^{-1}/\text{K}$ with increasing temperature and a simultaneous slight absorbance increase [32, 74].

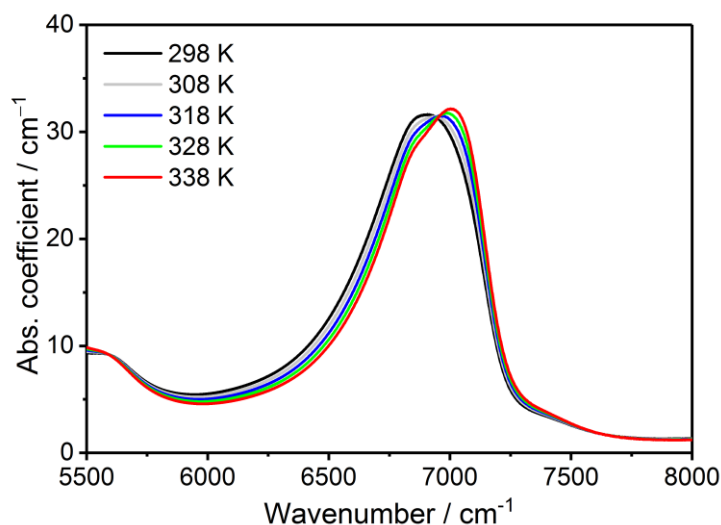


Fig. 13: NIR absorption spectrum of pure water in the range 5500–8000 cm^{-1} for temperatures between 298 and 338 K

3.2 Absorption of aqueous NaCl solutions

There is a long history of absorption studies of aqueous NaCl solutions. Lin et al. examined difference spectra to study the perturbation of water bands by NaCl solute versus temperature [63, 75-77]. Gowen et al. characterized the perturbation of pure H_2O absorption near the 1.4 μm NIR absorption feature by variations of temperature and NaCl concentra-

tion in terms of hydrogen bonding using multivariate curve resolution-alternating least squares (MCR-ALS) [78]. Despite this extensive earlier research, the database needed to be completed for the temperature and concentration ranges envisaged in this thesis. Thus, FTIR measurements of absorption in the spectral range 5500–8000 cm^{-1} as a function of NaCl concentration (0–26 wt%) and temperature (298–338 K) were conducted using the FTIR spectrometer (cf., Section 3.1) with the quartz sample cell. As discussed in section 2.2.3, a correction of measured transmission based on the matching of the refractive index is needed. Kamal et al. reported the effect of temperature on refractive index of salt solutions (Fig. 14) [79]. The change of the refractive index is very small, about 0.5%, in the temperature range from 298 to 228 K at a constant salt solution. Therefore, neglecting the temperature influence, the resulting transmission correction factors of NaCl solutions in FTIR measurement were calculated from the refractive index relating to the concentration [63, 80] (Table 6). Based on the measured transmittance, the absorption coefficient of water solutions can be found using Eq. (21) as present in Chapter 2.

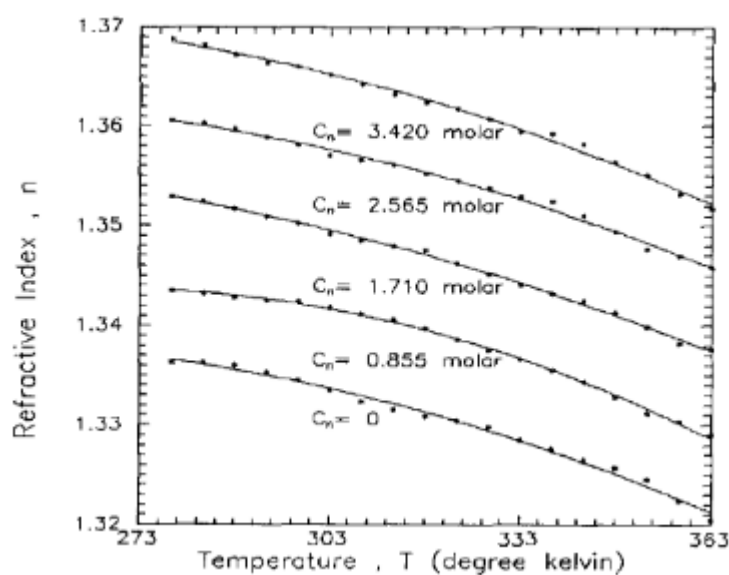


Fig. 14: Refractive index against temperature for pure water and four different concentration of NaCl [79]

Table 6: Correction factors of NaCl solutions at different solute concentrations

$w / \text{wt}\%$	$\alpha_{\text{Cal.}}$	$w / \text{wt}\%$	$\alpha_{\text{Cal.}}$
5	1.0669	20	1.0683
10	1.0674	26	1.0687
15	1.0679		

3.2.1 NIR spectra of aqueous NaCl solution at fixed temperature

Fig. 15a shows the NIR absorption coefficient of pure water (black solid line) and of aqueous NaCl solutions as a function of NaCl concentration (0–26 wt%, colored solid lines) at a fixed temperature of 298 K. The vertical error bars indicate a statistical error of 1% for two independent measurements on separate days.

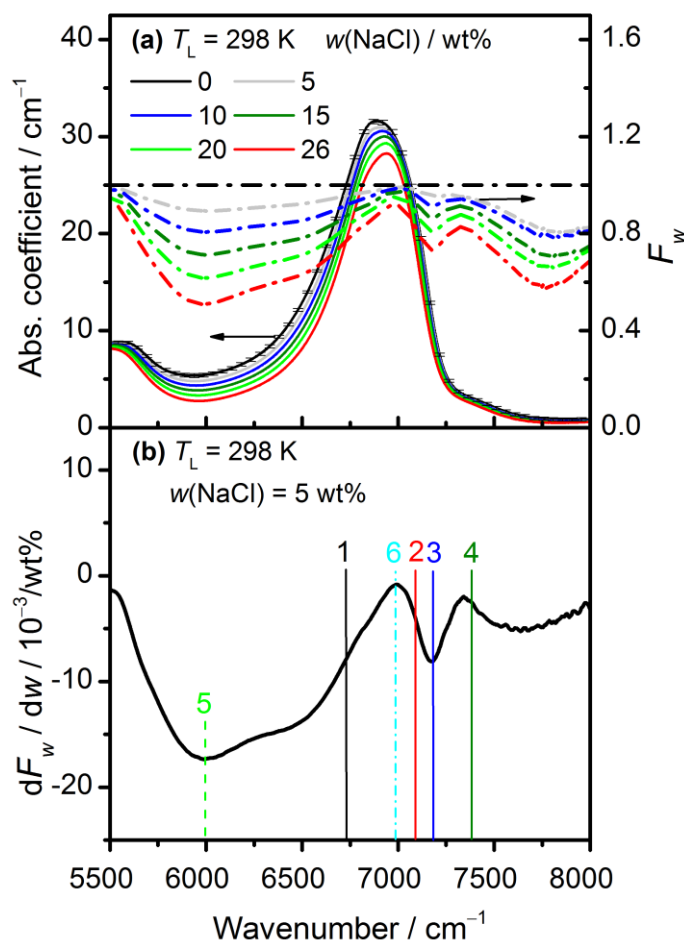


Fig. 15: (a) NIR absorption coefficient of pure water (black solid line) and aqueous NaCl solutions (5–26 wt%, given as $w(\text{NaCl})$ in the graphs) at 298 K measured via FTIR (colored solid lines), and their normalized absorption coefficient (with respect to pure water), F_w , (colored dashed lines). (b) Wavelength dependence of the derivative (with respect to NaCl mass fraction), dF_w/dw (solid line). The vertical solid lines numbered 1–4 in panel (b) denote laser frequencies utilized in the present thesis and the vertical dashed lines numbered 5 and 6 in panel (b) identifies a pair of laser frequencies for optimized sensitivity.

As NaCl is dissolved in water, water molecules form hydration shells around ions, and consequently the local hydrogen bond network is perturbed [81]. In this case, the absorption band is blue shifted by $\sim 2 \text{ cm}^{-1}/\text{wt}\%$ and the peak absorbance decreases due to the

change in the molecular interaction and the decrease in the number of water molecules per unit volume by changing the partial density [82], thereby changing the absorption coefficient as well (Fig. 15a). The absorption coefficient can be normalized with respect to that of pure water (at fixed T_L):

$$F_w(\tilde{\nu}_i) = k(\tilde{\nu}_i, w) / k(\tilde{\nu}_i, 0), \quad (22)$$

The changes of the spectra due to the increased solute concentration are more easily observed in normalized spectra, F_w , that are also plotted as colored dashed lines in Fig. 15a. The derivative of this ratio with respect to weight percent change of the salt, dF_w/dw , is plotted in Fig. 15b as a solid line, and this curve is useful to select the laser wavelengths sensitive (or insensitive) to NaCl concentration. From Fig. 15b, wavenumber pairs at the minimum (5985 cm^{-1}) and maximum (6991 cm^{-1}) respectively of dF_w/dw vs. wavenumber (marked as vertical line 5 and 6 respectively) are most promising for solute concentration measurement. The selection of a suitable combination of laser wavelengths for a multiple-wavelength sensor will be shown in detail in chapter 4.

3.2.2 Temperature dependence of NIR spectra of aqueous NaCl solution at fixed concentration

As with pure water [32, 83], the shape and magnitude of NIR absorption spectra of aqueous NaCl solutions depend on temperature [84]. Because hydrogen bond formation typically involves an increase in enthalpy and decrease in entropy, increasing temperature favors high-energy (i.e., OH band) configurations over lower-energy configuration. When the effects of hydrogen bond strength on NIR spectra are also considered, it is expected that increased temperature causes OH overtone and combination bands to shift to higher frequency, decrease in width, and increase in intensity [54].

The absorption coefficient of a 5 wt% aqueous NaCl solution was obtained at temperatures between 298 and 338 K (Fig. 16a). The absorption coefficient can be normalized with respect to room temperature (at fixed w):

$$F_T(\tilde{\nu}_i) = k(\tilde{\nu}_i, T_L) / k(\tilde{\nu}_i, 298 \text{ K}). \quad (23)$$

The spectra show a spectral blue shift of the peak absorbance of $\sim 5 \text{ cm}^{-1}/\text{K}$ with increasing temperature and a simultaneous slight absorbance increase [32]. Similarly, the temperature dependence is normalized for the 5 wt% solution in Fig. 16a by the curve for 298 K and

the derivative of the ratio, dF_T/dT_L , is plotted in Fig. 16b, which again is useful for sensor design. A (nearly) isosbestic point at 6937 cm^{-1} is identified in Fig. 16a where the absorption is almost independent of temperature; note that the position of such a point may depend on the salt concentration.

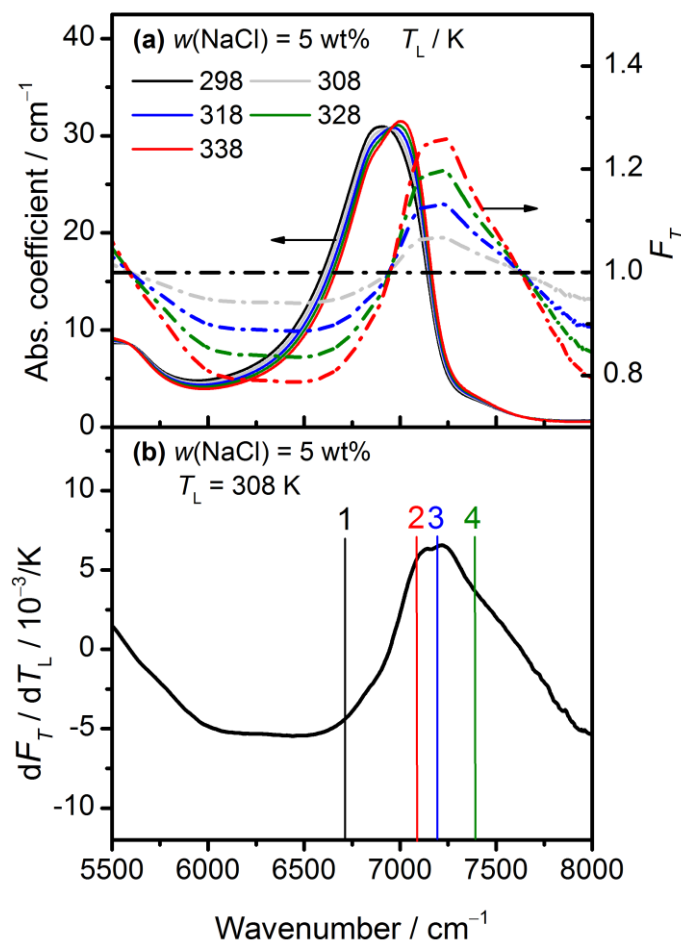


Fig. 16: (a) NIR absorption coefficient of aqueous NaCl solutions at 5 wt% as a function of temperatures (298–338 K, colored solid lines) and corresponding normalized (with respect to the room temperature spectrum) absorption coefficient, F_T (colored dashed lines). (b) Derivative of F_T with respect to the temperature of the liquid (solid line). The vertical solid lines numbered 1–4 in panel (b) denote laser frequencies utilized in the present thesis.

3.3 Absorption of aqueous urea solutions

NIR absorption spectra have been exploited to investigate changes in hydrogen bonds in aqueous solutions of urea [85, 86] where a characteristic shift is observed with increasing solute concentration or temperature in the broad region of the overtone and combination

peak near 1450 nm (6896 cm^{-1}) of the stronger hydrogen bonds. Dissolved urea provides additional spectral absorption in the region of the water absorption peak ($\sim 6900 \text{ cm}^{-1}$) because of weak NH vibrational bands ($2\nu_1, 2\nu_3, \nu_1+\nu_3$) [87]. Most previous investigations of aqueous urea solutions have been performed at either constant temperature or solute concentration and not in the spectral range required in this study. Thus, absorption measurements in the spectral range $5500\text{--}8000 \text{ cm}^{-1}$ as a function of urea mass fraction (0–40 wt%) and temperature (298–338 K) were conducted using the same FTIR spectrometer with the quartz sample cell (cf., section 3.1). Similarly, by taking the correction factors (Table 7) on the basis of refractive index data of water and urea solution from [69–72], the absorption coefficient can be accurately calculated from the measured transmission.

Table 7: Correction factors of urea solutions at different solute concentrations

$w / \text{wt}\%$	$\alpha_{\text{Cal.}}$	$w / \text{wt}\%$	$\alpha_{\text{Cal.}}$
5	1.0668	25	1.0684
10	1.0673	30	1.0687
15	1.0677	35	1.0690
20	1.0680	40	1.0692

3.3.1 NIR spectra of aqueous urea solution at fixed temperature

When temperature is constant, $k(\tilde{\nu}_i, w)$ is governed by both the concentration-dependent transmittance τ and the liquid film thickness (cf., Eq. (16)). Fig. 17a shows the NIR absorption coefficient of pure water (black solid line) and of aqueous urea solutions as a function of urea mass fraction (0–40 wt%, colored solid lines) at a fixed temperature of 298 K and a 1 mm sample thickness. The spectrum of urea remaining after subtracting the spectrum of a solution (40% by weight) from a properly scaled spectrum of pure water is presented in Fig. 17a by the black dotted line. Note, however, that the background subtraction is not perfect because of the perturbation urea has on the water absorption spectrum.

Similar to the absorption spectra of NaCl solutions (Fig. 15), the vertical error bars indicate a statistical error of 1% for two independent measurements on two separate days. When urea is dissolved in water, there are several effects that affect the absorption spectra including (1) change in the volumetric density of water; (2) interactions between urea and water molecules that influence the water absorption spectra; (3) absorption by the NIR-activity of

the NH group near the water peak [87-91]. With increasing urea concentration, the absorption coefficient decreases and the peak absorbance is shifted to lower wavenumbers by $\sim 2 \text{ cm}^{-1}/\text{wt}\%$ (Fig. 17a). The derivative, dF_w/dw , of the normalized spectra F_w with respect to a weight percent change of urea is plotted in Fig. 17b as a solid line and serves for selecting laser wavelengths sensitive (or insensitive) to urea concentration. Two (nearly) isosbestic points at 6626 and 6767 cm^{-1} are identified in the region of high absorption in Fig. 17b where the absorption coefficient at that temperature is almost independent of solute concentration.

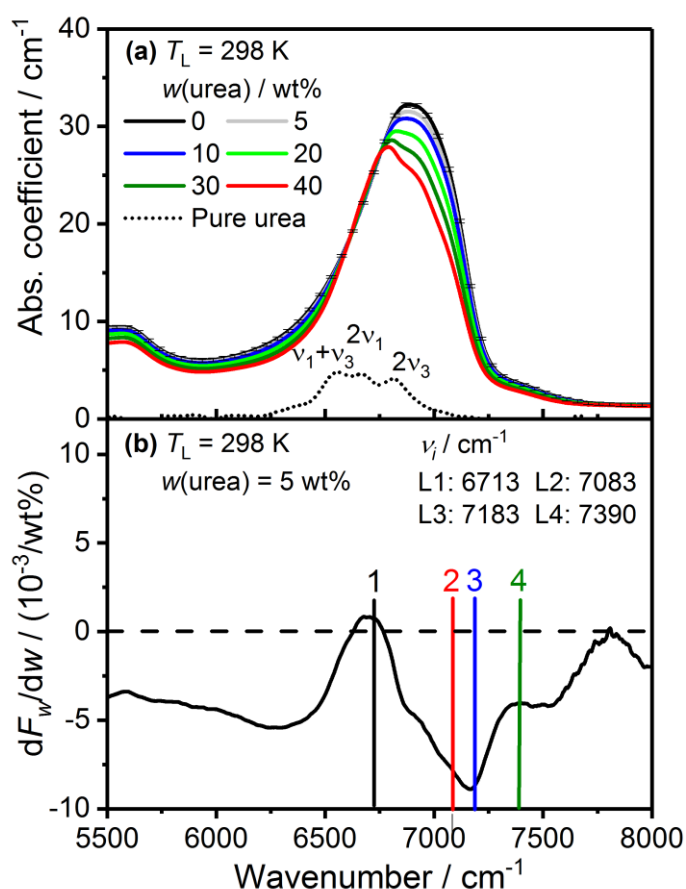


Fig. 17: (a) NIR absorption coefficient of pure water (black solid line) and aqueous urea solutions (5–40 wt%, given as $w(\text{urea})$ in the graph, colored solid lines) at 298 K. (b) Wavelength dependence of the derivative (with respect to urea mass fraction), dF_w/dw (solid line), where F_w is the normalized absorption coefficient with respect to pure water. The vertical solid lines numbered 1–4 in panels (b) denote laser wavenumbers utilized in the present thesis.

3.3.2 Temperature dependence of NIR spectra of aqueous urea solution at fixed concentration

As with pure water [32, 74, 92-94] and the case of NaCl (see Chapter 3.2.2), the shape and magnitude of the absorption spectra of aqueous urea solutions depends on temperature [90]. Temperature-dependent absorption coefficients of a 5 wt% solution are presented in Fig. 18a in the range 298–338 K.

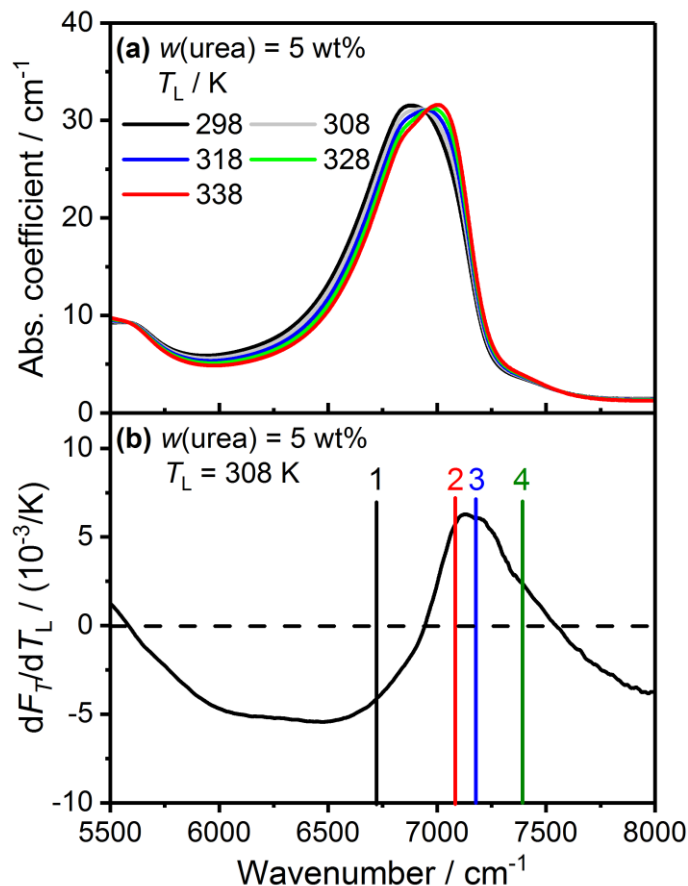


Fig. 18: (a) NIR absorption coefficient of a 5 wt% aqueous urea solution as a function of temperature (298–338 K, colored solid lines). (b) Derivative of F_T (normalized absorption coefficient with respect to room temperature) with respect to the temperature of the liquid (solid line). The vertical solid lines numbered 1–4 in panels (b) denote laser wavenumbers utilized in the present thesis.

Just as known for pure water (cf., Fig. 13) and the NaCl solution (cf., Fig. 16), with increasing temperature the absorption feature of urea solutions shifts towards higher wavenumbers by ~ 4 cm⁻¹/K. Similarly, the derivative of the normalized spectra F_T with respect to temperature of the liquid, dF_T/dT_L , is plotted in Fig. 18b as a solid line, which again is

useful for sensor design. A (nearly) isobestic point near the peak of the water band in Fig. 18b is identified at 6944 cm^{-1} , where for this solute concentration the absorption is almost independent of temperature.

3.4 Uncertainty analysis in measured absorption coefficient

Understanding the experimental uncertainty for various optical measurements is important for determining the precision and accuracy of the results that have been obtained. This section describes the general error propagation equation and its application for estimating uncertainties in FTIR measurements.

When a measured quantity, x , is a function of multiple independent variables $u, v, \dots, x = f(u, v, \dots)$, then the propagation of uncertainty in each of the variables produces an overall uncertainty for x . If the independent variables are also uncorrelated, then the error propagation equation for x is given by [95]

$$\Delta x \approx \sqrt{\left(\frac{\partial x}{\partial u} \Delta u\right)^2 + \left(\frac{\partial x}{\partial v} \Delta v\right)^2 + \dots}, \quad (24)$$

where Δx is the uncertainty in x , Δu is the uncertainty in u , etc.

In the FTIR data of an aqueous solution, according to Eq. (16), the measured absorption coefficient is a function of the solute mass fraction, liquid temperature, path length, and measured transmission. Using the assumption that all independent variables are uncorrelated, the uncertainty in the measured absorption coefficient can be determined by

$$\Delta k = \sqrt{\left(\frac{\partial k}{\partial \tau} \Delta \tau\right)^2 + \left(\frac{\partial k}{\partial w} \Delta w\right)^2 + \left(\frac{\partial k}{\partial T_L} \Delta T_L\right)^2 + \left(\frac{\partial k}{\partial \delta} \Delta \delta\right)^2}, \quad (25)$$

and the normalized absorption coefficient uncertainty becomes

$$\sigma_k = \frac{\Delta k}{k} = \sqrt{\sigma_\tau^2 + \sigma_w^2 + \sigma_\delta^2 + \left(\frac{\partial k/k}{\partial T_L} \Delta T_L\right)^2}. \quad (26)$$

The first three terms are the same for all transitions with $\sigma_\tau \approx 1\%$, $\sigma_w \approx 0.1\%$, $\sigma_\delta \approx 0.5\%$. The temperature measurement uncertainty ΔT_L is taken from the thermocouple specifications (TC Direct) as 0.4%. The uncertainty for the measured absorption coefficient for all lines is then about 1.2%.

4 Measurement of liquid films in transmission

The content of this chapter is derived from own publications [96, 97].

In this chapter a multi-wavelength near-infrared diode-laser absorption sensor is presented for real-time monitoring of the thickness, solution concentration, and temperature of thin films of water solutions.

4.1 Measurement strategy

In fixed-wavelength absorption measurements of liquid films, the laser light intensity decreases as it passes through the absorbing liquid, and Beer-Lambert's law relates the amount of light absorbed by the liquid to film thickness δ , liquid temperature T_L and solute concentration w . Additionally, non-specific transmission loss (light scattering, dirty optics, beam steering) must be taken into account [29]. In this case, the measured relative transmission τ is

$$\tau(\tilde{\nu}_i) = \left(\frac{I_t}{I_0} \right)_{\tilde{\nu}_i} = (1-u) \exp(-k(\tilde{\nu}_i, w, T_L) \delta), \quad (27)$$

where I_0 and I_t are the incident and transmitted light intensities, respectively, and u is the non-specific transmission loss. One contribution to the unspecific losses is reflection from the surfaces and liquid-quartz interfaces. These reflection losses can potentially be wavelength dependent due to changes in the refractive index of the liquid near an absorption feature [98]. However, in the case of liquid water or aqueous solutions, the real part of the refractive index varies by less than 0.3% from 5500 to 7500 cm^{-1} . Therefore, we assume that these non-specific transmission losses are the same for all sensor wavelengths. $k(\tilde{\nu}_i, w, T_L)$ (in cm^{-1}) is the spectral absorption coefficient of the liquid at wavenumber $\tilde{\nu}_i$ in dependence of temperature and solute concentration. For two wavelengths ($\tilde{\nu}_k, \tilde{\nu}_l$), the transmittance ratio ($\tau(\tilde{\nu}_k)/\tau(\tilde{\nu}_l)$) reduces to a function of temperature, solute concentration, and film thickness as shown in the following equations:

$$\frac{\tau(\tilde{\nu}_k)}{\tau(\tilde{\nu}_l)} = \exp((k(\tilde{\nu}_l, w, T_L) - k(\tilde{\nu}_k, w, T_L)) \delta). \quad (28)$$

In the work reported here, two limiting cases of thin film measurements are considered: (1) those with variable solute concentration at constant temperature and (2) those with variable

temperature at constant solute concentration. Thus, the measurement of δ , T_L , and w of the sample for each case reduces to the measurement of three unknowns using transmission measurements at three wavelengths of the four lasers in the sensor suite. As the solute concentration or liquid temperature is known, the logarithmic ratio $R(X)$ reduces to the ratio of the absorption coefficient differences of selected wavenumbers $\tilde{\nu}_k$, $\tilde{\nu}_l$, and $\tilde{\nu}_m$:

$$R(X) = \frac{\ln(\tau(\tilde{\nu}_k)/\tau(\tilde{\nu}_l))}{\ln(\tau(\tilde{\nu}_k)/\tau(\tilde{\nu}_m))} = \frac{k(\tilde{\nu}_l, X) - k(\tilde{\nu}_k, X)}{k(\tilde{\nu}_m, X) - k(\tilde{\nu}_k, X)}. \quad (X = w \text{ or } T_L) \quad (29)$$

As can be seen in the above equation, $R(X)$ is a function of w or T_L only. Therefore, one of the two desired parameters X can be determined from the experimentally determined transmittance and the absorption coefficient of aqueous solution at selected wavelengths. The liquid film thickness can then be determined when inserting the calculated X into Eq.(28):

$$\delta = \frac{\ln(\tau(\tilde{\nu}_k)/\tau(\tilde{\nu}_l))}{k(\tilde{\nu}_l, X) - k(\tilde{\nu}_k, X)}. \quad (30)$$

4.2 Design of sensor to characterize aqueous solutions of NaCl

The wavelength of individual single-mode, DFB telecommunications-style diode lasers can only be tuned approximately 50 cm^{-1} . Therefore, the practical sensor design considered here uses only a few (four) fixed laser wavelengths.

Table 8: Center wavenumber of diode lasers used and fitting coefficients characterizing the respective concentration dependences of absorption coefficients (see text).

Laser	Center wavenumber / cm^{-1}	Fitting coefficient $T_L = 298 \text{ K}$ (Eq. (31))			Fitting coefficient $w = 5 \text{ wt}\%$ (Eq. (32))	
		a_i	b_i	c_i	d_i	e_i
1	6713	–	–		52.70	–0.10
2	7083	24.13	–0.04	-4.06×10^{-3}	13.50	0.12
3	7183	11.44	–0.07	-1.28×10^{-3}	–	–
4	7390	3.65	–0.02	-8.82×10^{-5}	0.40	0.01

In this thesis we focus on the measurement of liquid films; thus the wavelength of each of these lasers is chosen to avoid absorption by gas-phase water vapor above the liquid (cf.,

Fig. 7). In our laboratory the four laser wavelengths used previously were limited for the characterization of thin films of pure water [99], their center wavelengths are listed in Table 8 and are indicated by vertical solid lines in Fig. 15b and Fig. 16b. It is important to note that the lasers listed in Table 8 are thus not the optimum choice for these measurements. However as shown below, these laser wavelength choices were suitable for a successful proof-of-concept demonstration of the sensor strategy.

4.2.1 Measurement of solute concentration and film thickness at constant liquid temperature

If the target of the measurement is the NaCl concentration, then the sensitivity of the ratio of transmission of light from a potential line pair will be large when (dF_w/dw) is large. For example, the ratio of transmission of lasers 2 and 3 shows a significant variation with NaCl concentration (see Fig. 15b). The FTIR data were used to determine the transmission of each laser, and Fig. 19a illustrates the details of the variation in F_w with NaCl concentration. Although the normalized absorption coefficient F_w for each of the lasers decreases with increasing NaCl concentration there is enough variation to use this ratio to determine the NaCl concentration.

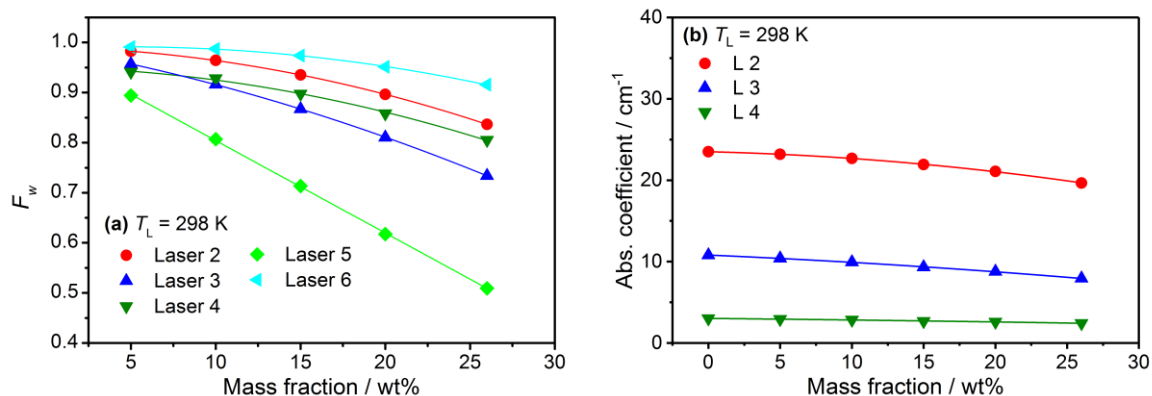


Fig. 19: (a) NaCl-concentration dependence (at 298 K) of the normalized (with respect to pure water) coefficient F_w at the five chosen wavenumber positions (Laser 2&3&4: available diode lasers, Laser 5&6: potential optimal wavenumbers) together with their polynomial fit. (b) Concentration dependence of the absorption coefficient at 298 K for the three chosen wavenumbers of lasers 2, 3 and 4; solid lines are second-order polynomial fits to the data points (cf., Table 8).

The sensitivity could be optimized if the minimum absorption coefficient (5985 cm^{-1} , line 5 in Fig. 15b and Fig. 19a) and the maximum absorption coefficient (6991 cm^{-1} , line 6 in Fig. 15b and Fig. 19a) were used instead. Fig. 19b shows the mass-fraction dependence (at

298 K) of the absorption coefficient for the wavenumber positions of our available lasers 2&3&4 together with second-order polynomial fits:

$$k(\tilde{\nu}_i, w) = a_i + b_i w + c_i w^2, \quad i = 2, 3, 4, \quad (31)$$

where a_i , b_i and c_i are the respective fitting coefficients at wavenumber $\tilde{\nu}_i$ (cf., Table 8).

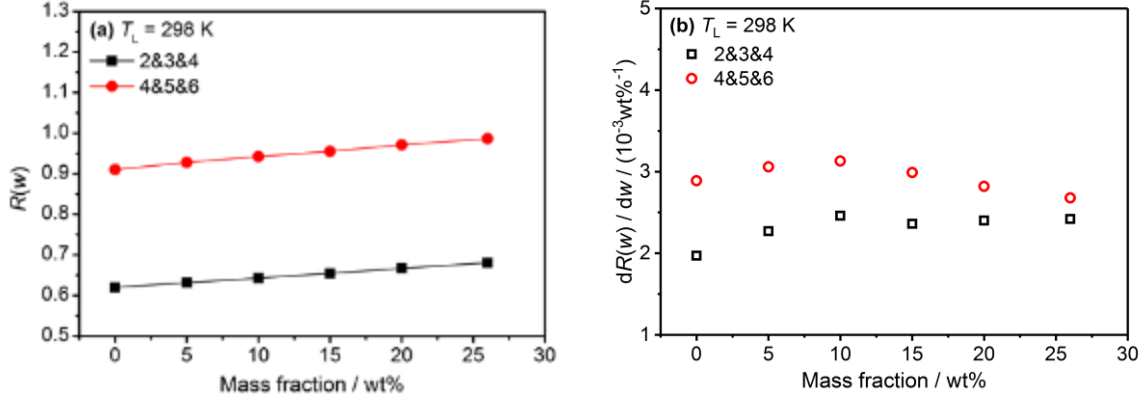


Fig. 20: (a) Logarithmic transmittance ratio $R(w)$ at 298 K using combinations of lasers 2&3&4 and 4&5&6. (b) Comparison for the sensitivity, $(dR(w)/dw)$, of the logarithmic transmittance ratio $R(w)$ (see text) used for NaCl concentration measurement when lasers 2&3&4 (open squares) and 4&5&6 (open circles) are employed, respectively.

By taking a ratio of the transmittance at selected wavelengths, the parameter u can be eliminated. From the logarithmic ratio $R(X)$, the NaCl mass fraction w , δ , and u can be obtained from known fitting coefficients (a_i , b_i , and c_i) and measured τ quantities using lasers 2, 3, and 4 (Eq. (29) and Eq. (30)).

A measure for the sensitivity of the measurement with respect to w is given by the derivative $dR(w)/dw$. Optimal wavelengths (denoted as laser 5 and 6 in Fig. 15b) near the maximum and minimum of the value dF_w/dw could be combined with laser 4 to determine δ and w , instead of the current combination of lasers 2&3&4. The variation of $(dR(w)/dw)$ with mass concentration for these two combinations is plotted in Fig. 20b. The comparison reveals that the use of laser 4, and the optimum laser wavelengths 5 and 6 exploit a stronger dependence on concentration, especially in the lower concentration range between 0 and 10 wt%, and improved measurements of liquid film thickness and solute concentration would be possible.

4.2.2 Measurement of liquid film temperature and film thickness at constant solute concentration

As in the case of a fixed temperature (Fig. 16a), ratio spectra were formed by normalizing with the spectrum at 298 K of the same solution, $F_T(\tilde{\nu}_i) = k(\tilde{\nu}_i, T_L)/k(\tilde{\nu}_i, 298 \text{ K})$, (dashed lines in Fig. 16a). Again, the intensity variation with respect to temperature of the 5 wt% solution spectrum is visualized by the derivative, dF_T/dT_L , presented in Fig. 16b. Laser 1, 2, and 3 are positioned close to the two extrema of the dF_T/dT_L curve (at 6500 and 7183 cm^{-1} , respectively), and laser 2 has larger absorption than laser 3. Therefore, lasers 1&2 were used to determine liquid film thickness and temperature. Since the wavelength of laser 4 coincides with a low absorption coefficient in the liquid, just as in the constant temperature case, the transmission at this wavelength was combined with laser 1&2 to infer the unknown, non-specific transmission loss u (Eq. (27)).

Fig. 21a shows the temperature dependence of the respective normalized spectral intensities (together with their linear fits as solid lines) as derived from the spectra presented in Fig. 16 for the wavenumber positions of the four available lasers 1, 2, 3, and 4. The temperature dependence of the absorption coefficient at these wavelength positions is presented in Fig. 21b with their linear fit:

$$k(\tilde{\nu}_i, T_L) = d_i + e_i T_L, \quad i = 2, 3, 4 \quad (32)$$

where d_i and e_i are the respective fitting coefficients at wavenumber $\tilde{\nu}_i$ (cf., Table 8).

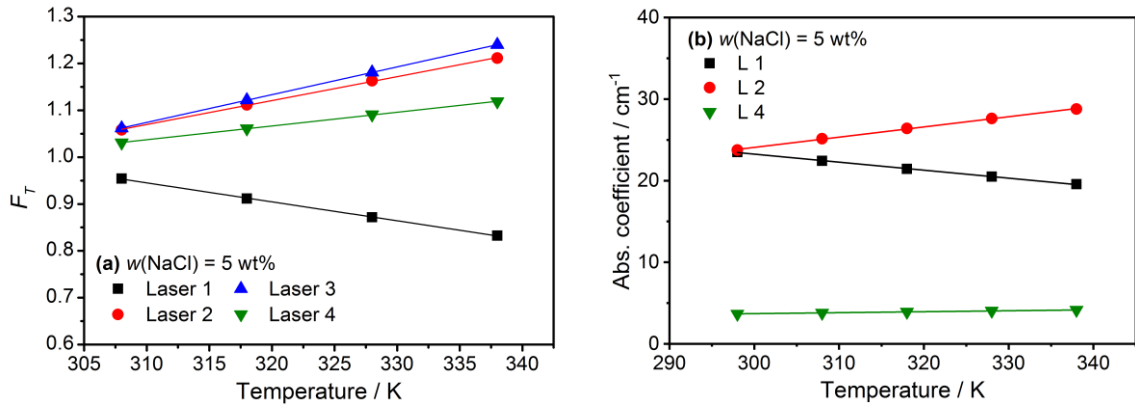


Fig. 21: (a) Liquid temperature dependence (at a given mass fraction of 5 wt%) of the normalized coefficient F_T at three chosen wavenumbers together with their linear fit. (b) Temperature dependence of the absorption coefficient in aqueous NaCl solutions (5 wt%) at three chosen wavenumbers together with linear fits.

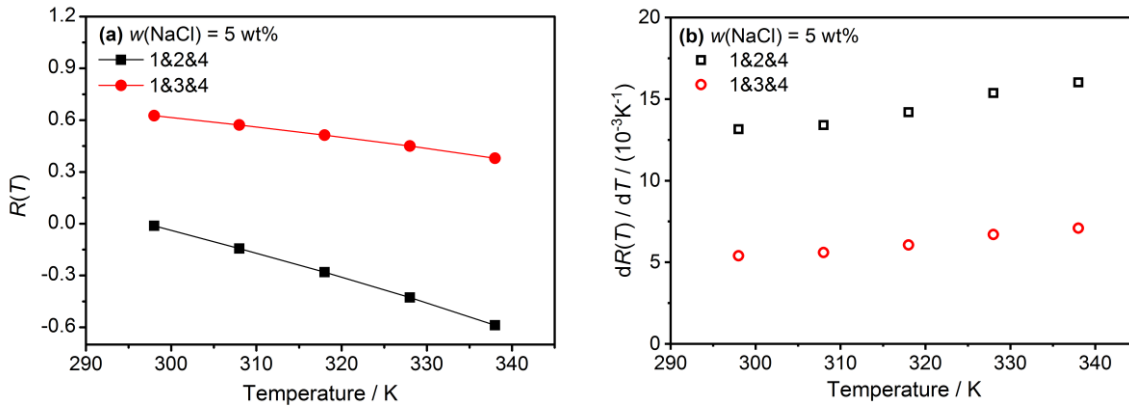


Fig. 22: (a) Logarithmic transmittance ratio $R(T)$ at 5 wt% using combinations of lasers 1&2&4 and 1&3&4. (b) Comparison for the sensitivity, $(dR(T)/dT_L)$, of the ratio $R(T)$ with respect to temperature using combinations of lasers 1&2&4 (filled squares) and 1&3&4 (open circles), respectively.

Liquid film thickness and temperature were then determined from the measured transmittance at the three chosen laser wavelengths by solving the logarithmic ratio $R(X)$, where $X = T_L$ (Eq. (29) and Eq. (30)).

The variation with temperature of this ratio, $dR(T)/dT_L$, calculated for the combination of laser wavelengths 1&2&4 and plotted in Fig. 22b (open black squares), increases with the temperature of the liquid. The variation of $(dR(T)/dT_L)$ with temperature for the combination of wavelengths 1&3&4 is plotted in Fig. 22b as open red circles. The comparison reveals that the wavelength combination 1&2&4 exhibits higher magnitude, and therefore would be the preferred laser wavelength selection for the variable temperature case.

4.3 Design of sensor to characterize aqueous solutions of urea

4.3.1 Measurement of urea concentration and film thickness at constant liquid temperature

For the selection of optimum wavelengths for a multi discrete-wavelength sensor, the variation of absorption with temperature and urea concentration were measured using heated thin-film cuvettes and a FTIR spectrometer in the range between 5500 and 8000 cm^{-1} as described in chapter 3.

When the temperature is fixed, it is important to select wavenumber pairs with a large difference in (dF_w/dw) to achieve good sensitivity for the concentration measurement. Laser 1, 2, and 3 are positioned around the extrema (at 6701 and 7160 cm^{-1}) of the (dF_w/dw) curve, and laser 2 has larger absorption than laser 3 (Fig. 17b) to provide sufficient signal-

to-noise ratio for thin film measurements. Thus, lasers 1 and 2 were used to determine liquid concentration and film thickness. Consider that laser 4 has a low absorption coefficient in the liquid; the transmission at this wavelength was combined with laser 1 and 2 to infer the unknown, non-specific transmission loss u (Eq. (27)).

In fixed-wavelength absorption measurements, the transmittance of each laser is measured simultaneously with liquid temperature, concentration, and path length being the same for each wavelength. Fig. 23a shows the concentration dependence (at 298 K) of the absorption coefficient for the four lasers together with linear fits to the data points:

$$k(\tilde{\nu}_j, w) = a_j + b_j w, j = 1, 2, 3, 4, \quad (33)$$

where a_j and b_j are the respective fitting coefficient at wavenumber $\tilde{\nu}_j$ (Table 9).

Table 9: Center wavenumbers of the diode lasers utilized in the present experiments and fitting coefficients characterizing the respective temperature dependences of the absorption coefficients (see text).

Laser	Center wavenumber / cm^{-1}	Fitting coefficient $T_L = 298 \text{ K}$ (Eq. (33))		Fitting coefficient $w = 5 \text{ wt\%}$ (Eq. (34))	
		a_j	b_j	c_j	d_j
1	6713	24.61	0.02	55.35	-0.10
2	7083	24.32	-0.21	-15.35	0.13
3	7183	11.45	-0.10	-8.88	0.07
4	7390	3.66	-0.02	0.84	0.01

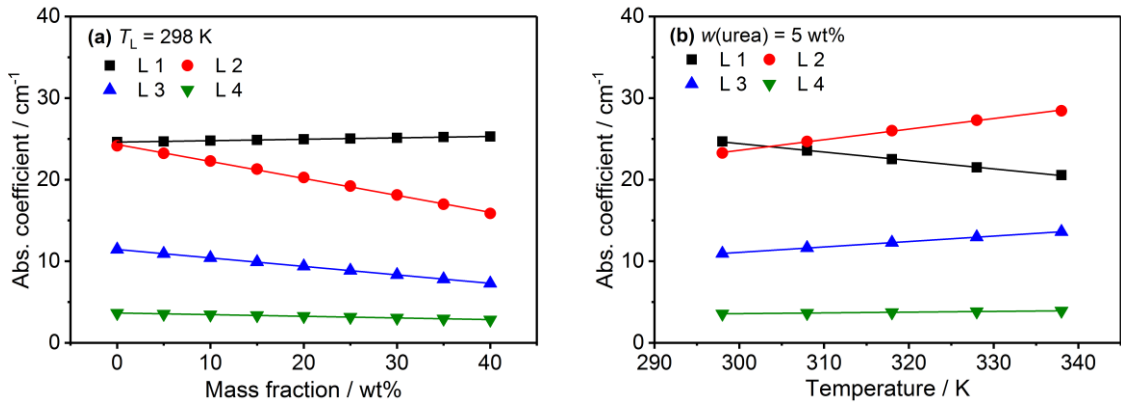


Fig. 23: (a) Concentration dependence of the absorption coefficient at 298 K for the four wavenumbers; solid lines are linear fits to the data points. (b) Temperature dependence of the absorption coefficient in urea water solution (5 wt%) at the four wavenumbers together with linear fits.

Following the strategy outlined in section 2, the urea mass fraction w and liquid film thickness δ can be determined from the known fitting coefficients (a_j and b_j) and experimentally determined transmittance values, $\tau(\tilde{\nu}_i)$, using lasers 1, 2, and 4 (Eq. (29) and (30)).

Combinations of laser wavelengths 1, 2, and 4 and 1, 3, and 4 are two choices of the currently available lasers. Fig. 24a shows the logarithmic transmittance ratio $R(w)$ using these two combinations. The sensitivity of the measurement with respect to w using these two combinations can be evaluated through the derivative, $dR(w)/dw$ (Fig. 24b). The comparison reveals that the wavelength combination 1, 2, and 4 exhibits a stronger dependence on concentration, and therefore would be preferred in the concentration measurements.

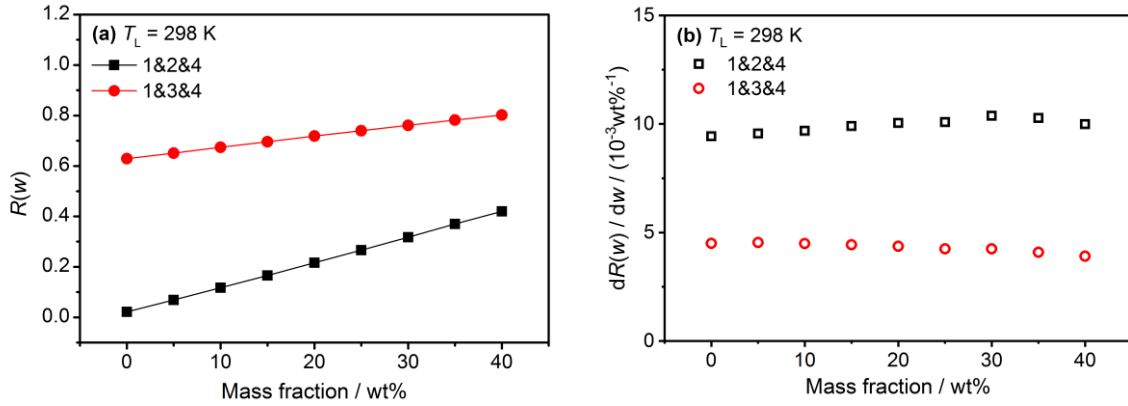


Fig. 24: (a) Logarithmic transmittance ratio $R(w)$ at 298 K using combinations of lasers 1&2&4 and 1&3&4. (b) Variation with mass fraction of the sensitivity, $(dR(w)/dw)$, with respect to mass fraction change of the logarithmic transmittance ratio $R(w)$.

4.3.2 Measurement of liquid temperature and film thickness at constant urea concentration

Similar to the concentration measurements at a fixed temperature, ratio spectra were formed by normalizing the temperature-dependent spectra with the spectrum at 298 K of the same solution. Again, the intensity variation with respect to temperature of the 5 wt% solution spectrum is visualized by the derivative dF_T/dT_L presented in Fig. 25b. Laser 1, 2, and 3 are positioned close to the two extrema of the dF_T/dT_L curve (6500 and 7133 cm^{-1}), and laser 2 is more strongly absorbed than laser 3 (cf., Fig. 18a). Therefore, lasers 1 and 2 were used to determine liquid film thickness and temperature, and the transmission at the wavelength of laser 4 was again combined with lasers 1 and 2 to infer the unknown, non-specific transmission loss u (Eq. (27)). The temperature dependence of the absorption coef-

efficient in urea water solution (5 wt%) at these wavelength positions is presented in Fig. 23b with their linear fit:

$$k(\tilde{\nu}_j, T_L) = c_j + d_j T_L, j = 1, 2, 3, 4, \quad (34)$$

where c_j and d_j are the respective fitting coefficients at wavenumber $\tilde{\nu}_j$ (cf., Table 9).

Similar to the concentration measurement, liquid temperature and film thickness can be obtained from the measured transmittance at the three laser wavelengths by solving the temperature-dependent logarithmic ratio $R(T)$ (Eq. (29) and (30)).

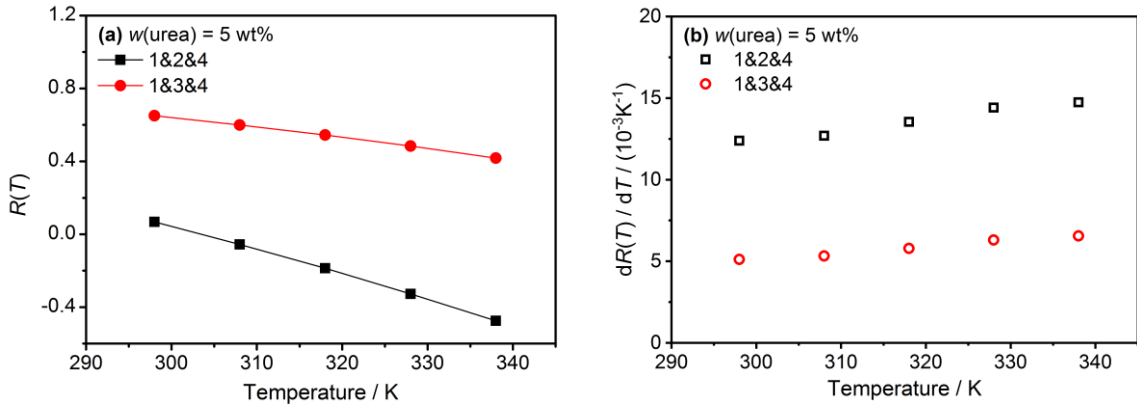


Fig. 25: (a) Logarithmic transmittance ratio $R(T)$ (at 5 wt%) using combinations of lasers 1&2&4 and 1&3&4. (b) Comparison for the sensitivity of the ratio $R(T)$ with respect to temperature, $(dR(T)/dT_L)$, using the two combinations.

The temperature dependence of the derivative $dR(T)/dT$ for the two combinations of laser 1, 2, and 4 and 1, 3, and 4 is plotted in Fig. 25b. Similarly, the comparison reveals that the wavelength combination 1, 2, and 4 exhibit a stronger dependence on temperature. Therefore, this wavelength combination would be preferred in the temperature measurements.

4.4 Experimental setup of multiplexed diode laser absorption sensor

A four-wavelength laser absorption sensor to characterize the thickness, temperature and solute concentration of the film was constructed and tested for liquid thin films with known thickness, temperature and solute concentration using lasers 1–4 in Table 8 and Table 9. The laser packages (14-pin butterfly) are placed in ILX Lightwave mounts (LDM-4984). The laser wavelength and intensity are controlled by a combination of temperature and injection current using a laser controller (ILX, LDC-3908). The diode laser absorption sensor assembly is depicted in Fig. 26.

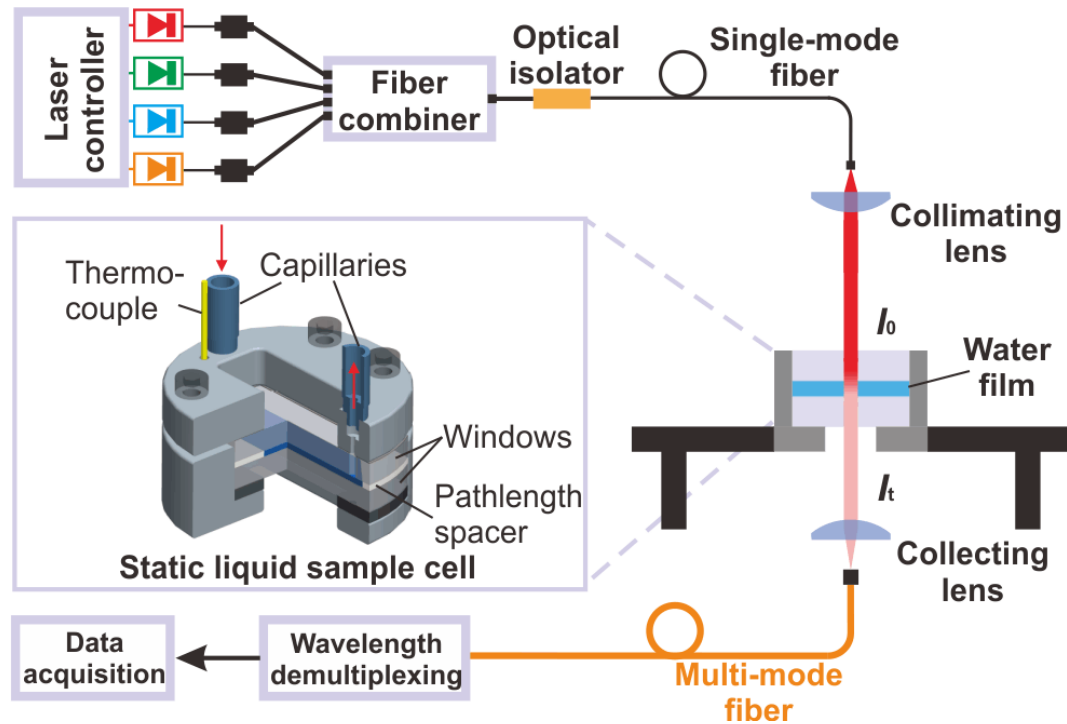


Fig. 26: Multiplexed diode laser absorption sensor for measurement of liquid film parameters.

The four distributed feedback (DFB) diode lasers (NEL) are wavelength-multiplexed into a single-mode fiber (9 μm core) using a 4 \times 1 fused combiner (Laser 2000). Out of the fiber the beams are collimated, then passed vertically through the liquid film formed between the quartz windows of a thin cuvette (LOT, GS20510, see inset in Fig. 26) at an angle of 2 $^\circ$ with respect to the plate normal to avoid etalon effects. The transmitted light is collected and focused into a 400 μm -core multimode fiber with a numerical aperture (NA) of 0.39 (Thorlabs) using an aspheric lens. The collection lens is chosen such that the f-number matches the NA of the multi-mode fiber. Multi-mode fiber has a larger core diameter than single mode fiber that improves the collection efficiency. But it increases sensor noise in the form of fiber mode noise caused by fiber motion [100]. To reduce the fiber mode-noise both the single-mode pitch-fiber and the multi-mode catch-fiber were fixed to minimize fiber motion during the experiment.

The multiplexed light is collimated using an aspheric lens with focus length of 25 mm (Edmund Optics,) and then wavelength demultiplexed by a diffraction grating with 1200 grooves/mm (Edmund Optics) from which the individual wavelengths diffract at different angles in a first-order Littrow configuration (Fig. 27). The transmitted laser signals obtained by the four large-area (diameter: 2 mm) InGaAs photodiode detectors (Thorlabs, PDA10CS) are simultaneously recorded and averaged 1000 samples at a rate of 20 kHz

implying an effective time for data acquisition of 50 ms. The large area detectors are necessary to ensure that the entire beam is focused on the active area of the detector. Control of the experiment and further data processing was performed in a LabVIEW environment running a National Instruments data acquisition (NI-DAQ) system. The NI-DAQ system consisted of a computer equipped with a PCI-6115 DAQ board (12-bit A/D conversion) and a BNC-2110 analog I/O block.

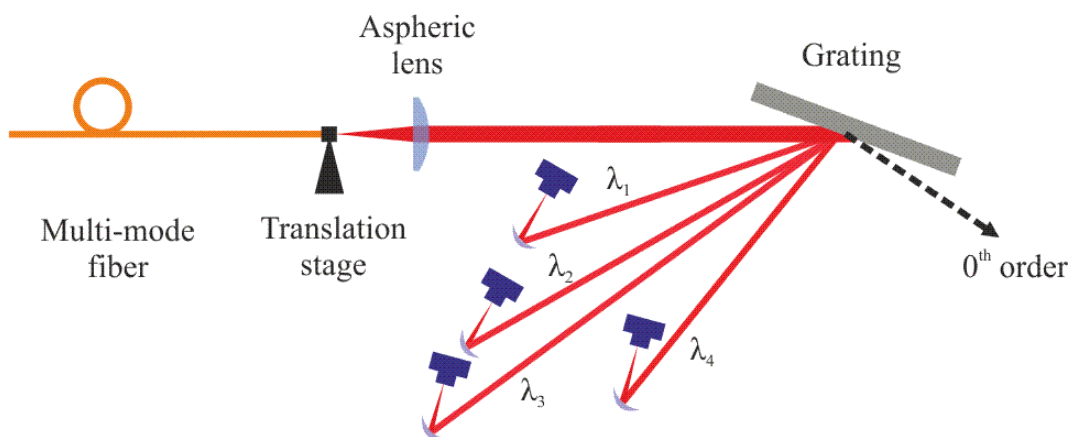


Fig. 27: Four wavelength demultiplexing setup used for transmission measurements.

The optical cell (LOT) used in the measurement of liquid films has the following features:

1. The thickness of the liquid layer within the cell is adjusted by PTFE spacers.
2. The cell is fitted with a Luer-lock syringe and a capillary to supply the appropriate liquid from a pipette.
3. A thermocouple is inserted through a small hole in the upper plate to monitor the temperature of the liquid sample.
4. The cell is mounted in a metal heating jacket through which water from a thermostat is circulated.
5. The upper quartz could be removed and this cell would be applied for a time-resolved measurement of an evaporating free liquid film deposited on the lower quartz plate. This will be discussed in section 4.6 in detail.

Furthermore, the exact optical path length between the inner window surfaces was determined by forming an average of the fringe spacing due to multiple reflections between the inner window surfaces of the empty cell placed in the beam path of the FTIR instrument while scanning a spectrum using the relation [101]

$$d = \frac{1}{2n_{\text{air}}\Delta f}, \quad (35)$$

where Δf is the mean wavenumber separation between interference maxima, and n_{air} the refractive index of air. When the cell temperature was varied the fractional change in the path length is approximately $0.3 \mu\text{m/K}$ due to the thermal expansion of the spacer material and therefore can be neglected within the small temperature range investigated here.

4.5 Demonstration of liquid-film measurements

In order to validate the performance of the sensor, a series of experiments were performed first on a liquid sample cell (shown in Fig. 26) with known liquid film thickness. In the following section two limiting cases of the thin film measurements for NaCl and urea solutions will be considered: (1) those with variable solute concentration at constant temperature and (2) those with variable temperature at constant solute concentration.

4.5.1 Measurement of liquid-film parameters of aqueous of NaCl solutions

The sample cell provided thin liquid films of precisely known thickness using four spacers (0.2, 0.5, 1.0, and 1.5 mm) and with temperature between 293 and 318 K. A variety of aqueous NaCl solutions were used with concentrations between 5 and 15 wt%. The path lengths (i.e., layer thickness) were evaluated from the transmittance ratios as outlined in section 4.1 under the assumption that either the temperature or concentration of the liquid was known.

For a fixed temperature ($T_L = 298 \text{ K}$) the layer thickness and NaCl mass fraction were calculated from measured transmittance ratios (cf., Eq. (29)) at wavelengths 2, 3, and 4, marked in Fig. 15b.

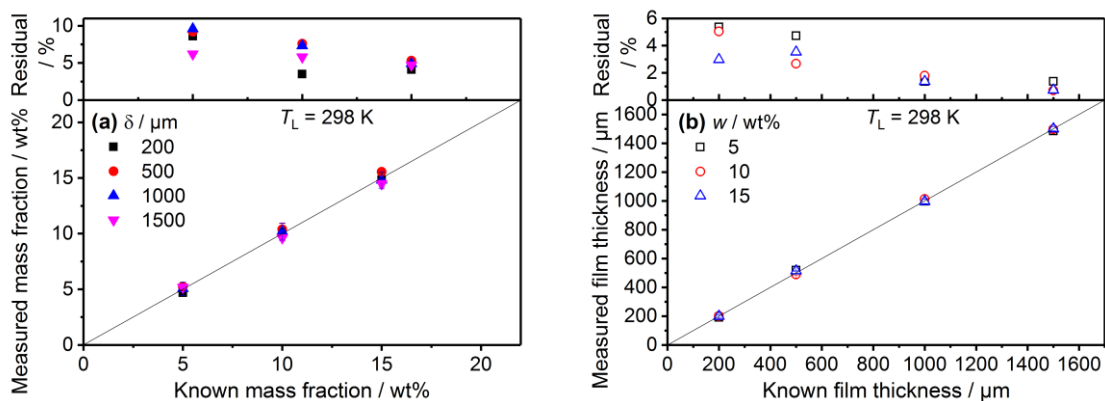


Fig. 28: a) Measured NaCl mass fraction (filled symbols) as a function of given mass fraction with layer thickness as parameter. b) Measured film thickness (open symbols) as a function of the plate distance for given NaCl concentrations of 5–15 wt% at 298 K.

Comparisons between the measurement and the given layer thickness are displayed in Fig. 28 and summarized in Table 10. The solid straight lines in the respective graphs represent the one-to-one correspondence between both values and the error bars indicates one standard deviation of the data collected in two repeated measurements on two days.

Table 10: Standard deviations and relative uncertainty between measurement and given NaCl mass fraction and layer thickness (i.e., plate separation) at a temperature of 298 K.

$w(\text{NaCl})$ / wt%	Standard deviation σ_{max} in w_{meas} / wt%	$\frac{ w_{\text{meas}} - w_{\text{known}} }{w_{\text{known}}}$ / %	Standard deviation σ_{max} in δ_{meas} / μm	$\frac{ \delta_{\text{meas}} - \delta_{\text{known}} }{\delta_{\text{known}}}$ / %
5	0.7	8.6	15.8	5.7
10	0.8	7.7	12.6	5.0
15	0.7	5.3	14.5	3.5

The largest standard deviation of 0.8% between the known and measured NaCl mass fraction occurs for the 10% sample at the sample thickness of 1000 μm . Although these data provide validation of the concept the available laser inventory did not provide the optimal sensitivity (Fig. 15b) and there were uncertainties in the NaCl concentration determined as large as a relative uncertainty of 10%. The measured film thickness (Fig. 28b) is in good agreement with the known plate separation. Due to the estimated error in the calculated NaCl concentration, the largest uncertainty in film thickness was 6%.

Alternatively, if the NaCl concentration can assumed as known and fixed and the liquid temperature and sample thickness were calculated from the measured transmittance ratios

(Eq. (32)) at wavelengths 1, 2, and 4 (marked in Fig. 16b). The comparison for three salt concentrations is shown in Fig. 29a–c and summarized in Table 11.

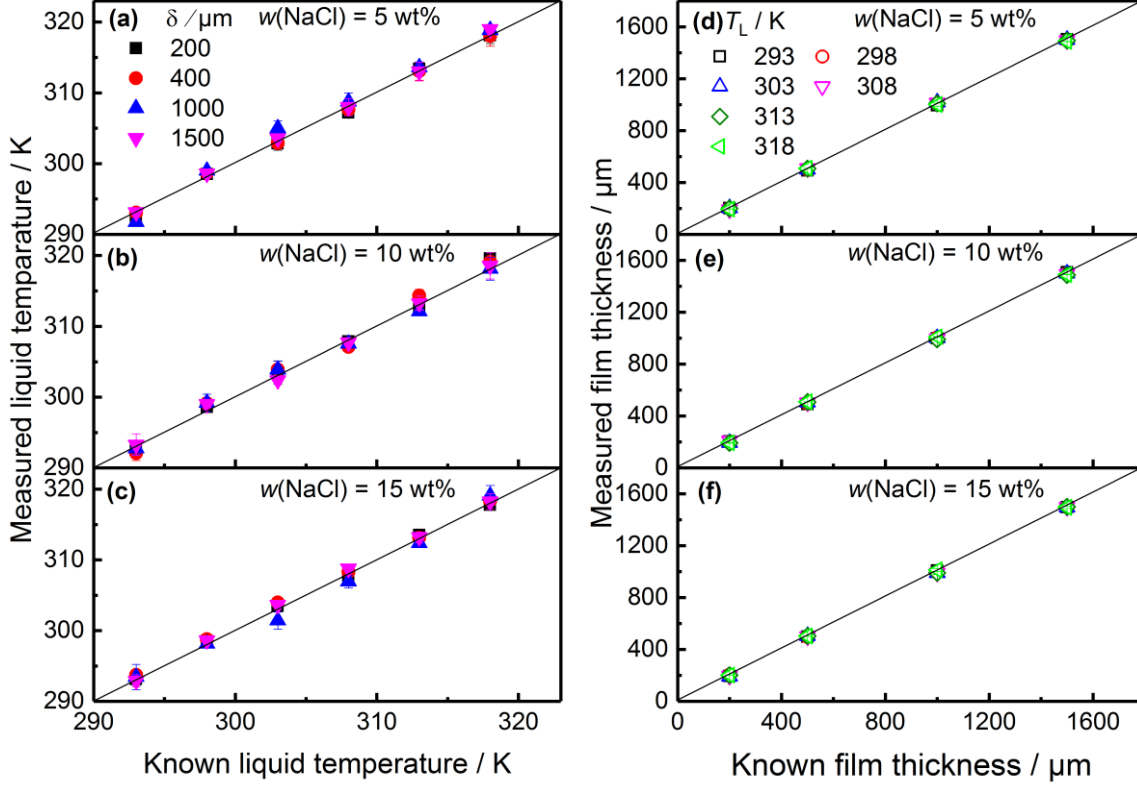


Fig. 29: (a–c): Correlation between the temperatures derived from absorption measurements (filled symbols) and the thermocouple readings for different layer thickness. (d–f): Correlation between the film thickness measured by absorption (open symbols) and the one given by the respective spacer at different solute concentration.

Table 11: Standard deviations and relative uncertainty between the measurement and the given liquid temperature and layer thickness

$w(\text{NaCl})$ / wt%	Standard deviation σ_{\max} in $T_{L,\text{meas}}$ / K	$\left \frac{T_{L,\text{meas}} - T_{L,\text{known}}}{T_{L,\text{known}}} \right _{\max}$ / %	Standard deviation σ_{\max} in δ_{meas} / μm	$\left \frac{\delta_{\text{meas}} - \delta_{\text{known}}}{\delta_{\text{known}}} \right _{\max}$ / %
5	1.5	0.5	12.5	3.5
10	1.6	0.7	14.8	4.8
15	1.8	0.6	11.9	4.7

The temperature uncertainty of the thermocouple (TC Direct, type K) is 0.4% (1.2 K at 300 K), and the difference in temperature between the laser absorption and the thermocou-

ple value was of order 2 K. Part of this difference might be related to the positioning of the thermocouple in the sample holder block. In the laser absorption temperature measurement, the uncertainty of the integrated transmittance ratio $R(T)$ is determined by the uncertainty of measured absorption coefficient (Eq. (26)) and can be written

$$\Delta R(T) = R(T) \sqrt{\sigma_{k1}^2 + \sigma_{k2}^2 + \sigma_{k4}^2}, \quad (36)$$

and therefore the uncertainty of the laser sensor in retrieving a temperature can be estimated by

$$\Delta T_L \approx \frac{R(T)}{dR(T)/dT} \sqrt{\sigma_{k1}^2 + \sigma_{k2}^2 + \sigma_{k4}^2}. \quad (37)$$

If the transmittance can be perfectly measured temperature uncertainty is about 4 K. For these validation measurements the largest difference in the measured liquid temperature was 1.8%. The measured film thicknesses (open symbols in Fig. 29d–f) were in good agreement with the known path lengths. Repeating the experiments on two days the largest standard deviation for the measurement of liquid film thickness was 15 μm or a maximum relative error of 4.8%.

4.5.2 Measurement in the liquid film of urea solution

Urea solutions were prepared similarly as detailed above to validate the sensor's performance for films of known thickness (0.2, 0.5, 1.0, and 1.5 mm), temperature (298–318 K), and solute concentration (5–15 wt%). For a fixed temperature ($T_L = 298$ K), the layer thickness and urea mass fraction were inferred from the measured transmittance ratios using Eq. (29) and Eq. (30). Fig. 30 illustrated the resulting accuracy of determining the urea mass fraction (left) and layer thickness (right) which is also summarized in Table 12.

The solid straight lines in the respective graphs represent the one-to-one correspondence between both values and the error bars represent one standard deviation of the data measured in two repeated measurements on separate days. The largest error of measured urea mass fractions was 1.8 wt% (for the 30 wt% sample at a sample thickness of 1000 μm). The maximum relative uncertainty in the concentration measurements was 7% (cf., residuals in the upper part of each graph). The measured film thicknesses (Fig. 30b) were in good agreement with the known plate separation leading to a corresponding largest uncertainty of 5%.

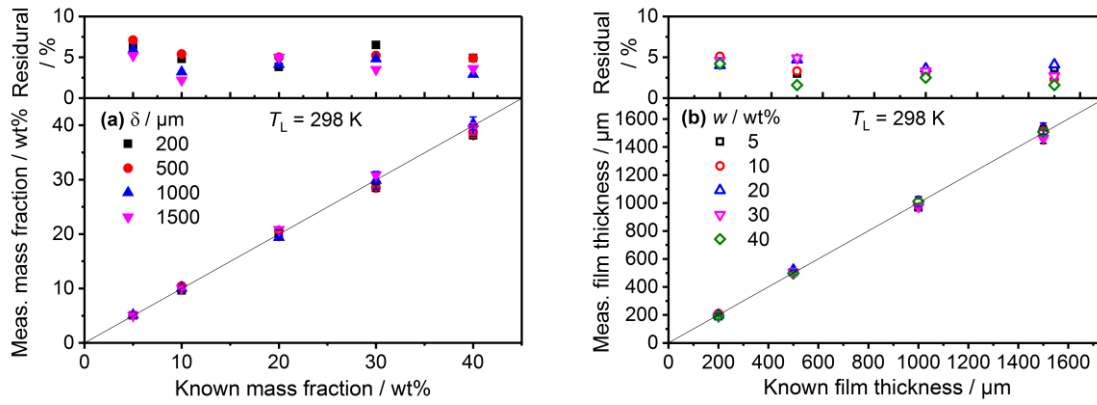


Fig. 30: (a) Correlation between measured and given urea mass fraction with layer thickness as parameter. (b) Measured film thickness as a function of the plate separation for given urea concentrations between 5 and 40 wt% at 298 K. The upper panel in each graph indicates the respective residuals between measured and given parameter values.

Table 12: Standard deviations and relative uncertainties between measurement and given urea mass fraction and layer thickness (i.e., plate separation) at a temperature of 298 K.

$w(\text{urea})$ / wt%	Standard deviation σ_{\max} in $w_{\text{meas}} / \text{wt}\%$	$\frac{w_{\text{meas}} - w_{\text{known}}}{w_{\text{known}}}$ / % $_{\max}$	Standard deviation σ_{\max} in $\delta_{\text{meas}} / \mu\text{m}$	$\frac{\delta_{\text{meas}} - \delta_{\text{known}}}{\delta_{\text{known}}}$ / % $_{\max}$
5	0.4	7.0	64.6	4.9
10	0.4	5.4	40.1	4.5
20	0.9	5.4	40.8	4.4
30	1.8	6.5	28.2	4.7
40	1.2	4.9	24.1	3.5

Similarly, if the urea concentration was known, the liquid temperature and sample thickness were calculated simultaneously from the measured transmittance ratios (Eq. (29) and (30)) at wavelengths 1, 2, and 4 (marked in Fig. 17b). In Fig. 31a–b calculated temperatures for two urea mass fractions (5 and 40 wt%) are plotted versus temperatures measured by the thermocouple. The comparison for all five urea concentrations is summarized in Table 13. For all tests, the temperature uncertainty of the thermocouple is 0.4%.

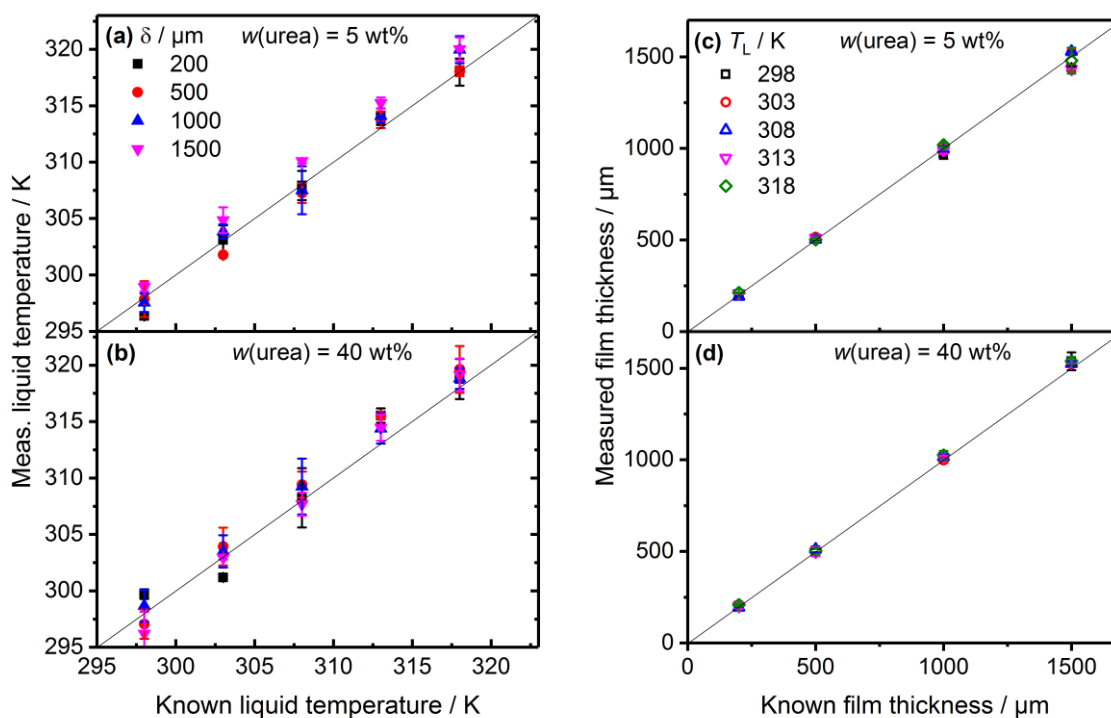


Fig. 31: (a–b) Correlation between temperatures derived from absorption measurements and thermocouple readings for different layer thickness and two urea concentrations. (c–d): Correlation between film thickness measured by absorption and the one given by the respective spacer at different temperatures and two solute concentrations.

Table 13: Standard deviations and relative uncertainty between the measurement and the given liquid temperature and layer thickness.

T_L / K	Standard deviation σ_{\max} in $T_{L,\text{meas}}$ / K	$\left \frac{T_{L,\text{meas}} - T_{L,\text{known}}}{T_{L,\text{known}}} \right _{\max}$ / %	Standard deviation σ_{\max} in δ_{meas} / μm	$\left \frac{\delta_{\text{meas}} - \delta_{\text{known}}}{\delta_{\text{known}}} \right _{\max}$ / %
298	2.1	0.9	60.0	6.7
303	2.8	1.0	36.8	6.1
308	1.6	1.2	41.9	6.1
313	2.6	0.8	35.6	5.9
318	2.6	0.8	48.8	6.2

Furthermore, for 80% of the experiments, the difference in temperature derived from the laser absorption and measured from the thermocouple was up to 3 K partly due to the posi-

tioning of the thermocouple in the sample holder block. In the laser absorption temperature measurement, the uncertainty of the integrated transmittance ratio $R(T)$ is determined from the uncertainty of measured absorption coefficients. If the transmittance could be perfectly measured, the temperature uncertainty would be about 4 K. The largest deviation of the evaluated temperatures from temperatures measured by the thermocouple was 2.8 K. The measured film thicknesses (Fig. 31c–d) were in good agreement with the known path lengths. It is noteworthy that the largest standard deviation for two independent measurements of film thickness was 60 μm (error bars in Fig. 31), or a maximum relative error of 6.7%.

4.6 Time-resolved measurements of film properties

Further experiments were performed for time-resolved simultaneous measurements of liquid film thickness, liquid-phase temperature, and non-specific background of an evaporating free aqueous film deposited on a quartz plate. The whole setup is similar to the one described before for the calibration measurement, but with three lasers in this system in order to measure the solute concentration and film thickness at a fixed temperature. A film of aqueous NaCl or urea solution (5 wt%) was prepared by dripping and stirring small droplets using a glass pipette onto the lower quartz plate of the heatable cuvette and the upper quartz was removed (Fig. 32).

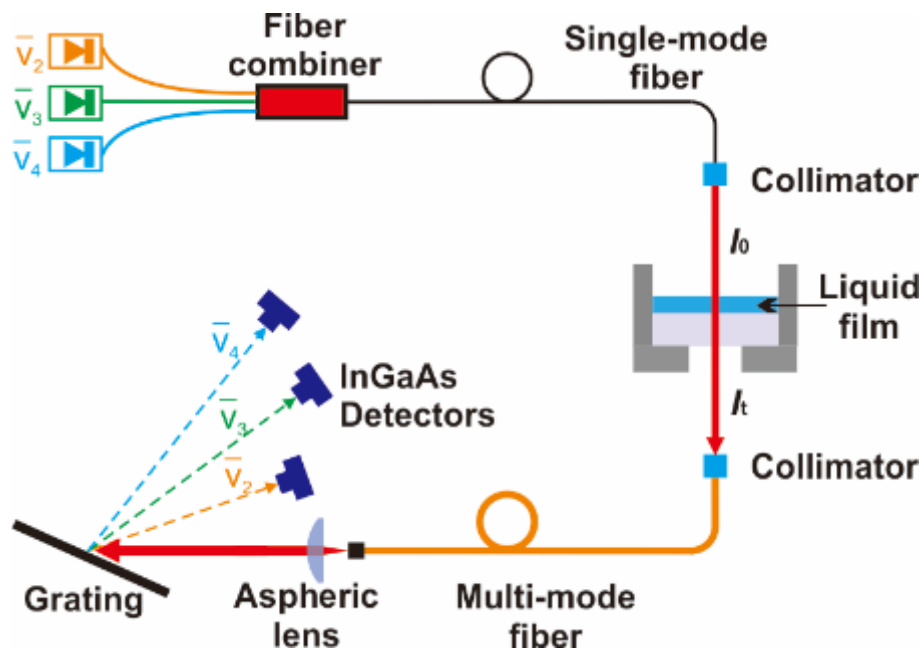


Fig. 32: Multiplexed diode-laser absorption sensor for liquid film measurements during evaporation.

NaCl solution

The liquid film was heated from room temperature up to a desired steady-state temperature by using the metal heating jacket of the cell. The layer thickness and the concentration were then measured via fixed-wavelength absorption with diode lasers 2, 3, and 4. Fig. 33 shows the film thickness (solid symbols) and the NaCl concentration (open symbols) for evaporating films at 318 (blue points) and 323 K (red points).

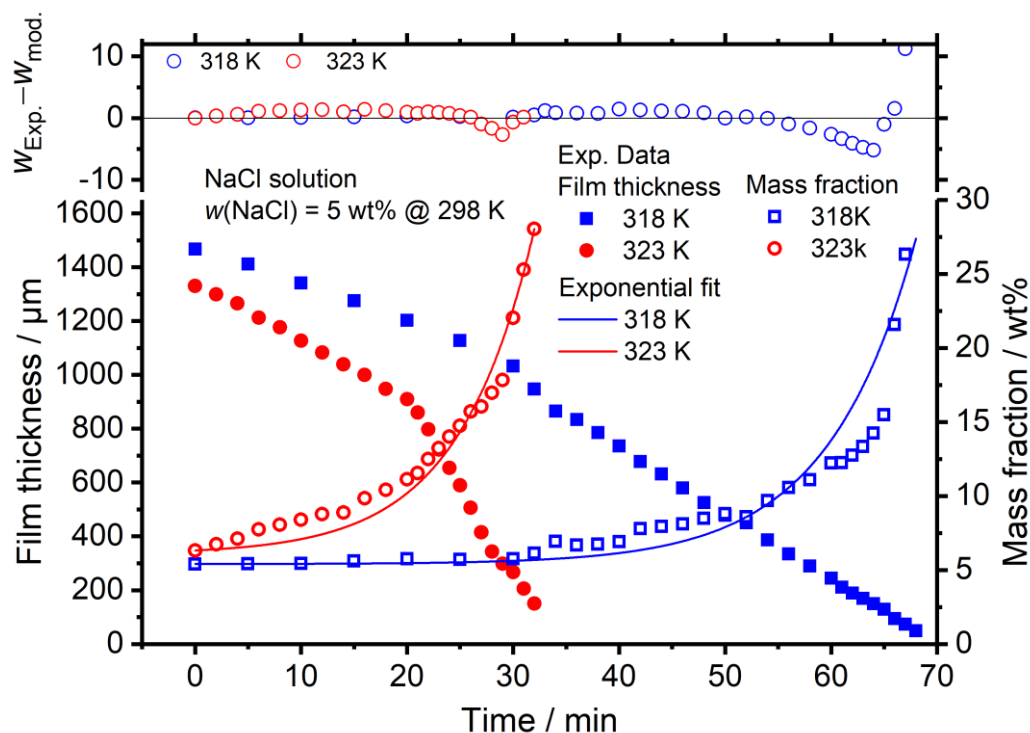


Fig. 33: Time-resolved measurement of film thickness (filled symbols) and concentration (open symbols) during film evaporation of NaCl solution at 318 K (blue squares) and 323 K (red circles) with exponential fit.

A constant evaporation rate produces a straight line on the film-thickness-versus-time plot. Note that at both temperatures a slower evaporation rate was observed until a film thickness of $\sim 900 \mu\text{m}$, which increased to a faster constant rate until the film completely evaporated (Table 14).

Table 14: Evaporation rate of NaCl solutions at different temperatures

Temperature / K	Evaporation rate / $\mu\text{m}/\text{min}$	
	> $\sim 900 \mu\text{m}$	< $\sim 900 \mu\text{m}$
318	20	37
323	21	61

During the evaporation, the change of the evaporation rate may be caused by several factors, namely, the vapor pressure above the film, interaction at the liquid-vapor interface, and the instability in water [102]. The inflection point in the evaporation rate near $900 \mu\text{m}$ corresponds to quite different NaCl concentrations. The time-dependent NaCl concentration was well described by a single exponential increase based on an empirical observation. The NaCl concentration-time histories at 318 (blue line) and 323 K (red line) are described by single exponentials as shown in Fig. 33 by the solid lines through the data points:

$$w(318 \text{ K}) = 6.07 + 0.25 \exp(0.14t), \quad (38)$$

$$w(323 \text{ K}) = 5.41 + 0.006 \exp(0.12t), \quad (39)$$

where t is the time.

Urea solution

The sensor was also demonstrated for simultaneous time-resolved measurement of layer thickness and urea concentration during film evaporation at constant temperature. Liquid layers of aqueous urea solution (5 wt%) were prepared on the lower quartz plate of the heatable cuvette while the upper quartz plate was removed. The liquid was distributed on the plate surface by spreading the deposited liquid through gentle mechanical stirring. To speed up the liquid film evaporation the liquid was brought to a desired steady-state temperature using the thermostatic metal heating jacket of the cell (see section 4.4). Layer thickness and urea concentration were then measured as a function of time via absorption of radiation from lasers 1, 2, and 4 (cf., Table 9). Fig. 34 shows the variations of film thickness (solid symbols) and urea mass fraction (open symbols) as a function of time for evaporating films at 318 (blue points) and 328 K (red points).

Fig. 34 shows that the two urea solutions with approximately the same initial solute mass fractions display the expected evaporation behavior with temperature. The film-thickness-

versus-time plots at both 318 and 328 K exhibit almost linear history. The thickness reduction rate at the two temperatures was calculated from the slope of fitted lines to the data points and was approximately 15, and 56 $\mu\text{m}/\text{min}$ for the two temperatures, respectively.

The hypothetical thermolysis of solid urea into gaseous NH_3 and HNCO takes place at about 403 K [103]. Therefore, it is expected that predominantly water evaporates initially from the film. After achieving the saturated state in the liquid, water evaporation and urea crystallization occur simultaneously under our evaporation condition.

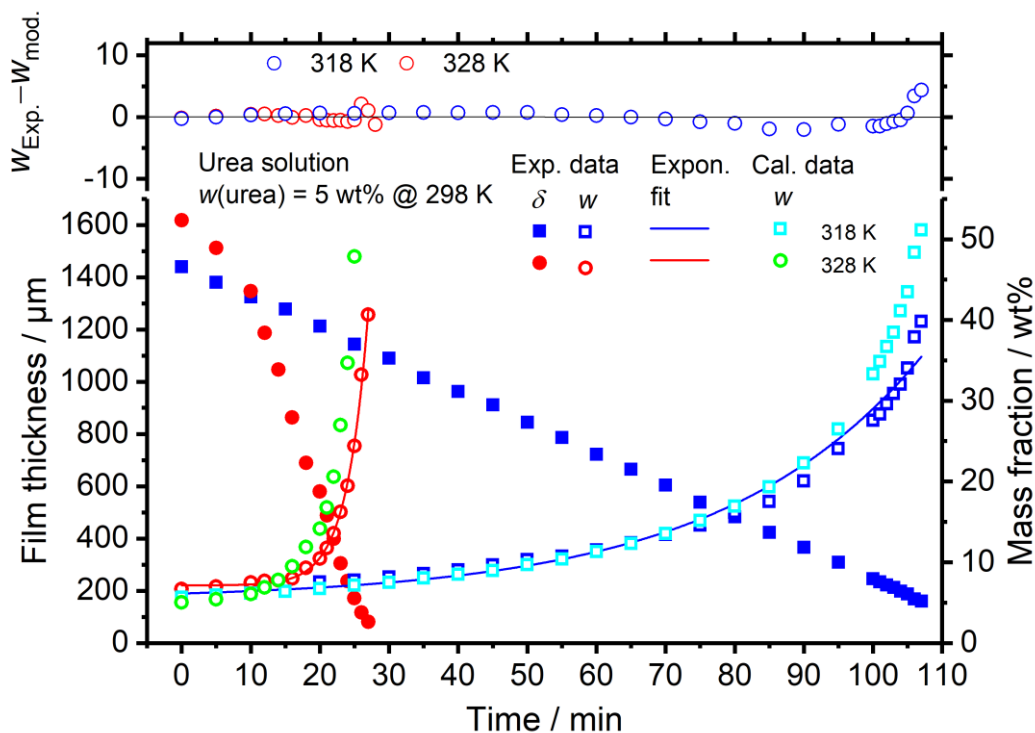


Fig. 34: Temporal variation of film thickness (filled symbols) and urea mass fraction (open symbols) during evaporation of films of aqueous urea solution at 318 K (blue squares) and 328 K (red circles) with exponential fit. Calculated mass fraction based on the measured film thickness at 318 K (open light blue squares) and 328 K (open green circles).

Note that the time-dependent urea concentrations at 318 (blue line) and 328 K (red line) are well described by a single exponential growth as shown in Fig. 34 by the solid lines through the data points:

$$w(318 \text{ K}) = 7.13 + 0.005 \exp(0.33 t), \quad (40)$$

$$w(328 \text{ K}) = 5.92 + 0.65 \exp(0.04 t). \quad (41)$$

Moreover, when the temperature is constant, the density of the urea solution (ρ) is related to the concentration (w) according to [104, 105],

$$\rho(w) = A_j + B_j w, \quad (42)$$

where A and B are fitting constants. Therefore, a urea concentration increase due to a decreased film thickness can be estimated as:

$$w = \frac{-A_j V + \sqrt{(A_j V)^2 + 4B_j V m_{\text{urea}}}}{2B_j V}. \quad (43)$$

In this equation, the volume V is given as the product δs , where s is the area of the deposited liquid on the window. In addition, m_{urea} is the mass of urea in the solution, which is immutable in the evaporating aqueous urea solution. In Fig. 34 the calculated urea concentrations at both 318 K (open light blue squares) and 328 K (open green circles) show good agreement with the measured concentrations until the film thickness reaches $\sim 600 \mu\text{m}$, above which the calculated concentration becomes higher than the measured one. This could be due to concentration gradients in the partially evaporated film and potentially precipitation of solid urea, which could cause the calculated volume of the liquid and even the urea concentration to deviate from the assumption of perfectly homogeneous evaporation and mixture composition (Eq. (43)). Even with this uncertainty, the data illustrate the potential use of laser absorption to monitor dynamic behavior of evaporating films of aqueous solutions.

4.7 Summary

In this chapter, a wavelength-multiplexed NIR diode laser absorption sensor has been investigated for measuring the layer thickness, solute concentration, and liquid temperature of aqueous NaCl and urea solutions. The temperature and solute concentration dependence of the NIR absorption of aqueous thin films from our FTIR measurements (chapter 3) provided the spectral database needed to design the multiplexed laser sensor.

Validation measurements of films of varying solute concentration at constant temperature and of varying temperature at constant solute concentration provide a proof-of-concept demonstration of the sensor. These tests were performed using a temperature-controlled cuvette with adjustable window separation. In the constant temperature limit, only three lasers are needed and the validation measurements found maximum difference between known and measured liquid film thickness and solute concentration of 6 and 10% (NaCl

solutions), and of 5 and 7% (urea solutions), respectively. Alternatively, when the concentration is known, the sensor validation measurements found a maximum difference for the liquid temperature of 2% (NaCl solutions), and 6.7% (urea solutions) and liquid film thickness of 5% (NaCl solutions), and of 1.2% (urea solutions), respectively.

To demonstrate the sensor potential to study the dynamics of evaporating liquid thin films, film thickness and solute concentration were determined during time-resolved measurements of evaporating aqueous NaCl and urea solution films ($w = 5$ wt%) on a transparent quartz plate at two steady-state temperatures. The method provides empirical data of millisecond time resolution, which could enable rapid measurement of the dynamics of evaporating liquid thin films, e.g., in the spray-based introduction of urea for ammonia production in SCR process for exhaust gas after treatment.

However, it should be noted that the present study provides measurement strategies for aqueous solutions where at least one of the two desired parameters (temperature or concentration) is known. In many practical systems, the liquid temperature and solute concentration are unknown, and a diagnostic that measures all three properties of the investigated liquid sample simultaneously would be preferred. The development of schemes for simultaneous monitoring of liquid film thickness, liquid temperature, and urea concentration, and demonstration measurements will be discussed in the next chapter.

5 Uncertainty quantification and design-of-experiment using Bayesian inference

The content of this chapter is derived from the own publication [106].

Diode laser-based multi-wavelength near-infrared (NIR) absorption in aqueous films is a promising diagnostic for making temporally-resolved measurements of layer thickness, temperature and concentration of a solute. Chapter 4 aimed at simultaneously determining two of these system parameters, while the third one (liquid temperature or solute concentration) needed to be specified. However, liquid temperature and solute concentration are unknown parameters and change independently over time. In this chapter an extension on measurements in aqueous urea solution films will be introduced, where simultaneous determination of multiple thin-film parameters (i.e., liquid temperature, solute concentration, and film thickness) from transmission measurements is presented coupled with the Bayesian methodology that is used to infer probability densities for the obtained data.

5.1 Introduction

In contrast with the method of absorbance ratios for the measurement of film parameters discussed in chapter 4, the actual measured transmissions are used to infer the actual values of the parameters by nonlinear regression within a model, which is a mathematically inverse problem. In general, the parameters are found by naïve minimizing of a sum-of-squares residual between measured and modeled data, which, under certain circumstances, produces the most probable set of parameters conditional on the observed data [107]. The principal limitation of the least-squares approach is that it only yields point estimates of the underlying parameter values, without providing a meaningful description of parameter uncertainty; this is particularly important for mathematically ill-posed inference problems, in which a large range of candidate parameter values can be substituted into the measurement equations to reproduce the data. In addition, the estimated parameter values are usually only local optima of the fitting metric, although methods that base model comparison on global optima do also exist [108].

Bayesian analysis overcomes these limitations by providing a rigorous method for using available experimental data with prior knowledge, to yield a more complete description of model and parameter uncertainties [109-112]. In addition, a database of temperature- and

concentration-dependent absorption coefficient for liquid water and aqueous urea solution was obtained using a FTIR spectrometer in the range between 5500 and 8000 cm^{-1} (chapter 3), and the absorption coefficient derived from there for the four laser wavelengths is referred to as a database model.

In this chapter, a Bayesian inference framework is presented for the determination of properties and uncertainty quantification of the thin film of urea-water solution. The Bayesian approach conceives the transmission measurements as random variables that obey probability densities, and the prior and measurement densities are propagated through Bayes' equation to obtain the posterior densities. Using this method, the sensor was first validated using a calibration cell presented in chapter 4. Uncertainty distributions in the measured parameters caused by measurement noise were modeled using a Markov-chain Monte-Carlo (MCMC) algorithm in the Bayesian framework. MCMC enables exploration of complex multi-dimensional probability distributions using an easily-sampled proposal distribution coupled with an accept-reject step [113]. Finally, as an application the temporal variation of film thickness, urea concentration, and liquid temperature were recorded during evaporation of a liquid film deposited on a transparent heated quartz flat.

5.2 Sensor strategy and Bayes' model

Bayesian inference provides a framework for combining experimental data with prior knowledge to physical model and quantify the associated uncertainties in parameter values [110]. There are several applications of Bayesian method in various areas of physics and we apply this method here in absorption spectroscopy. The following section briefly summarizes the theory on which the methodology is constructed and outlines the main steps of procedure.

5.2.1 Theoretical framework and algorithm

In the transmission measurement, $\tau(\tilde{\nu}_i)$ is contained in $\mathbf{b} \in R^m$ and unknowns (δ , T_L , w , and u) are contained in $\mathbf{x} \in R^n$, where $m = n = 4$. Generally, these vectors hold fixed values; however, in the Bayesian inference, \mathbf{b} and \mathbf{x} are considered random variables that feature probability densities, and the objective is to infer the probability density of \mathbf{x} by propagating the probability density determining \mathbf{b} through uncertainties affecting the measurement process. This is done through Bayes' equation:

The flow chart of Bayesian inference is shown in Fig. 35. In the present case, the observed transmission can be modeled as a function of the unknowns (δ , T_L , w , and u) from Eq. (27). In the transmission measurements the measurement noise contaminating \mathbf{b} is assumed normally distributed; then $\pi(\mathbf{b})$ is multivariate normal (MVN) and can be written as $\pi(\mathbf{b}) \sim N(\mu_b, \Gamma_b)$, where μ_b is the mean value, and Γ_b is the covariance matrix. If no prior information is assumed about \mathbf{x} (i.e., $\pi_{pr}(\mathbf{x}) = 1$), it can be shown that $\pi(\mathbf{x}|\mathbf{b}) \propto \pi(\mathbf{b}|\mathbf{x})$. To describe the distribution of \mathbf{b} given \mathbf{x} , a statistical model is required will be introduced in the next section.

5.2.2 Bayes' model

As stated before, in the laser absorption measurement of liquid films, the transmittance of the sample, $\tau(\tilde{\nu}_i)$, at frequency $\tilde{\nu}_i$ is given by Beer-Lambert's law (Eq. (27)). In the experiments presented here, we used four diode lasers used previously for the characterization of thin liquid film (see chapter 3), with their center wavelengths listed in Table 9 and marked in Fig. 17b.

A database of temperature- and urea concentration-dependent spectral absorption coefficient was created using a temperature stabilized quartz cuvette and a FTIR spectrometer (cf., chapter 3) in the range between 5500 and 8000 cm^{-1} . This database was used to generate 2nd order polynomial function to describe $k_{\tilde{\nu}_i}(T_L, w)$ for each of the four laser wavelengths

$$k_{\tilde{\nu}_i}(T_L, w) = a_{00}^i + a_{01}^i T_L + a_{10}^i w + a_{02}^i T_L^2 + a_{11}^i T_L w + a_{20}^i w^2, \quad i = 1, 2, 3, 4, \quad (45)$$

where a is the respective fitting coefficient at wavenumber $\tilde{\nu}_i$ (Table 15). The variation of the absorption coefficient of urea solutions with temperature and urea concentration is depicted in Fig. 36 and provides the basis of the sensor strategy investigated here.

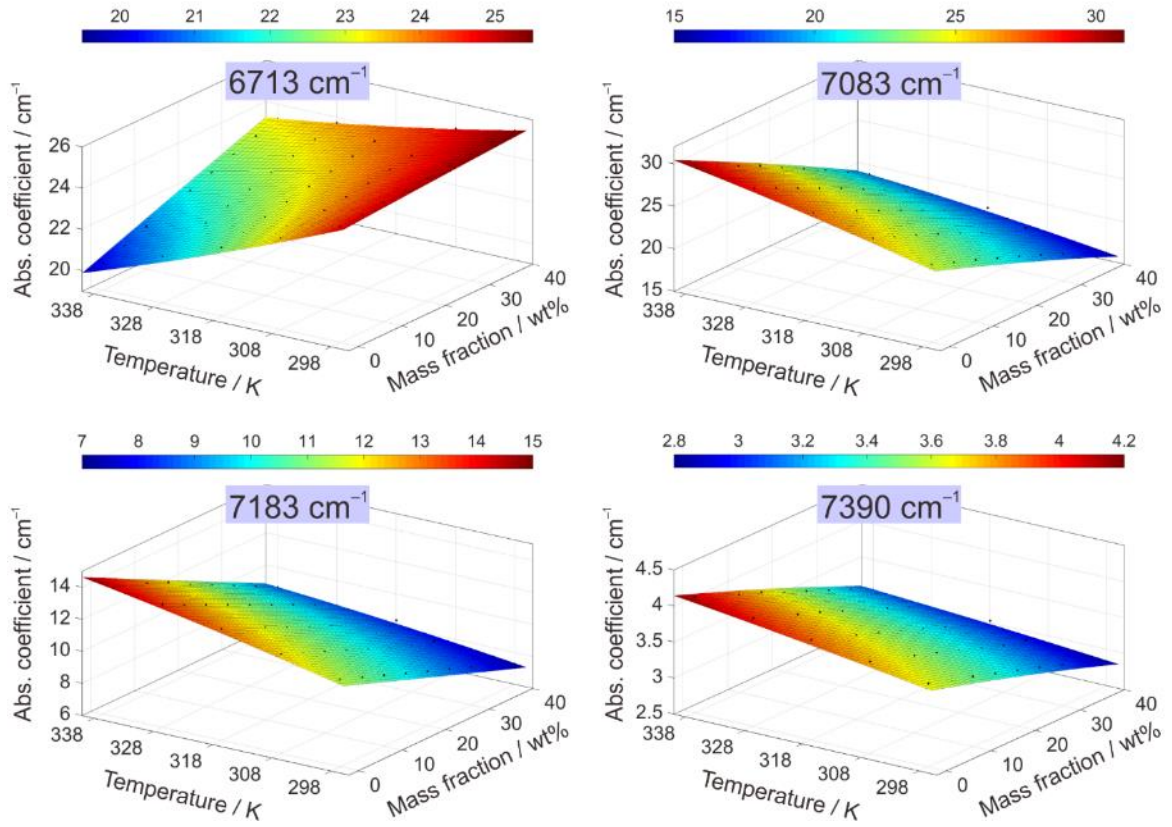


Fig. 36: Temperature- and concentration-dependent absorption coefficient of pure water and aqueous urea solutions (5–40 wt%) at different temperatures (298–338 K) for the four diode laser wavelengths employed in the current experiments. Black points: experiment; colored surfaces: polynomial fit (for the fitting coefficients, see Table 15).

Table 15: Center wavenumber of the diode lasers utilized in the present experiments and polynomial fitting coefficients for respective absorption coefficients as a function of temperature and solute concentration (cf., Eq. (45)).

Laser # <i>i</i>	$\tilde{\nu}_i$ / cm^{-1}	Fitting coefficient					
		a_{00}^i	a_{01}^i	a_{10}^i	a_{02}^i	a_{11}^i	a_{20}^i
1	6713	86.78	-0.30	-0.42	2.97×10^{-4}	1.50×10^{-3}	-1.62×10^{-5}
2	7083	-57.16	0.39	0.27	-4.00×10^{-4}	-1.60×10^{-3}	-5.91×10^{-4}
3	7183	-29.93	0.20	0.14	-2.04×10^{-4}	-8.20×10^{-4}	-7.65×10^{-6}
4	7390	43.62	-0.27	-0.04	4.59×10^{-4}	-2.02×10^{-4}	-5.21×10^{-5}

The choice of a bi-quadratic function to interpolate the FTIR measurements reflects a balance between sufficient degree-of-freedom to capture the trends of the absorption coefficient with temperature and solute concentration, but not so many as to “over-tune”, i.e., capture non-physical variations caused by measurement error. Accordingly, assessing the uncertainty associated with this interpolating function is not straightforward. Therefore, this error will be treated heuristically by folding it into the likelihood function as described later in this chapter.

The multi-wavelength sensor design strategy for absorption measurements of films of liquid solutions is similar to the sensor design introduced in chapter 4. Four DFB diode lasers were multiplexed into a single-mode fiber by a fiber combiner, and the light was collimated and transmitted through a liquid film. Films with controlled thickness were formed by filling the space between two optically-polished quartz windows of a cuvette (cf., Fig. 26) mounted in a stainless steel cell holder, and its thickness can be varied with a set of PTFE spacers. Alternatively, the front window can be removed to measure film open to the atmosphere. The transmitted light was collected into a multi-mode fiber and wavelength-demultiplexed by a diffraction grating; each separated wavelength beam was then focused onto four appropriately positioned InGaAs detectors. The cell was mounted in a metal heating jacket through which water from a thermostat was circulated. A thermocouple was inserted into the cell for monitoring the temperature of the liquid sample.

5.3 Error modeling

As discussed in section 5.1, Bayes’s theorem can be expressed as $\pi(\mathbf{x}|\mathbf{b}) \propto \pi(\mathbf{b}|\mathbf{x})$ under the constraint conditions in the presented work. Furthermore, if the measurement noise is independent and modeled as a centered normal distribution, the likelihood can be written as

$$\pi(\mathbf{b}|\mathbf{x}) = \frac{1}{(2\pi)^{-m/2} |\Gamma_b|^{-1/2}} \exp\left\{-\frac{1}{2} [\mathbf{b}^{\text{exp}} - \mathbf{b}(\mathbf{x})]^T \Gamma_b^{-1} [\mathbf{b}^{\text{exp}} - \mathbf{b}(\mathbf{x})]\right\}, \quad (46)$$

where $|\Gamma_b|$ is the determinant of the measurement covariance matrix [114-116]. Since the measurements are independent, $\pi(\mathbf{b})$ integrates to unity (i.e., $\pi(\mathbf{b}) = 1$). To evaluate the likelihood, $\pi(\mathbf{b}|\mathbf{x})$, the covariance of measurement data Γ_b is required, due to the measurement noise and uncertainty in the calibration procedure. The noises in the output voltage consist of process noise caused by fluctuations in laser intensities and electronic noise, which are assumed to be normally distributed (Fig. 37). The measurement noise variance is reduced through time averaging, and it can be shown that:

$$\Gamma_b \approx N_s^{-1/2} \text{diag}(\sigma_{b,1}^2, \sigma_{b,2}^2, \dots, \sigma_{b,m}^2), \quad (47)$$

where N_s is the number of samples.

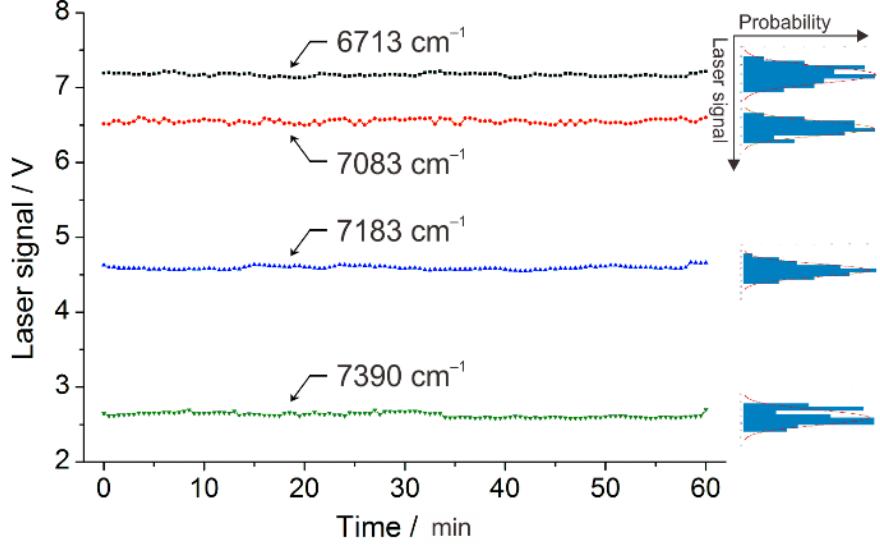


Fig. 37: Measured signal intensities and noise standard deviation (illustrated as expanded version at the right figure margin) obtained from analyzing the output voltage of the four diode lasers during a 1-hour time span. The noise consists of process noise caused by fluctuations in laser output and electronic noise.

Since the measurement model is imperfect, it includes some unknown uncertainties that we treat as random, e.g., systematic issues with the FTIR measurement and the interpolation error from the coarse parameter variation when taking FTIR data. In absence of exact information, the perturbation in the data is assumed to be white (or uncorrelated) and prescribe a standard deviation of 1% of the measurement at a given estimate to mask the overall error.

The most probable set of \mathbf{x} , i.e., the quantities that maximize the posterior probabilities $\pi(\mathbf{x}|\mathbf{b})$, is found by maximizing $\pi(\mathbf{b}|\mathbf{x})$. The maximum likelihood estimate \mathbf{x}^{MLE} , is equivalent to weighed least-squares minimization,

$$\arg \max [\pi(\mathbf{x}|\mathbf{b})] = \arg \max [\pi(\mathbf{b}|\mathbf{x})] = \mathbf{x}^{\text{MLE}} = \arg \min \left\{ \sum_{j=1}^m \frac{[\mathbf{b}_j^{\text{exp}} - \mathbf{b}_j(\mathbf{x})]^2}{\sigma_{b,j}^2} \right\}. \quad (48)$$

In this case, the maximum a posterior (MAP) and maximum likelihood (MLE) estimates coincide, i.e., $\mathbf{x}^{\text{MAP}} = \mathbf{x}^{\text{MLE}}$. An advantage of Bayesian inference over least-squares minimi-

zation is that one can also estimate the uncertainty from the posterior density via Eq.(44). The marginalized probabilities can be reported by “integrating out” all the other variables, e.g.,

$$\pi(x_1|\mathbf{b}) = \int_{-\infty}^{\infty} \int_{-\infty}^{\infty} \cdots \int_{-\infty}^{\infty} \pi(\mathbf{x}|\mathbf{b}) dx_2 dx_3 \cdots dx_n . \quad (49)$$

The uncertainty associated with each variable is reflected by the width of the corresponding marginalized posterior probability, which can be summarized by a credibility interval that contains a specified probability. Here, a 90% equal-tailed interval is used, where the probability densities at the lower and higher interval limits both 5% [117].

As shown in Eq. (44), the evidence, $\pi(\mathbf{b})$, is needed to normalize the posterior probability that is essential for calculating uncertainty estimates through credibility intervals. Since \mathbf{x} is four dimensional, to compute such integral Bayesian analyses it is typically carried out using MCMC, which generate a sequence of random samples starting from an initial point. At each set of parameters \mathbf{x}^k , a candidate point $\mathbf{x}^{k+1,c}$ is generated, often by sampling a normal distribution centered on the current point. The candidate point is accepted or rejected based on the relative posterior probabilities, $\pi(\mathbf{x}^{k+1,c}|\mathbf{b})$ and $\pi(\mathbf{x}^k|\mathbf{b})$, using the Metropolis-Hastings criterion [112, 116]. After an initial burn-in period, the samples become ergodic with the target distribution, $\pi(\mathbf{x}|\mathbf{b})$. Finally, marginalized probabilities can be estimated from a counting procedure (e.g., histograms).

5.4 Results and discussion

5.4.1 Validation experiments

To validate the sensor’s performance a sample of aqueous urea solution ($w = 10$ wt%) was prepared in the sample cell with a known thickness of 1 mm. The exact optical path length of 942 μm was determined by forming an average of the fringe spacing due to multiple reflections between the inner window surfaces of the empty cell placed in the beam path of the FTIR spectrometer (chapter 4). The liquid film was heated from room temperature up to a steady-state temperature of 308 K by raising the water temperature circulating inside the metal heating jacket of the cell. Since the thermocouple was positioned in the sample holder block the measurements were started roughly one minute after setting the temperature value such that the liquid film attained the same temperature as the holder block.

To visualize Bayesian inference and the marginalization of posterior densities, a set of 2 million samples, $X = \{x_1, x_2, \dots, x_n\}$, is generated using a MCMC algorithm [118]; these samples are then used to form marginalized posterior distributions for film thickness, liquid temperature, and solute concentration through kernel density estimation [119]. Fig. 38 shows the marginalized likelihood and posterior probability densities for T_L , w , and δ inferred from the transmission data.

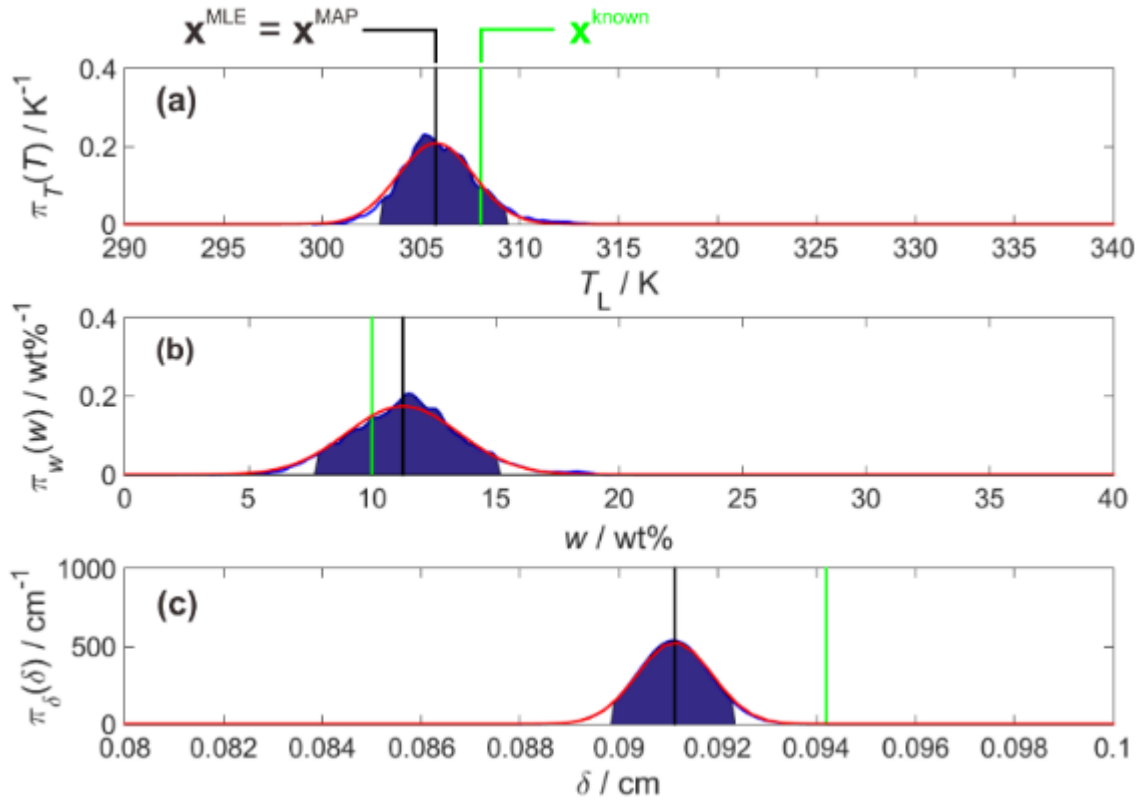


Fig. 38: Marginalized likelihood (blue) and posterior (red) densities for (a): T_L , (b): w , and (c): δ inferred from the transmission data. In all cases the MLE are equal to MAP (vertical black line). The vertical green line corresponds to the respective known quantity. 90% credibility intervals for these distributions (blue) are summarized in Table 16.

Table 16: 90% credibility intervals for the likelihood shown in Fig. 38, which surround \mathbf{x}^{MLE} .

	Test conditions	\mathbf{x}^{MLE}	90% credible interval
T_L / K	308	305.8	[302.9, 309.2]
$w / \text{wt}\%$	10	11.2	[7.7, 15.2]
$\delta / \mu\text{m}$	942	912	[899, 924]

The vertical green lines represent the known test conditions. Uninformative priors are specified for the parameters (e.g., T_L , w , δ , and u), thus $\pi(\mathbf{x}|\mathbf{b}) = \pi(\mathbf{b}|\mathbf{x})$ and $\mathbf{x}^{\text{MLE}} = \mathbf{x}^{\text{MAP}}$. The \mathbf{x}^{MLE} (vertical black line) was found by Eq. (48) using a least squares Levenberg-Marquardt algorithm. The 90% credible intervals (blue area in) and \mathbf{x}^{MLE} are given in Table 16. Note that the known solution (vertical green line) for δ is outside the 90% credibility intervals. This could be due to uncertainty calculated through error propagation of the variation of determined liquid temperature and urea mass fraction based on the temperature- and concentration-dependent absorption coefficient k measured in the FTIR experiments, as well as uncertainty of the angle of incidence. Since the MCMC chains are often slow to converge it is often reasonable to approximate $\pi(\mathbf{x}|\mathbf{b})$ by its asymptotic normal form around \mathbf{x}^{MLE} . If the measurement noise is Gaussian, then

$$\mathbf{x} \sim \mathcal{N}(\mathbf{x}^{\text{MLE}}, \Gamma_{\mathbf{x}})^{-1}, \quad (50)$$

$$\Gamma_{\mathbf{x}} = \left[\mathbf{J}(\mathbf{x}^{\text{MLE}})^T \Gamma_b^{-1} \mathbf{J}(\mathbf{x}^{\text{MLE}}) \right] \quad (51)$$

where $\mathbf{J}(\mathbf{x}^{\text{MLE}}) \in \mathfrak{R}^{(m \times n)}$ is the Jacobian matrix with elements $J_{pq} = \partial b_p / \partial x_q$ [110] that can be found by differentiating Eq. (27) with respect to x_j . In this context, the marginalized distribution for the j th variable is simply a normal distribution with $\mu_j = x^{\text{MLE}j}$ and $\sigma_j = (\Gamma_{x,j})^{1/2}$ (red curve in Fig. 38).

5.4.2 Temporal variation of film evaporation

To demonstrate the time-resolved simultaneous measurement of film thickness, liquid temperature, and concentration a film of aqueous urea solution (5 wt%) was placed on the lower quartz plate of the cuvette (cf., Fig. 32) with the upper quartz plate removed. The liquid was spread out on the plate surface gentle mechanical stirring. To speed up the evaporation process, the liquid film was continuously heated up to a steady-state temperature (~ 320 K) by again using the metal heating jacket of the cell.

Fig. 39 shows the variations of film thickness (blue squares), liquid temperature (green triangles), and urea mass fraction (red circles) as a function of time. The error on δ corresponds to the sum of the uncertainty relative to the angle of incidence (2°), the uncertainty calculated through error propagation of the variation of determined liquid temperature and urea mass fraction based on the temperature (relative variation of 0.64%/K) and concentration (0.93%/wt%) dependence on the absorption coefficient k measured in the FTIR experiments (chapter 3), and the uncertainty quantified using Bayesian inference (Fig. 38). At

the start of the experiment, the liquid is at room temperature, and the temperature then increases during the first 3 minutes before plateauing around 320 K for the following 41 minutes. During this initial period the film thickness slightly decreases. Note that the density of the urea solution changes by 0.38%/K in the 298–320 K temperature range independent on the urea concentration [120]. This density variation is covered by the way the calibration data has been determined, and thus by the measurement model.

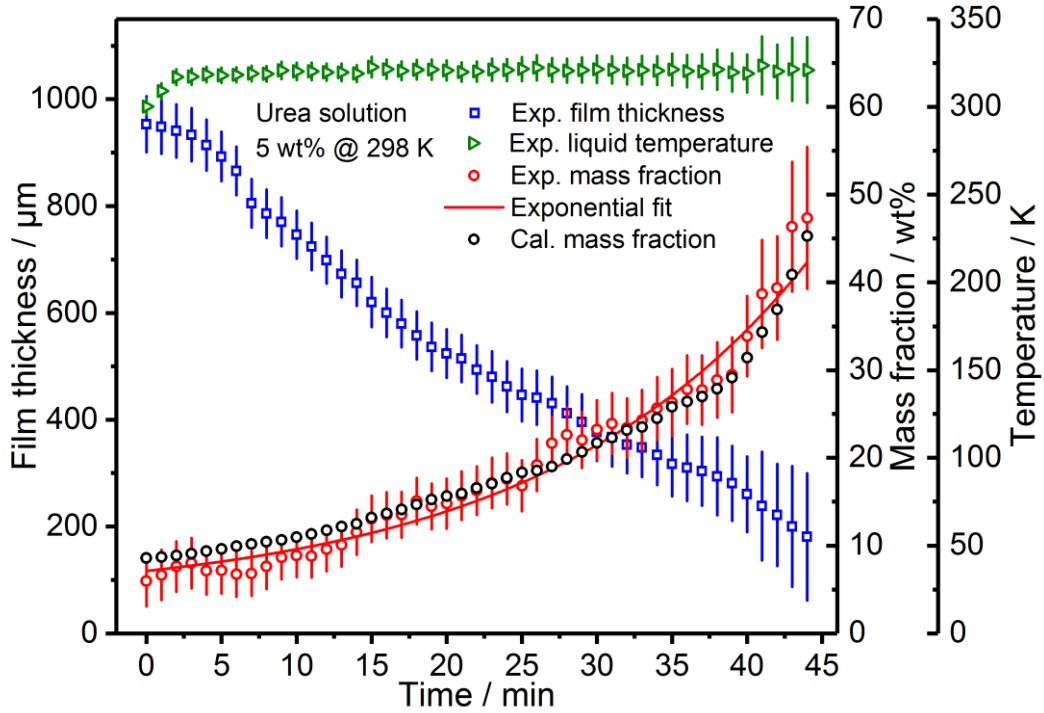


Fig. 39: Temporal variation of film thickness (blue squares), liquid temperature (green triangles), and urea mass fraction (red circles) during evaporation of an aqueous urea solution. The mass fraction data were fitted phenomenologically by an exponential function (red line) and calculated from a simple theory (black circles).

In the constant-temperature phase, the film thickness decreases steadily with time. The thickness reduction rate of urea solution film was calculated from the slope of a fitted line to the data points and was approximately 17 $\mu\text{m}/\text{min}$, which is similar to previous measurements of an evaporating aqueous urea solution film at 318 K (15 $\mu\text{m}/\text{min}$) (cf., chapter 4). Under the evaporation condition presented here, the urea concentration-time history can reasonably be described by a single exponential as shown in Fig. 39 by the red line through the data points:

$$w = 3.80 + 3.32 \exp(0.05t), \quad (52)$$

where t is the time. During the evaporation, the exponential change of the urea concentration may be caused by the vapor pressure at the prevailing temperature and the rate of diffusion of the vapor away from the surface. Furthermore, when the temperature is known, a urea concentration increase due to a decreased film thickness can be estimated with the algorithm used in chapter 4, and results of this calculation are depicted in Fig. 39 by black circles.

5.5 Summary

In this chapter, a Bayesian methodology that analyzes experimental data from four-color NIR transmission measurements in a thin liquid film of aqueous urea solution to simultaneously infer multi-parameters (film thickness, concentration, liquid temperature, and non-specific losses) as random variables defined by probability densities has been discussed.

The spectroscopic model was derived from FTIR measurements of the temperature and urea concentration dependence of the NIR absorption spectra of aqueous solutions. Validation tests were performed using a temperature-controlled cuvette with adjustable window spacing. To determine four parameters of interest simultaneously four laser wavelengths are needed. Maximum likelihood estimates of distribution parameters were found through Bayesian analysis. The MCMC algorithm was used to visualize Bayesian inference and the marginalization of posterior densities for the multi-parameters and 90% credibility intervals were computed. To study the steady evaporation behavior of a liquid thin film, film thickness, urea concentration, and liquid temperature were determined simultaneously during time-resolved measurements of a spread-out liquid layer on a transparent quartz plate for a stationary scenario.

6 Measurement of liquid films in retro-reflection

This chapter is derived from the own publication [121].

6.1 Motivation and overview

The measurement strategy of liquid film, as illustrated by the applications discussed in chapter 4 and 5, requires two-side optical access. In all of these measurements, laser light is transmitted through the sample in a single-pass line-of-sight fashion with a fiber (i.e., the transmitter) on one side of the film and a photodetector (i.e., receiver) on the other. In many practical applications, the liquid film is deposited onto opaque surfaces where optical access is only possible from one side and double-ended measurements are not feasible.

When light hits an opaque surface, there are three types of light reflection: specular reflection, diffuse reflection, and retro-reflection (Fig. 40). In specular reflection the incident and reflected light from a smooth surface of a mirror are at identical angles but on opposite sides. Light is not returned to the source. In diffuse reflection, light is scattered as it hits the surface and very little is returned to the source. In retro-reflection a large amount of the reflected light is returned directly to the original light source.

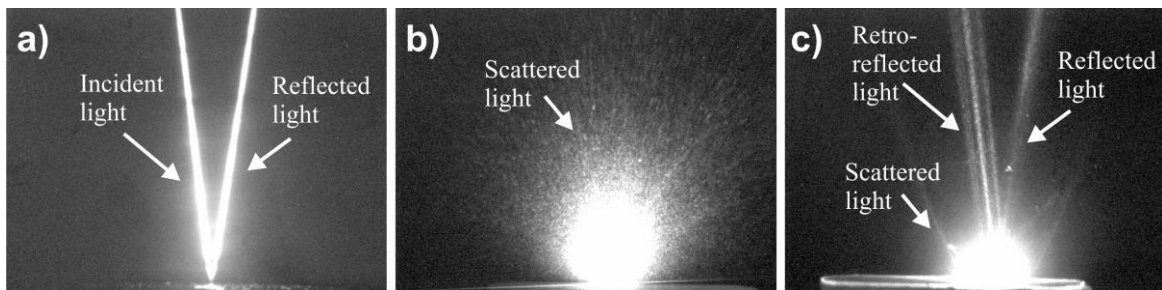


Fig. 40: Reflective images of a visible light beam (635 nm) on different surfaces: a) specular reflection on a mirror, b) diffuse reflection on a metal plate, c) retro-reflection on a retro-reflecting foil.

Several researchers have applied these different types of light reflection to infer gas-phase temperature or/and concentration. Gas-phase absorption measurements have been performed collecting light backscattered from a retro-reflector: Chen et al. [122] developed a VCSEL-based oxygen sensor for combustion optimization in gas furnaces collecting diffuse light from an anodized aluminum reflector. Seidel et al. [123] demonstrated a single-ended tunable diode laser absorption (TDLAS)-based open-path laser hygrometer for detection of water vapor with up to 2 m standoff distance. Wang and Sanders [124] utilized an off-axis diode laser sensor with wavelength-modulation spectroscopy (WMS) to meas-

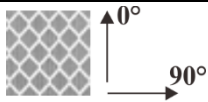
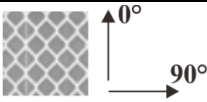
ure H₂O vapor spectra near 1350 nm with SNR > 400 using backscatter from rough surfaces and Goldenstein et al. [125] demonstrated a single-ended transmitter/receiver for stand-off measurements of gas temperature, pressure, and composition by collecting wavelength-modulated laser light backscattered from native surfaces.

In this thesis, this concept is extended to absorption-based measurements of liquid-water-film thickness collecting light scattered from retro-reflecting foils that support the liquid films. Retro-reflecting foils are readily available as they are routinely used to enhance the visibility of objects, such as traffic signs or safety clothing by enhancing the reflection in the visible and NIR [123, 126].

6.2 Characterization of retro-reflecting foils

As discussed in section 6.1, retro-reflection (RR) uses a surface as retro-reflector designed to direct light back towards the light source. Since the retro-reflection with a retro-reflecting foil is not perfect, the impinging light beam is partially absorbed and partially diffusely and specularly reflected (see Fig. 40). The distribution of this retro-reflected light depends on the type of retro-reflecting material (glass beads or prismatic elements). In order to select the suitable foil for the application various foils (Table 17) were characterized with regard to the reflective foil performance. Due to their cat-eye-like surface structure the foils reflect incoming radiation into the direction of the incoming beam for angled incidence of light. The angular dependence of the reflectivity of these foils therefore was determined beforehand.

Table 17: Retro-reflecting foils with different properties from 3M

Example of sheeting				
Name	Diamond grade	High intensity	Engineer grade	EG 3210
Technology	Microprismatic	Microprismatic	Glass bead	Glass bead

The optical setup for the characterization of retro-reflecting foils is depicted in Fig. 41. Light from a DFB diode laser emitting near 1.4 μm was directed through the central hole of an off-axis parabolic mirror (Thorlabs, reflected focal length (RFL) = 152.4 mm) onto the retro-reflecting foil. To eliminate unwanted linear beam translation during adjustment

of incident angle on retro-reflecting foil, the foil was pasted on a gimbal mount, and its distance from the parabolic mirror was adjusted to one RFL. The retro-reflected and/or specularly reflected light was collected by the same parabolic mirror, directed towards a second off-axis parabolic mirror and focused on a thermal power sensor (Thorlabs, S302C). Although infrared-sensitive cards are commercially available near $1.4 \mu\text{m}$, the laser beam is not easily observed due to the low power of the laser. The laser beam was co-aligned with a HeNe visible laser beam for alignment purposes. The incident light intensity I_0 and the reflected light intensity I_R were measured for rotation angles from 0° to 30° . The main purpose of the retro-reflecting foil is to spatially separate the (partial) specular reflection (SR) of the incoming beam by the liquid surface from the beam that carries the desired information from absorption by traversing the film twice. Due to the finite aperture of the the collection optics the direct reflection needs to be blocked from hitting the detector.

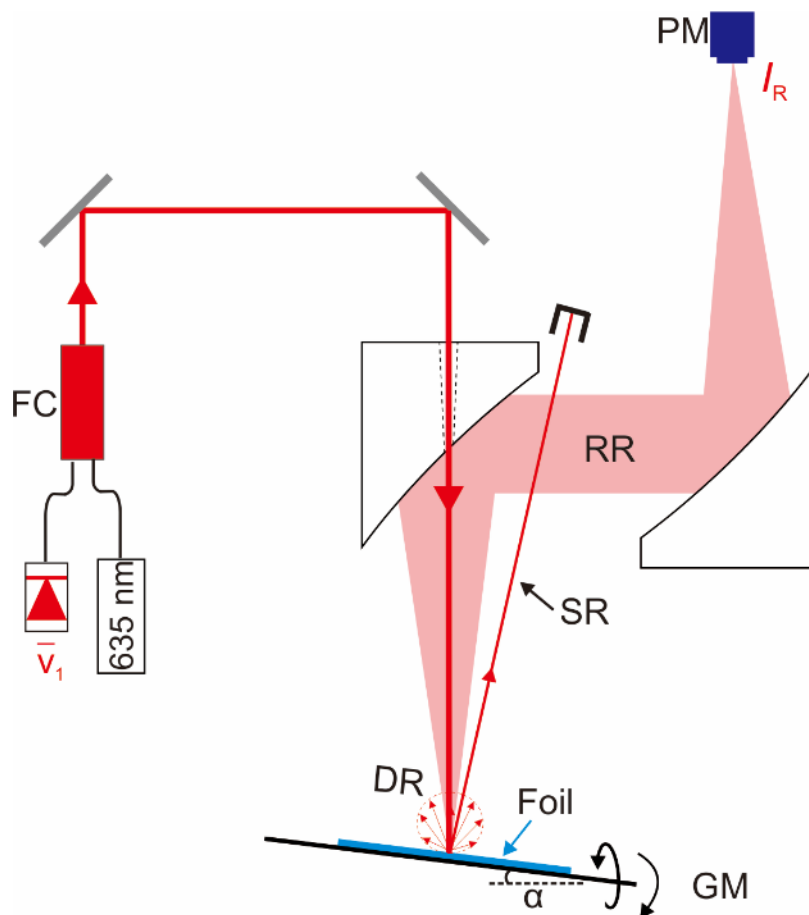


Fig. 41: Optical setup of the characterization of retro-reflecting foils. FC: fiber combiner, GM: Gimbal mount, RR: retro-reflection, SR: specular reflection, DR: Diffuse reflection, PM: Power meter.

The angular reflection properties of three commercial retro-reflecting foils (3M) are shown in Fig. 42. With the optical arrangement (Fig. 41), the measured reflectivity, $(I_R/I_0) \times 100\%$, decreased abruptly as soon as the angle changed from 5° to 6° , which is the limiting angle where the SR and RR beams were separated enough that the SR beam was no longer captured by the detector (Fig. 41). The Diamond Grade (DG) series foil with anti-fog coating that is equipped with a micro-prismatic array structure showed the highest reflectivity of 47% (at $\alpha = 7^\circ$) and was best suited for the present purpose, since the small contact angle (11°) of the “anti-fog” coating causes water to be more easily spread out into films and thus reduces the tendency of droplet formation during film evaporation (Fig. 43). All measurements presented in this chapter were carried out with this foil.

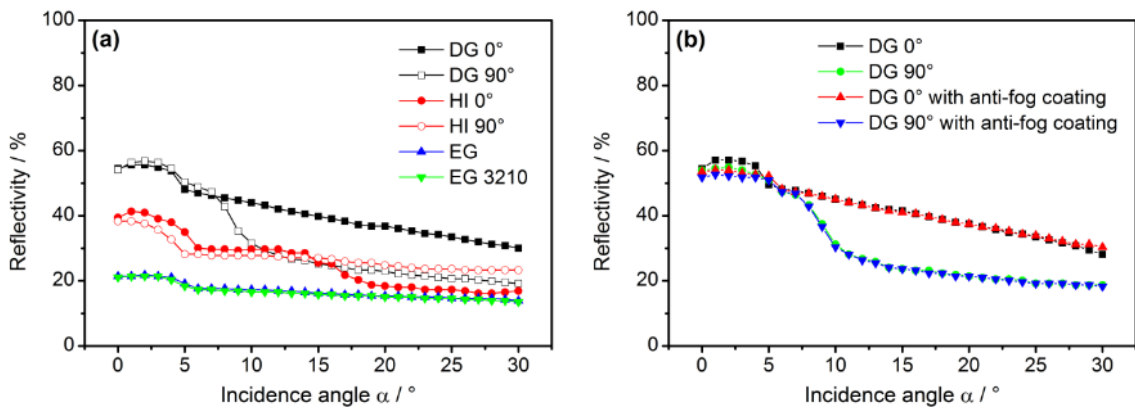


Fig. 42: Angular dependence of the relative intensity of retro-reflecting foils (Commercial materials from 3M): (a) Four standard foils (cf., Table 17); (b) Standard DG foil and foil with anti-fog coating.

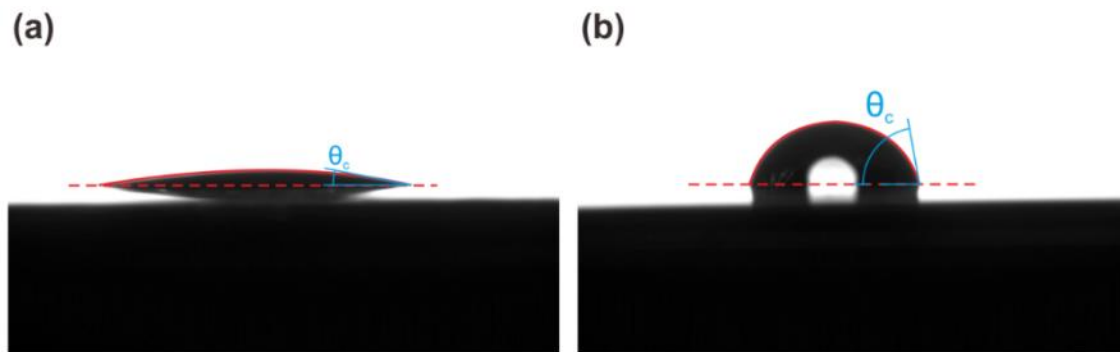


Fig. 43: Water ($V = 5 \mu\text{l}$) contact angle on (a) DG foil with anti-fog coating: 11° and (b) normal DG foil: 80° .

6.3 Measurement strategy and sensor design

The basic concept for two-color near-infrared sensing of liquid water-film thickness was demonstrated earlier using traditional line-of-sight (LOS) transmission of two lasers with a wavelength-division multiplexing (WDM) approach [29, 32]. On the contrary, on opaque or partially reflecting surfaces the detection of the specular surface reflection from the liquid layer which bears no absorption information needs to be avoided, but the comparatively small fraction of the beam backscattered from the support and having experienced bulk absorption needs to be collected. For this to achieve, a novel technique is presented in this thesis for the single-ended optical measurement of water film thickness using time division multiplexing (TDM) of two near-infrared laser wavelengths. The two interleaving pulse sequences are combined to a single pulse train and transmitted/retro-reflected through the absorption medium, which enables measurements using a single detector. The primary advantage of TDM compared to WDM is the simplification of the optical setup that avoids the additional large signal loss when the emerging beams are diffracted off the grating for angular wavelength separation; TDM therefore improves the signal-to-noise ratio (SNR) in the measurements. In this section, the design and initial demonstration of this sensor with measurements of water film thickness at a fixed temperature will be presented.

The optical setup of the absorption-based film thickness sensor is shown in Fig. 44. The output of two DFB diode lasers operating at 1353 and 1412 nm was combined in a single-mode fiber. Light exiting the fiber was collimated into a free-space beam and 10% of its intensity was split onto a reference (I_R) InGaAs photodiode detector (Thorlabs, PDA10CS). The remaining 90% was directed through the central hole of an off-axis parabolic mirror onto the liquid film spread on the retro-reflecting foil. The foil was placed onto the lower window (as a support) of a temperature-controlled cuvette (LOT), and its distance from the parabolic mirror was adjusted to one RFL. Without a liquid film, the light impinging on the foil were it undergoes diffuse and specular reflection in addition to some absorption by the coated foil. The retro-reflected light was collected by the first parabolic reflector, directed towards a second off axis paraboloid and focused on a second photodetector. A beam dump was arranged to block the specular reflection. All the optical component was mounted an aluminum breadboard (grey rectangle in Fig. 44). In this case, the board was vertically fixed on the optical table. In order to eliminate the specular reflection after reflection of foil (SR, thin solid line in Fig. 44) the incident light was adjusted of an angle of 7° by rotating the aluminum board.

Fig. 45 illustrates the effect of injection-current switching of the two lasers for time-division multiplexing at a 100 Hz repetition rate with a 1-ms off-time between each laser to monitor the detector dark current (i.e., each laser is on for 4 ms). The black lines illustrate the reference signal and the red lines the retro-reflected signal for an empty (Fig. 45a) and a water filled (Fig. 45b) cuvette. Note the much larger absorption by liquid water of the 1412 nm light compared to the 1353 nm light. The two independent waveforms are generated using LabVIEW codes running a National Instruments data acquisition (NI-DAQ) system. The NI-DAQ system consists of a PC equipped with a PCI-6115 DAQ board (12-bit A/D conversion) and a BNC-2110 analog I/O block.

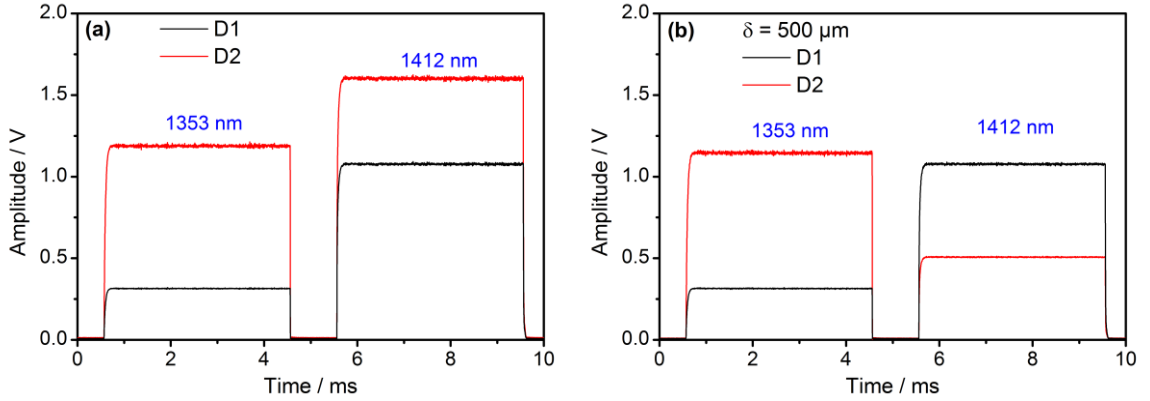


Fig. 45: Measured raw signals in time-division multiplexing: Reference I_R (detector 1, black lines) and film-transmitted retro-reflected laser intensities I_M (detector 2, red lines) through an empty cell (a) and a cell filled with a 500 μm water layer (b).

Background subtraction removes the small DC offset due to ambient light striking the detectors. This is accomplished by subtracting the voltage reading from each detector when all lasers are off. Fluctuations and drifts in the intensity of the lasers are corrected for by taking the ratio at each wavelength of the measured detector signal, I_M , over the reference detector signal, I_R : I_M/I_R . For the RR beam passing twice through the liquid, the laser intensity at wavelength λ can be represented by Beer-Lambert's law as:

$$I_{M,t}^\lambda = (1-u)I_{R,t}^\lambda \frac{I_{M,0}^\lambda}{I_{R,0}^\lambda} \exp\left(-k_{T_L}^\lambda \frac{2\delta}{\cos\alpha}\right), \quad (53)$$

where $I_{M,t}^\lambda$ and $I_{M,0}^\lambda$ are the measured laser intensities at the detector 2 (Fig. 44), in the presence and absence of the liquid, $I_{R,t}^\lambda$ and $I_{R,0}^\lambda$ are the corresponding intensities detected by the reference detector 1 (Fig. 44), respectively, u takes into account the non-specific losses (partial detection of the retro-reflected light, losses through reflection off surfaces,

dirty optics), δ is the film thickness, α is the angle of incidence, and k is the spectral absorption coefficient of water at wavelength λ in dependence on the temperature T_L of the liquid. In the chapter 3, a database of wavelength- and temperature-dependent absorption coefficients for liquid water was acquired by FTIR measurements. Note that Eq. (53) has two unknowns (δ and u) and therefore two laser wavelengths are needed for the detection of δ in a robust calibration-free manner. The liquid-water absorption cross-sections at the two wavelengths of the sensor differ by a factor of ~ 7 . In the case of liquid water, the real part of the refractive index varies by less than 0.3% from 5500 to 7500 cm^{-1} [29]. Therefore, we assume that these non-specific transmission losses u are the same for both wavelengths. By taking the ratio of equations (53) for both wavelengths, the parameter u can thus be eliminated and the film thickness at a fixed temperature can be determined:

$$\delta = \frac{\cos \alpha}{2(k_{T_L}^{1353} - k_{T_L}^{1412})} \ln \frac{I_{M,t}^{1412} I_{M,0}^{1353} I_{R,t}^{1353} I_{R,0}^{1412}}{I_{M,t}^{1353} I_{M,0}^{1412} I_{R,t}^{1412} I_{R,0}^{1353}}. \quad (54)$$

6.4 Results and discussion

6.4.1 Demonstration of liquid-film measurements

Initially, the liquid was enclosed in the cell covered with a quartz plate to validate the sensor's performance for films of known thickness at room temperature ($T_L = 293.5$ K). In Fig. 46, the film thickness evaluated from the absorbance measurements is plotted versus the given separation between the upper quartz plate and the retro-reflecting foil. The dashed straight line represents the one-to-one correspondence between both values. The maximum relative uncertainty in the measured film thickness was 7.5% for a sample thickness of 100 μm (residual in the upper part of Fig. 46a).

Compared to the cuvette used in the transmission measurements there is only one upper window so that a precise determination of the optical path length using the FTIR spectrometer is not possible. In this case, at first the surface roughness of the DG foil with anti-fog coating was quantified by using a profilometer (accuracy approx. ± 15 μm). Then the thickness variation was determined when the different PTFE spacers are pressurized manually using a micrometer, resulting in uncertainties for the various spacer thicknesses of 100 ± 5 , 200 ± 9 , 500 ± 7 , and 1000 ± 12 μm , respectively. The roughness of the foil and the thickness variation of the PTFE spacers enter into the error estimation of the plate –foil distance; this

appears as error bars along the x -axis for each data point. The uncertainty of each measurement in Fig. 46 is calculated through error propagation based on the following parameters in Eq. (54): The uncertainty of the measured liquid temperature using the pyrometer (3 K), the temperature-dependent absorption coefficient k measured in FTIR experiments (a relative variation of 0.62%/K), the angle of incidence (2°), the standard deviation of the average laser intensities (1%), and the standard deviation of all the voltage reading used in the measurement (0.1%).

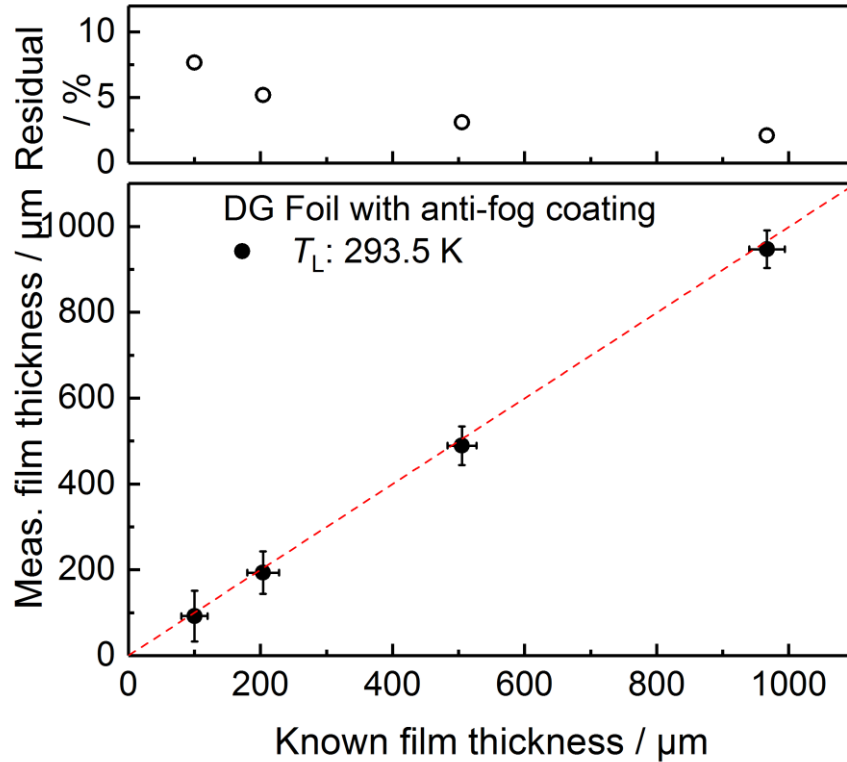


Fig. 46: Measured water film thickness as a function of distance between RR foil and upper quartz window in a calibration cuvette kept at 293.5 K. The upper panel indicates the respective residuals between the measured and nominal layer thickness.

6.4.2 Time-resolved measurements of an evaporating thin film at constant temperature

Further experiments were performed to study the temporal thickness variation of free-standing evaporating water films at constant temperature. The experiment was initiated by dosing and mechanically spreading a proper amount of water onto the retro-reflecting foil such that the initial film thickness was about $700 \mu\text{m}$, which for the present foil dimension was accomplished with 0.175 ml. Temperature (as defined by the temperature regulated

cuvette holder) was kept constant and relative humidity in the lab was measured to be $51 \pm 1\%$. Fig. 47 shows the measured variation of film thickness (solid symbols) as a function of time for evaporating films at 298, 306.4, and 316 K.

As shown in the upper panel in Fig. 47, an estimate of the water temperature (assumed to be close to the temperature of the supporting retro-reflecting foil) was provided by the reading of a pyrometer (pointing towards the foil from above, cf., Fig. 44) during the measurements. It is observed that except for the beginning of the experiment, the film thickness decreases almost linearly with time at all three temperatures, which is in accord with previous experiments where aqueous water films were probed at the same wavelengths in transmission (chapter 4). The thickness reduction rate at the three temperatures was calculated from the slope of fitted lines to the data points and was approximately 7, 11, and 23 $\mu\text{m}/\text{min}$, respectively, for the three temperatures. Note that the thickness reduction rate of pure water film at 316 K (23 $\mu\text{m}/\text{min}$) in this present work is evidently slower than the previous measurement of an evaporating water film at around 332 K (50 $\mu\text{m}/\text{min}$) [29]. In addition, the reduction rate is similar to previous measurement of an evaporating aqueous salt solution film at 318 K (25 $\mu\text{m}/\text{min}$) and obviously higher than the measurement of an evaporating aqueous urea solution film at 318 K (15 $\mu\text{m}/\text{min}$) (chapter 4).

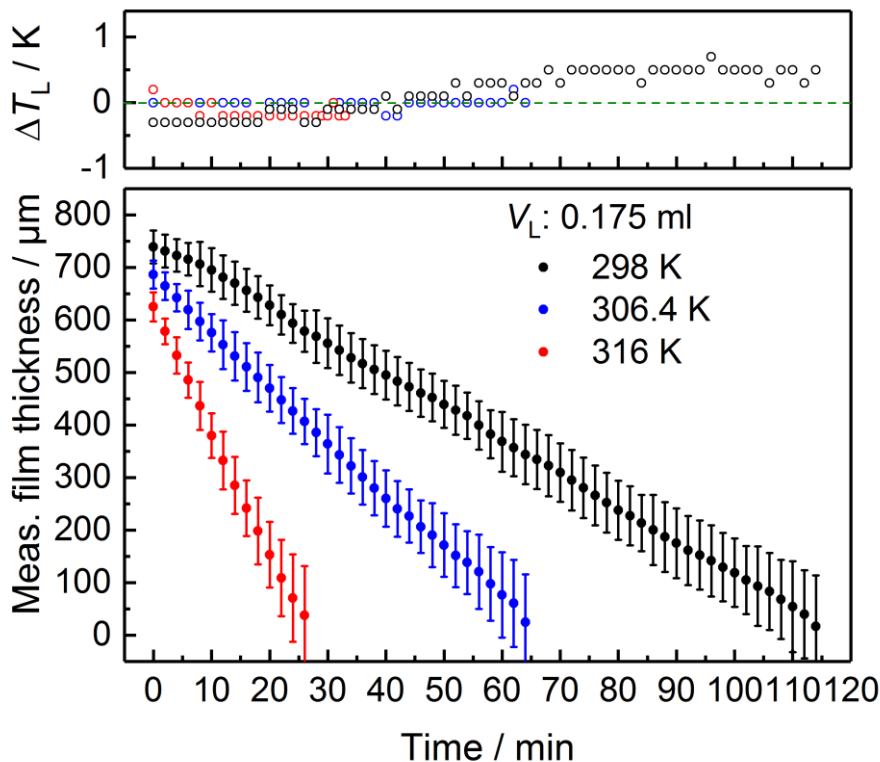


Fig. 47: Temporal variation of film thickness (solid symbols) during evaporation of water films at 298 K (black points), 306.4 K (blue points) and 316 K (red points). The upper panel indicates the variation in water temperature during the experiment measured pyrometrically.

Moreover, when the exposed surface area of the deposited liquid and the liquid temperature are known, the amount of the evaporated water can be estimated as [127]:

$$g_h = \theta A_L (x_s - x), \quad (55)$$

where g_h (in kg/h) is the mass flux of liquid water leaving the surface area A_L (in m^2) of the liquid as vapor, and θ (in kg/m^2h) is the evaporation coefficient, which for an assumed quiescent atmosphere above the liquid takes on a constant value of 25. x_s (in kg/kg) represents the humidity ratio in saturated air at the same temperature as the water surface, and x (in kg/kg) is the given humidity ratio of the surrounding air. The thickness reduction rate at the three temperatures was calculated from Eq. (55) and was approximately 5, 10, and 21 $\mu m/min$ for the three temperatures (i.e., 298, 306.4, and 316 K), respectively. The observed deviations from the measured values could be due to the variation in water temperature during the experiment (upper panel in Fig. 47) and the fact that in the experiment the air above the surface was not fully quiescent.

During the measurement of evaporating films, local de-wetting can occur that can influence the measurement. To record the variation in the film contour, a machine-vision camera (Basler ace acA645-100 gm) was positioned above the setup and images were taken to monitor the water film simultaneously during the evaporation process (shown in Fig. 48 for a 314.8 K case with higher time resolution than in Fig. 47). A filament lamp was used as an illumination source.

It is observed that the film thickness decreases at a constant rate of 21 $\mu m/min$ during the first 28 min after the start of the experiment, after which it decreased with a faster rate of 36 $\mu m/min$ until the film completely evaporated. For nine specific instances in time (blue arrows in Fig. 48), camera images were recorded and are presented in Fig. 49.

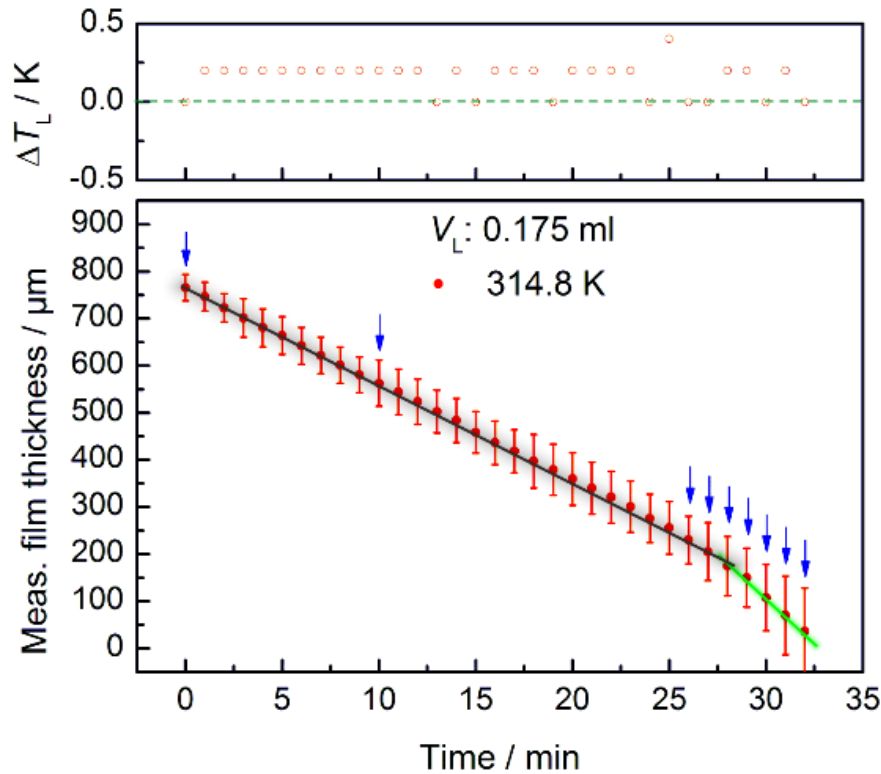


Fig. 48: Absorption-based measurement of the temporal thickness variation during water film evaporation at 314.8 K. Blue arrows: nine specific instances where images were taken with a machine-vision camera in Fig. 49. Black and green solid lines: linear fit to the data points for retrieving the average thickness reduction rate. The upper panel indicates the variation in water temperature during the experiment measured via an optical pyrometer.

The red circle in each image marks the impingement point (IP, ~ 1 mm diameter) of the NIR laser beams on the film. Up to at least 25 min after the start of the experiment (SOE) there is no visible change of the liquid around the IP. Again, the film thickness reduction rate calculated from Eq. (55) of a planar surface is $20 \mu\text{m}/\text{min}$, which is nearly the same as the measurement data. For later times we speculate that the surface topology at that location may be affected by the retracting fluid boundary approaching the IP, as can be deduced from the partial reflections of the lab ceiling lamps in Fig. 49 (bright areas near the IP). This may in turn affect the evaporation behavior due to a change in surface curvature and lead in course to a speed-up in the evaporation rate at and around 28 min after SOE (Fig. 48). From $t = \sim 33$ min, the film was fractured and retracted from the position where the laser beam retro-reflected from the foil surface.

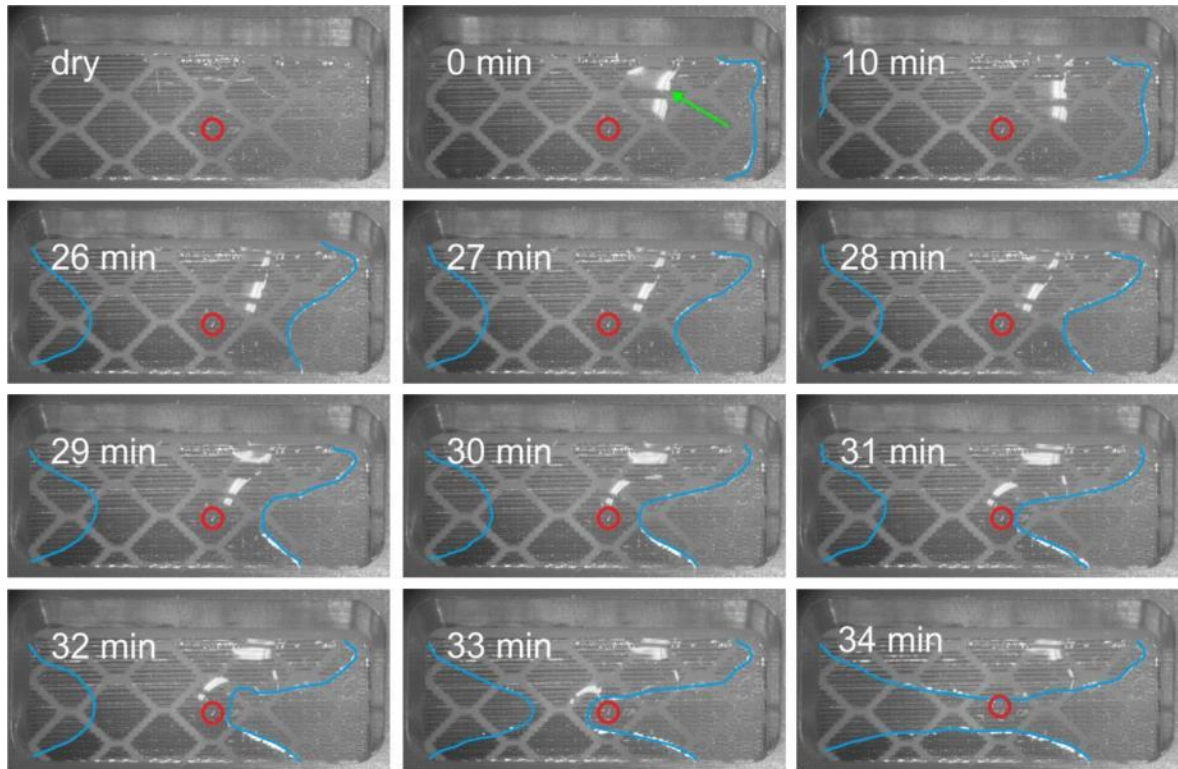


Fig. 49: Photographs at twelve instants (between 0 and 32 min., as marked by arrows in Fig. 48) until the film completely evaporated within the laser beam impingement area. Red circle diode laser impingement point; Green arrow: reflection from room lightings on water surface; Blue lines: boundaries of the water film in the field of view.

6.5 Summary

A single-ended two-color absorption sensor in the NIR spectral range was developed and demonstrated for film-thickness measurements of liquid water on opaque support surfaces. A retro-reflecting foil with anti-fog coating was used as backscattering target. Two off-axis parabolic mirrors were used through one of which the incident laser beam is pointed towards the film and which also served to capture and collimate the retro-reflected or diffuse-reflected beam traversing the film twice. A second off-axis paraboloid then focused the collimated light onto the detector. Time-division multiplexing (TDM) was used as a method more robust (a single detector is sufficient at the receiving end) and with higher optical throughput than, e.g., wavelength-division de-multiplexing.

Validation tests were performed using a temperature-controlled cuvette with known separations between cover window and retro-reflecting foil. The sensor was also demonstrated by recording the time-varying thickness of evaporating water films at known temperatures (298, 306.4, 314.8, and 316 K), where the liquid temperatures were deduced from optical

pyrometry during the measurements. The reduction of the film thickness as a function of time was measured down to approx. 50 μm . The technique may be applied to diverse fields of film diagnostics, e.g., monitoring the evaporation of thin films from smooth or structured surface, such as heat pipes and capillary pumped loops [128], spray and jet impingement cooling [129], falling film evaporation [130] and others.

7 Conclusions and future work

7.1 Conclusions

The objective of this thesis was to investigate liquid thin film sensing in transmission and retro-reflection based on the laser-absorption spectroscopy. For this purpose, Fourier transform infrared (FTIR) measurements of the temperature and solute concentration dependence of the thin films provided the spectral database needed to design the wavelength-multiplexed laser sensor. The spectral database was recorded with a spectral resolution of 2 cm^{-1} in the range $8000\text{--}5500\text{ cm}^{-1}$ ($1.25\text{--}1.82\text{ }\mu\text{m}$). From the variation of the normalized spectra with either solute concentration (dF/dw) or temperature (dF/dT), spectral regions can be identified that are most sensitive to changes in respective parameters.

In this thesis, a wavelength-multiplexed NIR diode laser absorption sensor was developed to measure the layer thickness, solute concentration, and liquid temperature of aqueous NaCl and urea solutions from the evaluation of the absorbance ratios at multiple laser wavelengths. In this study, at least one of the two desired parameters (temperature or solute concentration) is assumed to be known. Validation tests were performed using a temperature-controlled cuvette consisting of two parallel quartz plates providing liquid layers of variable thickness ($200\text{--}1500\text{ }\mu\text{m}$). Validation measurements of films of varying solute concentration at constant temperature and of varying temperature at constant solute concentration provided a proof-of-concept demonstration of the sensor concept. The sensor was successfully applied for simultaneous measurements of liquid-film thickness and solute concentration during time-resolved measurements of evaporating aqueous solution films on a transparent quartz plate at steady temperatures. The faster evaporation at the higher temperature as well as the linear decrease in film thickness and the exponential increase in solute concentration with time were observable from these experiments demonstrating the capabilities of the technique. Furthermore, this study highlighted the need for making this technique more robust and quantitative when applied to practical systems, where the analyzing radiation may pass through spatial regions of strong variation in refractive index or flow-induced surface modifications of liquid films.

The liquid-film temperature and the solute concentration are typically unknown parameters in many practical applications, and diagnostics that recovers the solute concentration and liquid temperature in addition to the film thickness would be preferred. Therefore, a scheme was developed that enables simultaneous monitoring of liquid film thickness, liq-

liquid temperature, and solute concentration of aqueous urea solution, based on a Bayesian methodology. The Bayesian analysis was based on the available temperature- and concentration-dependent spectral database measured by a FTIR spectrometer in the range 5500–8000 cm^{-1} for aqueous urea solutions. This concept was validated with measurements using a calibration cell. Uncertainty in the distribution parameters caused by measurement noise was quantified using Markov-chain Monte-Carlo (MCMC) algorithms, which were used to derive credibility intervals. As a practical demonstration, the temporal variations of film thickness, urea concentration, and liquid temperature were then recorded simultaneously during evaporation of a liquid film deposited on a transparent heated quartz plate.

In addition, a single-ended two-wavelength NIR laser-based absorption sensor was developed and applied for film thickness measurements of liquid water on an opaque support surface using a retro-reflecting foil with anti-fog coating. Laser wavelengths at 1412 and 1353 nm were used where the temperature dependence of the liquid water absorption cross section was known. The lasers were fiber coupled and the detection of the retro-reflected light was accomplished through a multimode fiber and a single photodiode using time-division multiplexing (TDM). This absorption method relies on the measurement of the light that has been attenuated by traveling twice through the liquid layer (e.g., reflected diffusely or directionally from the supporting solid surface). Therefore, the partial reflection from the front surface must be suppressed. In the approach reported in this thesis these signals were separated geometrically (cf., Fig. 44). The water-film thickness at a given temperature was determined from measured transmittance ratios at the two laser wavelengths. This technique was demonstrated using a temperature controlled cell providing liquid layers of variable and known thickness between 100 and 1000 μm using PTFE spacers. Furthermore, the sensor was successfully applied to record the time-varying thickness of evaporating water films at three known temperatures. Liquid films down to approx. 50 μm were measured in the presence of water vapor above the liquid during the evaporation.

7.2 Future work

Several ideas of further research remain for extending the current work, which are described below.

In the present work, the film thickness was recorded down to 50 μm using the diode laser-based absorption sensor. To extend the sensitivity range for measuring small film thickness (below 50 μm), absorption in the ~ 2 μm wavelength range (in which still the convenient

fiber-based handling of sender and receiver is possible) could be explored where liquid water/aqueous solutions exhibits larger absorption cross sections by approximately a factor of 4.5, compared to the spectral region ($\sim 1.4 \mu\text{m}$) used in this thesis. The selection of new wavelengths would require an extended database, and new FTIR measurements need to be performed to provide the necessary information for the variation of the absorption spectrum in this new wavelength region as a function of temperature and solute concentration.

In practical applications of liquid film diagnostics, double-ended transmission measurements are not feasible since optical access is often possible from one side only. We already demonstrated the feasibility of a single-ended two-color absorption sensor using a retro-reflecting foil with anti-fog coating as backscattering target (chapter 6). Furthermore, many practical situations feature liquid films that vary dynamically, such as a wavy surface topology due to boundary layer effects between gas and liquid phase, film breakup, wave formation during and after film deposition. In these cases, beam steering, defocusing, or even breakup of the analysis beam might take place due to the difference in the index of refraction of the liquid versus vapor media. Future work could extend this measurement strategy to the more challenging situation of films deposited on opaque rough surfaces (e.g., stainless steel, ceramic) with diffuse scattering instead of retro-reflecting behavior, and dynamic measurements in flow channels.

Liquid films have broad unstructured absorption features and tunable narrow-band light sources are not required for their measurement. Therefore, at least some of the lasers could be replaced by cheaper light sources (e.g., light-emitting diode (LED)) [131-134]. Fig. 50 shows three examples of NIR-LEDs (IBSG) emitting at around 1100, 1530, and 1950 nm with half widths of about 100 nm, which overlap part of the wavelength region around the broad liquid water absorption peak. The Table 18 below summarizes some of the manufacturer's specified operating characteristics. The divergence angle of the LED output light is around 15° and the optical power is much lower than diode laser. Therefore, the standoff distance for these units in the film measurement is limited.

Table 18: Specified optical-electrical characteristics of the LEDs

Model	Wavelength / μm			FWHM / nm		Optical power / mW	
	Min	Typ	Max	Min	Max	Min	Max
LED11HP	1.09	1.10	1.15	60	80	4.5	9
LED15HP	1.51	1.53	1.55	90	150	2.5	5
LED19HP	1.92	1.95	1.97	100	200	0.8	1.2

Furthermore, the influence of water vapor interference absorption on the total absorption signal in these wavelength ranges needs to be considered (red lines in Fig. 50). These limitations need to be further investigated and the devices could then be tested for fluid phase measurements in beam transmission and backscattering arrangements.

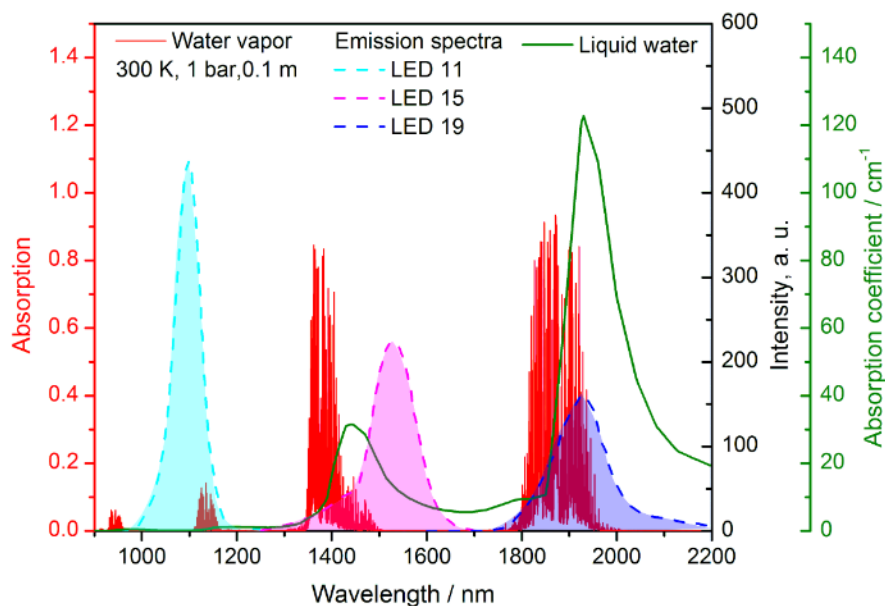


Fig. 50: Absorption spectrum of water vapor in the NIR region based on HITRAN 2012 (red lines), emission spectra of the LEDs (light blue, pink, and violet shaded spectra), and liquid water absorption spectrum (green curve).

8 Own publications originating from this thesis

8.1 Articles in peer-reviewed journals

1. R. Pan, J.B. Jeffries, T. Dreier, and C. Schulz, "Measurements of liquid film thickness, concentration and temperature of aqueous NaCl solution by NIR absorption spectroscopy", *Appl. Phys. B* **120**, 397(2015)
2. R. Pan, J.B. Jeffries, T. Dreier, and C. Schulz, "Measurements of liquid film thickness, concentration and temperature of aqueous urea solution by NIR absorption spectroscopy", *Appl. Phys. B* **122**, 4 (2016)
3. R. Pan, C. Brocksieper, J.B. Jeffries, T. Dreier, and C. Schulz, "Diode laser-based standoff absorption measurement of water film thickness in retro-reflection", *Appl. Phys. B* **122**, 249 (2016)
4. R. Pan, K.J. Daun, T. Dreier, and C. Schulz, "Uncertainty quantification and design-of-experiment in absorption-based aqueous film parameter measurements using Bayesian inference", *Appl. Opt.* **56**, E1-E7, (2017)

8.2 Non peer-reviewed articles and conference presentations

1. R. Pan, J.B. Jeffries, T. Dreier, and C. Schulz, "Measurements of liquid film thickness and solute concentration of aqueous NaCl solution by absorption spectroscopy", (Laser Applications to Chemical, Security, and Environment Analysis (LACSEA), conference paper, Seattle, Washington, USA, 2014)
2. R. Pan, J.B. Jeffries, T. Dreier, and C. Schulz, "Measurements of liquid film thickness and solute concentration of aqueous NaCl solution by absorption spectroscopy", (Laser Applications to Chemical, Security, and Environment Analysis (LACSEA), Poster, Seattle, Washington, USA, 2014)
3. R. Pan, Kyle J. Daun, T. Dreier, and C. Schulz, "Uncertainty quantification and design-of-experiment in NIR absorption spectroscopy using Bayesian Inference", (Gordon Conference on Laser Diagnostics in Combustion, Poster, Waterville Valley, NH, 2015)
4. R. Pan, J.B. Jeffries, T. Dreier, and C. Schulz, "Measurements of liquid film thickness, concentration and temperature of aqueous of NaCl and urea solution by NIR absorption spectroscopy", GRC, (Gordon Conference on Laser Diagnostics in Combustion, Poster, Waterville Valley, NH, 2015)

5. R. Pan, J.B. Jeffries, T. Dreier, and C. Schulz, "DLAS-based measurement of water film thickness in Retro-Reflection", (Laser Applications to Chemical, Security, and Environment Analysis (LACSEA), conference paper, Heidelberg, Germany, 2016)

9 References

1. M. Drake, T. Fansler, A. Solomon, and G. Szekely, "Piston fuel films as a source of smoke and hydrocarbon emissions from a wall-controlled spark ignited direct-injection engine," SAE Technical Paper, 2003010547 (2003).
2. P. Felton, D. Kyritsis, and S. Fulcher, "LIF visualization of liquid fuel in the intake manifold during cold start," SAE Technical Paper, 952464 (1995).
3. W. Hentschel, A. Grote, and O. Langer, "Measurement of wall film thickness in the intake manifold of a standard production SI engine by a spectroscopic technique," SAE Technical Paper, 972832 (1997).
4. G. Rottenkolber, J. Gindele, J. Raposo, K. Dullenkopf, W. Hentschel, S. Wittig, U. Spicher, and W. Merzkirch, "Spray analysis of a gasoline direct injector by means of two-phase PIV," *Exp. Fluids* **32**, 710-721 (2002).
5. S. Wigger, H. J. Füller, D. Fuhrmann, C. Schulz, and S. A. Kaiser, "Quantitative two-dimensional measurement of oil-film thickness by laser-induced fluorescence in a piston-ring model experiment," *Appl. Opt.* **55**, 269-279 (2016).
6. N. Grice, and I. Sherrington, "An Experimental Investigation into the Lubrication of Piston Rings in an Internal Combustion Engine-Oil Film Thickness Trends, Film Stability and Cavitation," SAE Technical Paper, 930688 (1993).
7. H. Inagaki, A. Saito, M. Murakami, and T. Konomi, "Development of Two-Dimensional Oil Film Thickness Distribution Measuring System," SAE Technical Paper, 952346 (1995).
8. J. R. Mawhinney, and J. K. Richardson, "A review of water mist fire suppression research and development," *Fire Technol.* **33**, 54-90 (1996).
9. T. A. Shedd, and T. A. Newell, "Automated optical liquid film thickness measurement method," *Rev. Sci. Instrum.* **69**, 4205-4213 (1998).
10. H. Glade, K. Krömer, S. Will, S. Nied, S. M. Pancera, and G. Schürmann, "Scale formation of mixed salts in multiple-effect distillers," *IDA Journal* **2**, 38-44 (2010).
11. J. Gieshoff, M. Pfeifer, A. Schafer-Sindlinger, P. C. Spurk, G. Garr, T. Leprince, and M. Crocker, "Advanced urea SCR catalysts for automotive applications," SAE Technical Paper, 2001010514 (2001).
12. F. Birkhold, U. Meingast, P. Wassermann, and O. Deutschmann, "Analysis of the injection of urea-water-solution for automotive SCR deNO_x-systems: Modeling of two-phase flow and spray/wall-interaction," SAE Technical Paper, 2006-2001-0643 (2006).

-
13. I. Nova, and E. Tronconi, eds., *Urea-SCR technology for deNOx after treatment of diesel exhausts* (Springer, New York, 2014).
 14. A. Schagen, and M. Modigell, "Local film thickness and temperature distribution measurement in wavy liquid films with a laser-induced luminescence technique," *Exp. Fluids* **43**, 209-221 (2007).
 15. F. Birkhold, U. Meingast, P. Wassermann, and O. Deutschmann, "Modeling and simulation of the injection of urea-water-solution for automotive SCR deNOx-systems," *Appl. Catal. B: Environ.* **70**, 119-127 (2005).
 16. R. J. Belt, J. M. C. V. t. Westende, H. M. Prasser, and L. M. Portela, "Time and spatially resolved measurements of interfacial waves in vertical annular flow," *Int. J. Multiph. Flow* **36**, 570-587 (2010).
 17. M. Damsohn, and H. M. Prasser, "High-speed liquid film sensor with high spatial resolution," *Meas. Sci. Technol.* **20**, 114001-114009 (2009).
 18. T. Fukano, and A. Ousaka, "Prediction of the circumferential distribution of film thickness in horizontal and near-horizontal gas-liquid annular flows," *Int. J. Multiph. Flow* **15**, 403-419 (1989).
 19. Y. Hagiware, E. Esmaeilzadeh, H. Tsutsui, and K. Suzuki, "Simultaneous measurement of liquid film thickness, wall shear stress and gas flow turbulence of horizontal wavy two-phase flow," *Int. J. Multiph. Flow* **15**, 421-431 (1989).
 20. G. E. Thorncroft, and J. F. Klausner, "A capacitance sensor for two-phase liquid film thickness measurements in a square duct," *ASME J. Fluids Eng.* **119**, 164-169 (1997).
 21. I. B. Özdemir, and J. H. Whitelaw, "An optical method for the measurement of unsteady film thickness," *Exp. Fluids* **13**, 321-331 (1992).
 22. P. Kelly-Zion, W. Collins, and D. Glawe, "Application of laser interferometry for transient film thickness measurements," in *ASME Heat Transfer/Fluids Engineering Summer Conference*, (Charlotte, North Carolina, USA, 2004), pp. 501-507.
 23. N. Borgetto, C. Galizzi, F. André, and D. Escudié, "A thickness measurement technique based on low-coherence interferometry applied to a liquid film with thermal gradient," *Exp. Therm. Fluid Sci.* **34**, 1242-1246 (2010).
 24. S. K. Debnath, M. P. Kothiyal, J. Schmit, and P. Hariharan, "Spectrally resolved phase-shifting interferometry of transparent thin films: sensitivity of thickness measurements," *Appl. Opt.* **45**, 8636-8640 (2006).
 25. F. Gao, H. Muhamedsalih, and X. Jiang, "Surface and thickness measurement of a transparent film using wavelength scanning interferometry," *Opt. Express* **20**, 21450-21456 (2012).
-

-
26. T. Ohyama, K. Endoh, A. Mikami, and Y. H. Mori, "Optical interferometry for measuring instantaneous thickness of transparent solid and liquid films," *Rev. Sci. Instrum.* **59**, 2018-2022 (1988).
 27. A. A. Mouza, N. A. Vlachos, S. V. Paras, and A. J. Karabelas, "Measurement of liquid film thickness using a laser light absorption method," *Exp. Fluids* **28**, 355-359 (2000).
 28. J. M. Porter, J. B. Jeffries, and R. K. Hanson, "Mid-infrared laser-absorption diagnostic for vapor-phase fuel mole fraction and liquid fuel film thickness," *Appl. Phys. B* **102**, 345-355 (2011).
 29. H. Yang, D. Greszik, I. Wlokas, T. Dreier, and C. Schulz, "Tunable diode laser absorption sensor for the simultaneous measurement of water film thickness, liquid- and vapor-phase temperature," *Appl. Phys. B* **104**, 21-27 (2011).
 30. H. Yang, X. Guo, W. Zhou, B. Chen, J. Hu, M. Su, and X. Cai, "Investigation on liquid film of urea-water solutions with diode laser absorption spectroscopy," *Exp. Fluids* **56:73**, (2015).
 31. S. Wittig, J. Himmelsbach, B. Noll, H. J. Feld, and W. Samenfink, "Motion and evaporation of shear-driven liquid films in turbulent gases," *J. Eng. Gas Turbines Power* **114**, 395-400 (1992).
 32. H. Yang, D. Greszik, T. Dreier, and C. Schulz, "Simultaneous measurement of liquid water film thickness and vapor temperature using near-infrared tunable diode laser spectroscopy," *Appl. Phys. B* **99**, 385-390 (2010).
 33. W. French, D. Rose, P. Kelly-Zion, and C. Pursell, "Analysis of evaporating fuel films using shadowgraph and schlieren imaging techniques," SAE Technical Paper, 2008012443 (2008).
 34. E. Kull, G. Wiltafsky, W. Stolz, K. D. Min, and E. Holder, "Two-dimensional visualization of liquid layers on transparent walls," *Opt. Lett.* **22**, 645-647 (1997).
 35. M. Alonso, P. J. Kay, P. J. Bowen, R. Gilchrist, and S. Sapsford, "A laser induced fluorescence technique for quantifying transient liquid fuel films utilising total internal reflection," *Exp. Fluids* **48**, 132-142 (2010).
 36. D. Greszik, H. Yang, T. Dreier, and C. Schulz, "Measurement of water film thickness by laser-induced fluorescence and Raman imaging," *Appl. Phys. B* **102**, 123-132 (2011).
 37. C. H. Hidrovo, and D. P. Hart, "Emission reabsorption laser induced fluorescence (ERLIF) film thickness measurement," *Meas. Sci. Technol.* **12**, 467-477 (2001).
 38. R. K. Hanson, "Applications of quantitative laser sensors to kinetics, propulsion and practical energy systems," *Proc. Combust. Inst.* **33**, 1-40 (2011).
-

-
39. M. G. Allen, "Diode laser absorption sensors for gas dynamic and combustion flows," *Meas. Sci. Technol.* **9**, 545-562 (1998).
 40. J. Wolfrum, T. Dreier, V. Ebert, and C. Schulz, "Laser-based combustion diagnostics," in *Encyclopedia of Analytical Chemistry*, R. A. Meyers, ed. (J. Wiley & Sons Ltd., Chichester, 2000), 2118-2148.
 41. S. T. Sanders, J. A. Baldwin, T. P. Jenkins, D. S. Baer, and R. K. Hanson, "Diode-Laser sensor for monitoring multiple combustion parameters in pulse detonation engines," *Proc. Comb. Inst.* **28**, 587-594 (2000).
 42. G. B. Rieker, J. B. Jeffries, and R. K. Hanson, "Calibration-free wavelength-modulation spectroscopy for measurements of gas temperature and concentration in harsh environments," *Appl. Opt.* **48**, 5546-5560 (2009).
 43. W. A. P. Luck, "Structure of water and aqueous solutions," in *Proceedings of the international symposium*, (Weinheim: Verlag Chemie, Marburg, 1974), 248-284.
 44. E. Hecht, *Optics, 4th ed.* (Pearson Addison Wesley, San Francisco, 2002).
 45. W. Unterberg, "Studies of liquid film flow and evaporation with reference to saline water distillation," (Dissertation, University of California, Department of Engineering, Los Angeles, USA, 1961).
 46. C. Schulz, and V. Sick, "Tracer-LIF diagnostics: quantitative measurement of fuel concentration, temperature and fuel/air ratio in practical combustion systems," *Prog. Energy Combust. Sci.* **31**, 75-121 (2005).
 47. B. Commoner, and D. Lipkin, "The application of the Beer-Lambert Law to optically anisotropic systems," *Science* **110**, 41-43 (1949).
 48. J. M. Porter, J. B. Jeffries, and R. K. Hanson, "Mid-infrared absorption measurements of liquid hydrocarbon fuels near 3.4 μm ," *J. Quant. Spectrosc. Radiat. Transfer* **110**, 2135-2147 (2009).
 49. D. W. Ball, *Field guide to spectroscopy* (SPIE Press, Bellingham WA, 2006).
 50. H. Haken, and H. C. Wolf, *Molecular physics and elements of quantum chemistry: introduction to experiments and theory, 2nd ed.* (Springer-Verlag Berlin-Heidelberg-New York, 2004).
 51. H. Günzler, and H. M. Heise, *IR Spectroscopy* (WILEY-VCH Verlag GmbH, Weinheim, 2002).
 52. W. Demtröder, *Laser Spectroscopy: Basic Concepts and Instrumentation* (Springer, Berlin, 1996).
 53. P. W. Atkins, *Physikalische Chemie* (Wiley-VCH Weinheim, 2006).
-

-
54. P. Williams, and K. Norris, *Near-Infrared Technology in the Agriculture and Food Industries, 2nd ed.* (The American Association of Cereal Chemists, St. Paul, MN, 2001).
 55. H. Haken, and H. C. Wolf, *The physics of atoms and quanta: introduction to experiments and theory, 7th ed.* (Springer-Verlag Berlin-Heidelberg-New York, 2007).
 56. H. W. Siesler, Y. Ozaki, S. Kawata, and H. M. Heise, *Near-Infrared Spectroscopy: Principles, Instruments, Applications* (Wiley-VCH, Weinheim, Germany, 2002).
 57. T. Schimanouchi, "Tables of molecular vibrational frequencies, consolidated Vol. 1," N. S. R. Data, ed. (Nat. Bur. Stand., U.S., 1972).
 58. D. A. Skoog, and J. J. Leary, *Instrumentelle analytik* (Springer-Verlag, Berlin-Heidelberg-New York, 1992).
 59. D. Eisenberg, and W. Kauzmann, *The structure and properties of water* (Oxford University Press, London, 1969).
 60. J. J. Max, and C. Chapados, "Isotope effects in liquid water by infrared spectroscopy. III. H₂O and D₂O spectra from 6000 to 0 cm⁻¹," *J. Chem. Phys.* **131**, 184505-184518 (2009).
 61. L. S. Rothman, I. E. Gordon, Y. Babikov, A. Barbe, D. C. Benner, P. F. Bernath, M. Birk, L. Bizzocchi, V. Boudon, L. R. Brown, A. Campargue, K. Chance, E. A. Cohen, L. H. Coudert, V. M. Devi, B. J. Drouin, A. Faytl, J.-M. Flaud, R. R. Gamache, J. J. Harrison, J.-M. Hartmann, C. Hill, J. T. Hodges, D. Jacquemart, A. Jolly, J. Lamouroux, R. J. L. Roy, G. Li, D. A. Long, O. M. Lyulin, C. J. Mackie, S. T. Massie, S. Mikhailenko, H. S. P. Müller, O. V. Naumenko, A. V. Nikitin, J. Orphal, V. Perevalov, A. Perrin, E. R. Polovtseva, C. Richard, M. A. H. Smith, E. Starikova, K. Sung, S. Tashkun, J. Tennyson, G. C. Toon, V. G. Tyuterev, and G. Wagner, "The HITRAN 2012 molecular spectroscopic database," *J. Quant. Spectrosc. Radiat. Transfer* **130**, 4-50 (2013).
 62. R. Röttgers, D. McKee, and C. Utschig, "Temperature and salinity correction coefficients for light absorption by water in the visible to infrared spectral region," *Opt. Express* **22**, 25093-25108 (2014).
 63. L. Kou, D. Labrie, and P. Chylek, "Refractive indices of water and ice in the 0.65- to 2.5-microm spectral range," *Appl. Opt.* **32**, 3531-3540 (1993).
 64. H. Yang, "Tunable diode-laser absorption-based sensors for the detection of water vapor concentration, film thickness and temperature," in *Institute for combustion and gas dynamics*, (Dissertation, University of Duisburg-Essen, Germany, Duisburg, 2012).
 65. P. Griffiths, and J. D. Haseth, *Fourier Transform Infrared Spectrometry, 2nd edn.* (John Wiley & Sons, 2007).
-

-
66. J. Kiefer, A. Bösmann, and P. Wasserscheid, "Quantitative measurement of complex substances dissolved in an ionic liquid using IR spectroscopy and chemometrics," *Tech. Messen* **84**, 32-37 (2017).
 67. W. D. Perkins, "Fourier transform infrared spectroscopy. Part II. Advantages of FT-IR," *J. Chem. Educ.* **64**, A269-A271 (1987).
 68. M. Born, and E. Wolf, *Principles of Optics: Electromagnetic Theory of Propagation, Interference, and Diffraction of Light* (Pergamon Press, London, 1959).
 69. I. Thormählen, J. Straub, and U. Grigull, "Refractive index of water and its dependence on wavelength, temperature, and density," *J. Phys. Chem. Ref. Data* **14**, 933-645 (1985).
 70. J. R. Warren, and J. A. Gordon, "On the refractive indices of aqueous solutions of urea," *J. Phys. Chem.* **70**, 297-300 (1966).
 71. O. Söhnel, and P. Novotny, *Densities of aqueous solutions of inorganic substances* (Elsevier, Amsterdam, 1985).
 72. A. V. Wolf, *Aqueous solutions and body fluids* (Harper & Row, New York, 1966).
 73. G. M. Hale, and M. R. Querry, "Optical constants of water in the 200-nm to 200- μ m wavelength region," *Appl. Opt.* **12**, 555-563 (1973).
 74. J. R. Collins, "Change in the infra-red absorption spectrum of water with temperature," *Phys. Rev.* **26**, 771-779 (1925).
 75. J. Lin, and C. W. Brown, "Near-IR spectroscopic determination of NaCl in aqueous solution," *Appl. Spectrosc.* **46**, 1809-1815 (1992).
 76. J. Lin, and C. W. Brown, "Simultaneous determination of physical and chemical properties of sodium chloride solutions by near infrared spectroscopy," *J. Near Infrared Spectrosc.* **1**, 109-120 (1993).
 77. J. Lin, and C. W. Brown, "Novel applications of near-infrared spectroscopy of water and aqueous solutions from physical chemistry to analytical chemistry," *Trends Anal. Chem.* **13**, 320-326 (1994).
 78. A. A. Gowen, J. M. Amigo, and R. Tsenkova, "Characterisation of hydrogen bond perturbations in aqueous systems using aquaphotomics and multivariate curve resolution-alternating least squares," *Anal. Chim. Acta* **759**, 8-20 (2013).
 79. K. M. Aly, and E. Esmail, "Refractive index of salt water: effect of temperature," *Opt. Mater.* **2**, 195-199 (1993).
 80. X. Ning, "Investigation of aqueous salt, glucose and urea solutions by using FTIR spectroscopy," (Bachelor thesis, University of Duisburg-Essen, Germany, 2015).
-

-
81. S. Park, and M. D. Fayer, "Hydrogen bond dynamics in aqueous NaBr solutions," *Proc. Natl. Acad. Sci. U.S.A* **104**, 16731-16738 (2007).
 82. J. V. Frost, and K. Molt, "Analysis of aqueous solutions by near-infrared spectrometry (NIRS). III. Binary mixtures of inorganic salt in water.," *J. Mol. Struct.* **410-411**, 573-579 (1997).
 83. R. K. Hanson, "Applications of quantitative laser sensors to kinetics, propulsion and practical energy systems," *Proc. Comb. Inst.* **33**, 1-40 (2011).
 84. G. R. Choppin, and K. Buijs, "Near infrared studies of the structure of water. II. Ionic solutions," *J. Chem. Phys.* **39**, 2042-2050 (1963).
 85. E. A. Galinski, "Compatible solutes of halophilic eubacteria: molecular principles, water-solute interaction, stress protection," *Experientia* **49**, 487-496 (1993).
 86. E. A. Galinski, M. Stein, B. Amendt, and M. Kinder, "The kosmotropic (structure-forming) effect of compensatory solutes," *Comp. Biochem. Physiol. A Mol. Integr. Physiol.* **117**, 357-365 (1997).
 87. J. J. Workman, and L. Weyer, eds., *Practical guide to interpretive near-infrared spectroscopy* (CRC Press, London, 2007).
 88. J. Gordadolnik, and Y. Marechal, "Urea and urea-water solutions - An infrared study," *J. Mol. Struct.* **615**, 177-189 (2002).
 89. M. Lever, K. Randall, and E. A. Galinski, "Near infra-red spectra of urea with glycine betaine or trimethylamine N-oxide are additive," *Biochim. Biophys. Acta* **1528**, 135-140 (2001).
 90. A. Henriques, J. Martins, J. Ferra, F. D. Magalhaes, and L. Carvalho, "Influence of temperature variations in near infrared of urea and formaldehyde solutions," in *16th International Conference on Near Infrared Spectroscopy*, (France, 2013), pp. 419-423.
 91. M. C. Stumpe, and H. Grubmüller, "Aqueous Urea Solutions: Structure, Energetics, and Urea Aggregation," *J. Phys. Chem. B* **111**, 6220-6228 (2007).
 92. H. Maeda, Y. Ozaki, M. Tanaka, N. Hayashi, and T. Kojima, "Near infrared spectroscopy and chemometrics studies of temperature-dependent spectral variations of water: relationship between spectral changes and hydrogen bonds," *J. Near Infrared Spectrosc.* **3**, 191-201 (1995).
 93. R. Goldstein, and S. S. Penner, "The near-infrared absorption of liquid water at temperatures between 27 and 209°C," *J. Quant. Spectrosc. Radiat. Transfer.* **4**, 441-451 (1963).
-

-
94. R. F. Hankel, A. Günther, K. E. Wirth, A. Leipertz, and A. Braeuer, "Liquid phase temperature determination in dense water sprays using linear raman scattering," *Opt. Express* **22**, 7962-7971 (2014).
 95. P. R. Bevington, and D. K. Robinson, *Data reduction and error analysis for the physical sciences* (McGraw-Hill, second edition, 1992).
 96. R. Pan, J.B. Jeffries, T. Dreier, and C. Schulz, "Measurements of liquid film thickness, concentration and temperature of aqueous NaCl solution by NIR absorption spectroscopy," *Appl. Phys. B* **120**, 397-406 (2015).
 97. R. Pan, J. B. Jeffries, T. Dreier, and C. Schulz, "Measurements of liquid film thickness, concentration, and temperature of aqueous urea solution by NIR absorption spectroscopy," *Appl. Phys. B* **122:4**, 1-10 (2016).
 98. C. Dale Keefe, T. Wilcox, and E. Campbell, "Measurement and applications of absolute infrared intensities," *J. Mol. Struct.* **1009**, 111-122 (2012).
 99. H. Yang, D. Greszik, I. Wlokas, T. Dreier, and C. Schulz, "Tunable diode laser absorption sensor for the simultaneous measurement of water film thickness, liquid- and vapor-phase temperature," *Appl. Phys. B* **104**, 21-27 (2011).
 100. R. J. Bartula, and S. T. Sanders, "Estimation of signal noise induced by multimode optical fibers," *Opt. Eng.* **47**, 035002-035007 (2008).
 101. S. T. Sanders, J. A. Baldwin, T. P. Jenkins, D. S. Baer, and R. K. Hanson, "Diode-Laser sensor for monitoring multiple combustion parameters in pulse detonation engines," *Proc. Combust. Inst.* **28**, 587-594 (2000).
 102. R. W. Style, and J. S. Wettlaufer, "Evaporatively driven morphological instability " *Phys. Rev. E* **76**, 11602-11607 (2007).
 103. F. Fadul, A. Nelli, and A. Fakheri, "Urea mixing in selective catalytic reduction systems," in *ASME International Mechanical Engineering Congress and Exposition*, (Seattle, WA, 2008).
 104. M. A. Motin, T. K. Biswas, and E. M. Huque, "Volumetric and viscometric studies on aqueous urea solution," *Phys. Chem. Liq.* **40**, 593-605 (2002).
 105. K. Kawahra, and C. Tanford, "Viscosity and density of aqueous solutions of urea and guanidine hydrochloride," *J. Biol. Chem.* **241**, 3228-3232 (1966).
 106. R. Pan, K. J. Daun, T. Dreier, and C. Schulz, "Uncertainty quantification and design-of-experiment in absorption-based aqueous film parameter measurements using Bayesian inference," *Appl. Opt.* **56**, E1-E7 (2017).
 107. R. C. Aster, B. Borchers, and C. H. Thurber, *Parameter Estimation and Inverse Problems* (Elsevier, Waltham, MA, USA, 2012).
-

-
108. R. Feeley, M. Frenklach, M. Onsum, T. Russi, A. Arkin, and A. Packard, "Model discrimination using data collaboration," *J. Phys. Chem. A* **110**, 6803-6813 (2006).
 109. D. S. Sivia, *Data Analysis: A Bayesian Tutorial* (Oxford University Press, New York, USA, 2006).
 110. U. V. Toussaint, "Bayesian inference in physics," *Rev. Mod. Phys.* **83**, 943-999 (2011).
 111. T. A. Sipkens, R. Mansmann, K. J. Daun, N. Petermann, J. T. Titantah, M. Karttunen, H. Wiggers, T. Dreier, and C. Schulz, "In situ nanoparticle size measurements of gas-borne silicon nanoparticles by time-resolved laser-induced incandescence," *Appl. Phys. B* **116**, 623-636 (2014).
 112. P. J. Hadwin, T. A. Sipkens, K. A. Thomson, F. Liu, and K. J. Daun, "Quantifying uncertainty in soot volume fraction estimates using Bayesian inference of auto-correlated laser-induced incandescence measurements," *Appl. Phys. B* **122:1**, 1-16 (2016).
 113. C. P. Robert, and G. Casella, *Monte Carlo Statistical Methods, 2nd edition* (Springer, New York, 2004).
 114. D. Calvette, and E. Somersalo, *Introduction to Bayesian Scientific Computing* (Springer, New York, 2008).
 115. A. Tarantola, *Inverse Problem Theory and Methods for Model Parameter Estimation* (SIAM, Philadelphia, 2005).
 116. J. Kaipio, and E. Somersalo, *Statistical and Computational Inverse Problems, 2nd ed.* (Springer Science & Business Media, New York, 2006).
 117. R. Charnigo, M. Francoeur, P. Kenkel, M. P. Mengüç, B. Hall, and C. Srinivasan, "Credible intervals for nanoparticle characteristics," *J. Quant. Spectrosc. Radiat. Transfer* **113**, 182-193 (2012).
 118. W. H. Press, S. A. Teukolsky, W. T. Vetterling, and B. P. Flannery, *Numerical Recipes: The Art of Scientific Computing* (Cambridge University Press, Cambridge, 2007).
 119. A. W. Bowman, and A. Azzalini, *Applied Smoothing Techniques for Data Analysis* (Oxford University Press, Oxford, 1997).
 120. A. I. Toryanik, and E. M. Topalova, "Effect of urea on the structure of water over a wide temperature range," *J. Struct. Chem.* **26**, 830-832 (1985).
 121. R. Pan, C. Brocksieper, J. B. Jeffries, T. Dreier, and C. Schulz, "Diode laser-based standoff absorption measurement of water film thickness in retro-reflection," *Appl. Phys. B* **122**, 249-255 (2016).
-

-
122. J. Chen, A. Hangauer, R. Strzoda, and M. C. Amann, "Laser spectroscopy oxygen sensor using diffuse reflector based optical cell and advanced signal processing," *Appl. Phys. B* **100**, 417-425 (2010).
 123. A. Seidel, S. Wangner, and V. Ebert, "TDLAS-based open-path laser hygrometer using simple reflective foils as scattering targets," *Appl. Phys. B* **109**, 497-504 (2012).
 124. Z. Wang, and S. T. Sanders, "Toward single-ended absorption spectroscopy probes based on backscattering from rough surfaces: H₂O vapor measurements near 1350 nm," *Appl. Phys. B* **121**, 187-192 (2015).
 125. C. S. Goldenstein, R. M. Spearrin, and R. K. Hanson, "Fiber-coupled diode-laser sensors for calibration free stand-off measurements of gas temperature, pressure, and composition," *Appl. Opt.* **55**, 479-484 (2016).
 126. A. Seidel, S. Wagner, A. Dreizler, and V. Ebert, "Robust, spatially scanning, open-path TDLAS hygrometer using retro-reflective foils for fast tomographic 2-D water vapor concentration field measurements," *Atmos. Meas. Tech.* **8**, 2061-2068 (2015).
 127. The Engineering Toolbox, http://www.engineeringtoolbox.com/evaporation-water-surface-d_690.html, (2016).
 128. P. Stephan, and C. A. Busse, "Analysis of the heat transfer coefficient of grooved heat pipe evaporator walls," *Int. J. Heat Mass Transfer* **35**, 383-391 (1992).
 129. D. W. Zhou, and C. F. Ma, "Local jet impingement boiling heat transfer with R113," *Heat Mass Transfer* **40**, 539-549 (2004).
 130. T. Gambaryan-Roisman, and P. Stephan, "Analysis of falling film evaporation on grooved surfaces," *J. Enhanced Heat Transfer* **10**, 445-458 (2003).
 131. D. A. Bui, and P. C. Hauser, "Analytical devices based on light-emitting diodes – a review of the state-of-the-art," *Anal. Chim. Acta* **853**, 46-58 (2015).
 132. J. L. Wheeler, C. B. Dreyer, J. Poshusta, J. L. Martin, and J. M. Porter, "Real-time monitoring of room-temperature ionic liquid purity through optical diode-based sensing," *Sens. Actuators B Chem.* **220**, 309-313 (2015).
 133. G. Li, Y. Sui, M. Dong, W. Ye, C. Zheng, and Y. Wang, "A carbon monoxide detection device based on mid-infrared absorption spectroscopy at 4.6 μm ," *Appl. Phys. B* **119**, 287-296 (2015).
 134. R. Adami, and J. Kiefer, "Light-emitting diode based shifted-excitation Raman difference spectroscopy (LED-SERDS)," *Analyst* **138**, 6258-6261 (2013).
-

10 List of abbreviations

Latin symbol

A	Amplitude
$A_{\tilde{\nu}}$	Spectral absorbance
A_j	Fitting constant
A_L	Surface area of the liquid
A_m	Maximum amplitude in the electric or magnetic field
A_t	Amplitude of the electric or magnetic field at time t
B	Rotational constant
B_j	Fitting constant
c	Speed of light
d	Distance between two parallel plates
E	Total energy
E_{el}	Electronic energy
E_{vib}	Vibrational energy
E_{rot}	Rotational energy
ΔE	Energy difference at two quantum states
F_w	normalized absorption coefficient with respect to pure water
F_T	normalized absorption coefficient with respect to room temperature
Δf	Mean wavenumber separation between interference maxima
$G(\nu)$	Vibrational energy
g_h	Mass flux of liquid
h	Planck's constant
\hbar	Reduced Planck's constant

List of abbreviations

H	Hamiltonian operator
I_0	Initial intensity
I_t	Transmitted light intensity
J	Jacobian matrix
J	Rotational quantum number
J'	Quantum number for the upper state
J''	Quantum number for the lower state
k	Boltzmann constant
$k(\nu_i)$	Absorption coefficient
L	Distance
m	Mass
N	Total number of molecules
n_L	Molar density of absorption species
n	Refractive index
R	Ratio
T_L	Liquid temperature
u	Non-specific background attenuation
V	Volume
w	Mass fraction
X	Known quantity
X	Samples
x_s	Humidity ratio in saturated air
x	Humidity ratio of the surrounding air
z	Path length

List of abbreviations

BS	Beam splitter
CCD	Charge-coupled device
DLAS	Diode laser absorption spectroscopy
DFB	Distributed feedback
DG	Diamond Grade
DR	Diffuse reflection
EG	Engineer Grad
FC	Fiber combiner
FDM	Frequency-division multiplexing
FTIR	Fourier transform infrared
GM	Gimbal mount
HI	High Intensity
HPD	Highest posterior density
IC	Internal combustion
IP	Impingement point
IR	Infrared
LIF	Laser-induced fluorescence
LCI	Low-coherence interferometry
LED	Light-emitting diode
MAP	Maximum a posterior
MCMC	Markov chain Monte Carlo
MCR-ALS	Multivariate curve resolution-alternating least squares
MLE	Maximum likelihood
MVN	Multivariate normal
NA	Numerical aperture
NI-DAQ	National Instruments data acquisition

List of abbreviations

NIR	Near infrared
PTFE	Polytetrafluoroethene
RFL	Reflected focal length
RR	Retro-reflecting
SCR	Selective catalytic reduction
SHO	Simple harmonic oscillator
SLED	Super luminescent light emitting diode
SI	Spark Ignition
SMF	Single-mode-fiber
SNR	Signal-to-noise
SOE	Start of the experiment
SR	Specular reflection
TDLAS	Tunable diode laser absorption
TDM	Time-division multiplexing
TIR	Total internal reflection
UV	Ultraviolet
WDM	Wavelength-division multiplexing
WMS	Wavelength-modulation spectroscopy

Greek symbol

α	Incident angle
$\alpha_{\text{Cal.}}$	Transmission correction factor
Γ	Covariance matrix
δ	Liquid film thickness
θ	Evaporation coefficient
λ	Wavelength
μ	Mean value
ν	Frequency
ν	Vibrational quantum number
$\tilde{\nu}$	Wavenumber
π	Probability density
ρ	Density
σ_L	Absorption cross section
σ_x	Uncertainty in x
τ	Transmission
Ψ	Wave function of quantum system
ω	Classical oscillator frequency

11 Acknowledgments

I would like to express my most sincere gratitude to Prof. Dr. Christof Schulz for his guidance throughout my studies at Duisburg. He makes my PhD journey an exciting and rewarding experience with his unwavering support and consistent encouragement. His creative ideas, critical thinking, and incredible effort have served as an excellent model for me throughout the research process.

I wish to forward my special thanks to Prof. Dr. Thomas Dreier for his time, and detailed suggestions in the research and numerous drafts of presentations and manuscripts.

And I would like to thank Dr. Jay B. Jeffries from Stanford University and Prof. Dr. Kyle Daun from University of Waterloo for the scientific guidance and constant assistance.

I also appreciate the support, assistance and friendship of my colleagues in the IVG group, including Florian Schneider, Jan Menser, Lin Shi, Thorsten Benzler, Matthias Beuting, Dr. Thorsten Endres, Dr. Robin Chrystie, Dr. Peter Fjodorow, Simon Görs, Raphael Mansmann, Dr. Daniel Fuhrmann, Martin Goschütz, Dr. Sebastian Kluge, Jasmina Kovacevic, Adrian Münzer, Dr. Hans Orthner, Bo Shu, Dr. Lisong Xiao, Ming Zhao, Dr. Yeehwa Schelleier, Samer Suleiman, Jörg Albrecht, Erdal Akyildiz, Beate Endres, Dieter Hermanns, Ludger Jerig, Birgit Nelius, Natascha Schlösser, and many others. Thanks for the nice atmosphere all of them have brought to me. Especially, thanks to the whole diagnostic group for the discussion in the group meeting every two weeks.

Finally, I am most indebted to my wife, Fengping Wu, for her love and support. I am grateful to my family, my parents Guoyu Pan and Cui Liu, parents-in-law Xinjing Wu and Hongmei Liang. Thanks for their continuous love, understanding and support beyond measure.

